Structural analysis of HfO_2 and $HfSi_2$ ultra-thin films on Si(100): A photoelectron diffraction study

Dissertation

zur Erlangung des Doktorgrades der Naturwissenschaften

der Fakultät Physik der Technischen Universität Dortmund

vorgelegt von

Christian Rolf Flüchter

- Juni 2008 -

Contents

Acronyms III

Introduction V

1 Photoemission Techniques 1

1.1 The Photoelectric Effect . . . 1

1.2 Electron Yield . . . 2

1.3 Photoelectron Spectroscopy . . . 4

1.4 Photoelectron Spectra and Line Shapes . . . 6

1.4.1 Chemical Shift . . . 8

1.4.2 Line Shapes . . . 9

1.5 Photoelectron Diffraction . . . 11

2 Computer Simulations and Algorithms 17

2.1 Simulating Diffraction Patterns . . . 17

2.1.1 The MSCD Program . . . 20

2.1.2 The MSPHD Program . . . 21

2.2 Algorithms . . . 22

2.2.1 The Levenberg-Marquardt Method . . . 22

2.2.2 The Nelder-Mead Method . . . 22

2.2.3 Genetic Algorithms . . . 23

3 Technological Relevance of HfO_2 and $HfSi_2$ 29

3.1 High-k Dielectrics . . . 29

3.2 Nanowires . . . 30

4 Experimental Setup **33**
4.1 UHV Chamber 33
4.2 Sample Holder 34
4.3 Analyzer / Detector 35
4.4 Evaporator 36
4.5 Beamline 37

5 Results and Discussion **41**
5.1 XPD Data Treatment 41
5.2 Clean Silicon 44
5.2.1 High Energy Results 45
5.2.2 Low Energy Results 48
5.3 $HfSi_2$/Si(100) High Energy Investigation 50
5.4 $HfSi_2$/Si(100) - Thin Layer 56
5.4.1 XPS Investigation 56
5.4.2 XPD Investigation 60
5.5 $HfSi_2$/Si(100) - Thicker Layer 70
5.5.1 XPS Investigation 70
5.5.2 XPD Investigation 72
5.5.3 Lattice Alignment 78
5.6 Real Space Imaging of Annealed Hf Films on Si(100) 79
5.7 Stability of EBE Prepared HfO_2/Si(100) 82
5.8 Stability of the System HfO_2/Si_3N_4/Si(100) 89

6 Conclusions and Outlook **95**

A Properties of Hafnium and Silicon **101**

B Sample Input Files **103**

Bibliography **105**

Publications **115**

Acknowledgements **117**

Acronyms

AES ... Auger Electron Spectroscopy
AFM ... Atomic Force Microscopy
CEM ... Channel Electron Multiplier
DELTA ... Dortmunder Elektronen Speicherring Anlage
EBE ... Electron Beam Evaporator/Evaporation
EOT ... Equivalent Oxide Thickness
EXAFS ... Extended X-ray Absorption Fine Structure
FET ... Field Effect Transistor
GA ... Genetic Algorithm
GCA ... Gradual Channel Approximation
HE ... High Energy
IL ... Inter Layer
LE ... Low Energy
LEED ... Low Energy Electron Diffraction
LNLS ... Laboratório Nacional de Luz Síncrotron
MOSFET ... Metal-Oxide-Semiconductor Field Effect Transistor
NWFET ... Nanowire Field Effect Transistor
PE ... Photoelectron
PED ... Photoelectron Diffraction

PES .... Photoelectron Spectroscopy

RT .... Room Temperature

SEM .... Scanning Electron Microscopy

STM .... Scanning Tunneling Microscopy

UHV .... Ultrahigh Vacuum

UPS .... Ultraviolet Photoelectron Spectroscopy

XPD .... X-Ray Photoelectron Diffraction

XPS .... X-Ray Photoelectron Spectroscopy

XRF .... X-Ray Fluorescence

Introduction

Probing for the electronics and the structural properties of semiconductors is an important field in surface science. In particular, reconstructions and surface adsorbates are in the focus of scientific activities, because of their significant influence on surface properties. In recent years the silicon surface and its interface to hafnium dioxide gained a lot of interest due to its technological relevance in the semiconductor industry [1–4].

In the 1960s, Gordon Moore predicted that the switching-speed of micro-electronic devices would keep increasing exponentially. This prediction came true within the last 40 years, where the switching-frequencies of so-called MOSFETs (metal-oxide semiconductor field effect transistors) grew by a factor of $1.5 - 1.8$ per year. This development was accompanied by a continuous miniaturization of the devices. The link between their performance and their size is not coincidental, but can be directly derived from the electrodynamics of the MOSFET design. This was already shown by Shockley in the 1950s [5].

The ongoing down-scaling of the devices, as they are produced for decades now, turns out to be limited by the electronic properties of their gate dielectric. In order to insulate the gate electrode from the channel region of a MOSFET a thin silicon dioxide (SiO_2) layer is used. Reducing its thickness is one possibility to further enhance the performance of MOSFET devices. More details are provided in Ch. 3. If the gate oxide's thickness is reduced below 12 Angstroms, increasing tunneling currents occur leading to a sever reduction in the MOSFETs' performance. To overcome this problem in the near future the use of alternative gate dielectrics is proposed [1,2]. The most important property of the desired substitute would by a high dielectric constant κ. The most promising candidates for a replacement of SiO_2 are HfO_2 and ZrO_2. The main concern regarding these materials is a lack of their thermal stability on silicon. Annealing to temperatures above 700°C causes the formation of a $HfSi_2$ compound having a metallic characteristic, destroying the layers' insulating properties.

The stability of this system under certain preparation conditions is investigated in this work. Possible solutions to the stability problem are introduced by nitrogen implantation.

While the formation of $HfSi_2$ nano-structures is adversarial in the case discussed above, it turns out to be valuable for nanometer-sized wiring of semiconductor devices, e. g. for MOSFETs. The hafnium silicide compound, created upon annealing, turns out to form self-assembled nanowires on silicon surfaces [6, 7]. In this case, the knowledge of their structure is one step for calculating their electronic properties (cf. Ch. 3). Nonetheless, current literature on this system relates mainly to scanning probe microscopy investigations that do not probe the inner structure of the nanowires.

The clarification of structure and morphology of those self-assembled structures is the subject-matter of the first part of this work. Using photoemission spectroscopy and related methods as well as real space imaging, an unambiguous picture of these structures will be drawn.

The photoelectric effect is one of the most prominent processes, when it comes to the investigation of surfaces, surface related systems, and interfaces. Its principals were discovered and described more than 100 years ago [8, 9]. Since this time a lot of effort was put into methods and devices to exploit the chemical sensitivity of the photoelectric effect. Major achievements regarding x-ray photoemission spectroscopy (XPS) within the last decades were the development of ultra-high vacuum chambers, new light sources like synchrotrons, and very efficient electron spectrometers. For most of the recent experiments in surface science, including those presented in this work, the use of tunable, high-flux synchrotron radiation is inevitable.

One important extension to XPS is x-ray photoelectron diffraction (XPD). It is known since the 70s of the last century [10]. It uses the interference of photoelectrons scattered at the atom lattice around an emitter while escaping the surface. The resulting interference patterns can be used, analogous to holography, to determine the local real space structure around an emitting atom. This method for structural determinations is of significance, especially regarding buried interfaces. An extended introduction to XPD is provided in Ch. 1.5. While surface structures can be probed by real space imaging, e. g. by scanning tunneling microscopy (STM), buried interfaces cannot be accessed by those methods. The main difficulty using XPD, in contrast to holography, is the loss of phase-information during the measurement of the photoelectrons. Without this phase-information interface structures cannot be calculated directly from the data. Instead, computer simulations of model structures have to be conducted and to be compared to the experimental results in order to clarify the structure of a system. This procedure requires a significant computational effort and the use of distinct algorithms. One of those was particularly developed for this purpose in the course of this work.

In the **first** chapter an introduction to the methods and their theoretical bases is provided. This includes the photoelectric effect and the generation of electrons in a solid. An overview over additional excitations of the solid, going along with photoemission, and their influence on spectroscopy, is provided as well. Applications like x-ray photoelectron spectroscopy (XPS) and x-ray photoelectron diffraction (XPD) are discussed. They are the most important methods for the consecutive work.

The **second** chapter gives a detailed insight into the computational methods necessary to correctly interpret diffraction patterns recorded by XPD, or for decomposing XPS spectra. The programs needed for conducting computer simulations of XPD patterns, namely the programs MSCD and MSPHD, are introduced. An overview on fitting procedures and their fields of use is given. One can distinguish between deterministic and probabilistic algorithms. Concerning the first kind, the Levenberg-Marquardt and the Simplex algorithm are introduced. For the part of the probabilistic methods, genetic algorithms are discussed in detail.

The **third** chapter provides a summary over the fields of science where the systems $HfSi_2$/Si and HfO_2/Si are of active interest. As a first example the relevance of HfO_2 for the use in the semiconductor industry and the concerns about its thermal stability is outlined. As a second example the use of $HfSi_2$ in the field of quasi-one-dimensional nanowires is sketched.

The **fourth** chapter deals with the experimental setup that was used to conduct the experiments to be presented later on. In addition to the ultra-high vacuum chamber and the detection unit, a view on the evaporation and excitation devices, in particular to beamline 11 at DELTA, is provided.

Starting with the **fifth** chapter the results obtained for the different systems are discussed. The chapter begins with an introduction on the processing of XPD data, followed by the investigation of a clean silicon surface using two different energies. In Ch. 5.3 an R-factor analysis of a high excitation energy measurement on the system $HfSi_2$/Si(100) is presented. Preliminary results are used as a basis for the analysis. Ch. 5.4 deals with a soft x-ray investigation on the system $HfSi_2$/Si(100). In contrast to x-ray tube measurements a high surface sensitivity and high energy resolution made the determination of atomic distances and surface reconstructions possible. For an independent indication for a presumed island formation of $HfSi_2$ on the surface, real space images using atomic force microscopy and scanning electron microscopy are presented in Ch. 5.6. The stability of the system HfO_2/Si(100) under the preparation conditions used is tested in Ch. 5.7. A possible solution to the lack of thermal stability of HfO_2 is presented in Ch. 5.8. An ultra-thin silicon nitride (Si_3N_4) layer is introduced at the HfO_2/Si interface. It ought to function as diffusion barrier for silicon to suppress the creation of interfacial SiO_2.

In chapter **six** the new findings regarding the $HfSi_2$ structures and the stability of HfO_2 are summarized and final conclusions are drawn. In addition, an outlook to a possible continuation or to consecutive investigations is provided.

1 Photoemission Techniques

1.1 The Photoelectric Effect

Heinrich Hertz discovered the ability of light interacting with electrons in 1887 [8]. He observed the influence of ultra-violet light on spark discharges between two electrodes. Later on, more detailed investigations were undertaken by his student Hallwachs. For this reason the photoelectric effect is also called the "Hallwachs-effect". An exact explanation for it could not be given within classical physics. The solution to the problem was discovered by Albert Einstein in the year 1905 [9] by assigning particle properties to light, as firstly proposed by Planck. Using these "photons" and assuming energy conservation he formulated the famous photoelectric equation

$$E_{kin,e} = h\nu - W, \tag{1.1}$$

where $h\nu$ is the primary energy of the incident light (ν is its frequency and h is the Planck constant), W is the overall energy that needs to be supplied for releasing the electrons from the solid, and $E_{kin,e}$ is the final kinetic energy the electrons have escaping the surface. Later on, it was found that W can be split up in $W = E_{bin} + \phi$, being i. e. the binding energy of the electrons to the atoms and an additional surface energy, or work function, the electrons have to overcome at the surface.

In the most simple case the electron system of the atom is assumed to remain in the ground state during the photoemission process (the Koopmans theorem [11]). Even this estimation gives reasonable results according to Eq. (1.1); experimental results often show a slightly higher kinetic energy of the emitted photoelectrons. This energy originates from the relaxation energy of the exited electron system within the solid that can be partially transferred to the photoelectron [12].

By gauging the electrons' kinetic energies one can determine their binding energies within the solid. Throughout the last century many methods were developed to exploit this effect gaining valuable information about matter, which includes liquids and gases, namely: ultraviolet photoelectron spectroscopy (UPS), x-ray photoelectron spectroscopy (XPS), x-ray photoelectron diffraction (XPD), photoemission electron microscopy (PEEM), and x-ray standing waves (XSW). These are just some examples for the use of the photoelectric effect, which will be addressed later.

1.2 Electron Yield

The number of electrons leaving the surface with respect to the number of photons impinging onto the surface depends on several parameters. In addition to the mass density of a material, its photoelectron cross-section plays an important role. This quantity gauges the probability for a photoemission event taking place at a particular orbital and for a given photon energy. Fig. 1.1(a) displays two examples of photoelectron cross-sections. It was found that they can change by orders of magnitude if the excitation energy is varied [13]. The graph shows these quantities for the Hf 4f and the Si 2p state, which are the most prominent ones in this work. Further details on the properties of these two materials are given in appendix A. Quantitatively, the differential cross-section can be estimated using a dipole approximation [15]

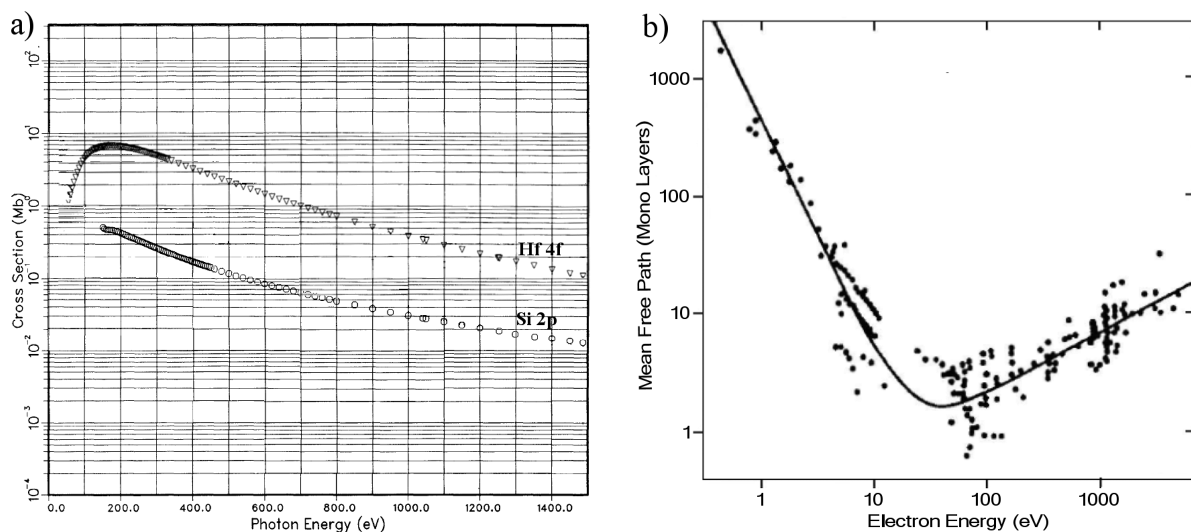

Figure 1.1: Photoionization cross sections for the Hf 4f and the silicon 2p state (a) [13]. Inelastic mean free path of electrons in solids with respect to their kinetic energy (in units of monolayers) (b) [14].

$$\frac{d\sigma}{d\Omega} \propto \frac{1}{d_I \cdot E_{Prim}} \sum_{i,f} \left| < \Psi^f | \sum_1^N \Delta_i | \Psi^i > \vec{e} \right|^2 , \tag{1.2}$$

where the quantity d_I describes the degeneracy of the initial state, in the right part of the equation, and the sum runs over all possible matrix elements for allowed transitions of the N electron system.

Furthermore, electrons do not propagate unhindered through the solid. The interaction with the electron system of the lattice can lead to the excitation of plasmons, for example. Interaction with adjacent atoms can cause the exchange of phonons [16]. If it is assumed that the probability of these events is a constant throughout the material, the number of electrons keeping their initial energy decays exponentially by the depth d from where the particles escape:

$$N_e = N_0 e^{-\frac{d}{\lambda \sin(\theta)}} \tag{1.3}$$

The mean free path the electrons travel before inelastic scattering occurs is called λ. The term $\sin(\theta)$ takes the observation angle θ, with respect to the surface normal, into account. The path length the electrons from a certain depth have to pass through within the solid increases with increasing θ. This is why photoemission experiments are more surface sensitive under a grazing incident angle. The quantity λ furthermore strongly depends on the kinetic energy of the electrons, while depending weakly on the kind of material through which the electrons propagate. This gives rise to the so-called universal curve that is displayed in Fig. 1.1(b). It displays the mean free path of electrons with respect to their energy. It is found empirically. Every black dot stands for the λ of a certain material in a certain configuration. The development of the curve can be qualitatively understood by the electron-lattice interactions as previously mentioned [14].

Still, this approach does not explain (observation-) angle dependending of diffraction effects, as up to now only homogenous and amorphous media have been assumed. On the contrary, many samples exhibit a crystalline structure. By accounting for the geometry of the sample, photoemission can be exploited to yield valuable information about the samples' atomic structure. The phenomenon will be discussed in detail in Chs. 1.5 and 2.1.

1.3 Photoelectron Spectroscopy

A standard photoemission (PE) experiment is shown in Fig. 1.2. Photons with energy $E_{ph} = h\nu$ are impinging onto a surface under an angle α. The photoelectrons, emitted under an angle θ, are observed by an electron analyzer. For many applications α and θ are chosen being in the same plane with respect to the surface normal.

X-ray light for photoemission experiments can be generated by various sources that have different fields of use. Conventional x-ray tubes produce light of defined wave length depending on the materials their anode is coated with. For example, Mg K_α-radiation ($h\nu = 1253.6$ eV) or Al K_α-radiation ($h\nu = 1486.6$ eV) [17]. While such tubes are easy usable and low in cost compared to a synchrotron, they on the other hand deliver a comparably low energy resolution and photon intensity. For a Mg K_α-source, for example, the resolution is about $\Delta E \approx 0.7$ eV. Other possible sources are gas-discharge lamps and synchrotron radiation sources. Advantages and disadvantages of the sources are summarized in Tab. 1.1. For most of the applications the use of a synchrotron is favorable. Its only disadvantages are the rather low availability and the decay of the light's intensity during long-term experiments.

The excitation energy is chosen with respect to the application. For many experiments a high surface sensitivity is necessary, resulting in preferred electron energies of around 50 – 60 eV and thus a primary energy lying at about the same level above the binding energy of a certain state. For historical reasons the energy ranges of the impinging photons have been given different

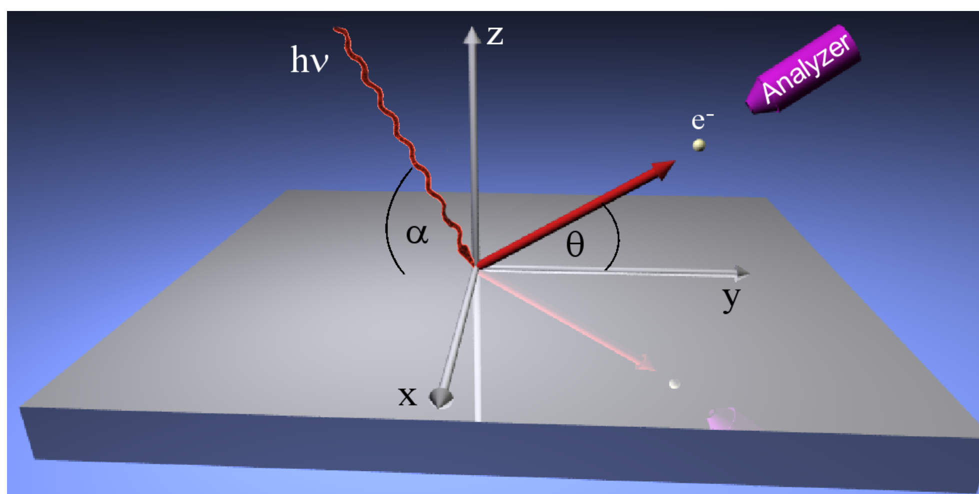

Figure 1.2: Schematic of a standard PE experiment. The light used for excitation can either be produced by a synchrotron light source, an x-ray tube, or a gas discharge lamp. The work principals of the electron analyzer will be described in Ch. 4.

device	excitation energy [eV]	energy resolution [meV]	flux $[\frac{photons}{cm^2 \cdot s}]$	variable energy	availability
x-ray tube	100-10000	500-2000	$\approx 10^9$	no	high
discharge lamp	10-40	1-100	$10^{10} - 10^{13}$	no	high
synchrotron	30-15000	10-100	$10^{11} - 10^{13}$	yes	low

Table 1.1: Comparison of key parameters of different x-ray sources (cf. e. g. [18]).

names. Using energies of $10 - 50$ eV ($10 - 100$ eV sometimes), the experiments are called ultra violett photoelectron spectroscopy (UPS), for energies above 100 eV the method is named x-ray photoelectron spectroscopy (XPS). One also sometimes distinguishes XPS and soft-XPS (SXPS) for photon energies above 1000 eV and below 1000 eV.

Throughout all energies, excitations of the electron system are mainly relaxed via two channels, shown schematically in Fig. 1.3 [19]. The core-hole, created by the photo ionization (Fig. 1.3(a)), is eventually filled by an electron from another (higher) shell. The relaxation energy released by this process can either be emitted as an x-ray photon (Fig. 1.3(b)), or by transferring the energy to a third electron involved in the process through a so-called “virtual photon” (Fig. 1.3(c)). The first channel is called x-ray fluorescence (XRF), the second one Auger process, named by Pierre Auger [20] after he discovered the process subsequently to Lise Meitner. The analysis of these electrons is called Auger electron spectroscopy (AES). The possible transitions are labelled according to the shells of the involved electrons (“KLL” in the case of Fig. 1.3(b)). For lighter

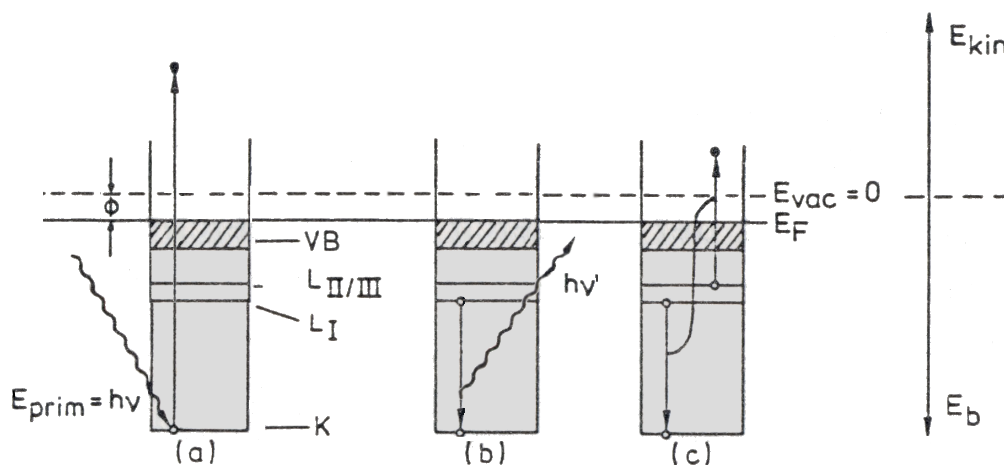

Figure 1.3: Excitation and relaxation in photoemission [19]. Removal of a K-shell electron by photoionization (a), refilling of the core-hole by an electron from a higher state and emission of an x-ray photon (b), or an Auger electron (c).

elements up to Z≈ 30 the fraction of Auger electrons overweighs XRF, because their production increases as the difference between the energy states of the shells decreases. For elements of higher Z, XRF becomes more significant [21]. Both effects can be exploited to gain information about the structure and electronics of a system.

Besides photoemission, the setup in Fig. 1.2 can be inverted so that the surface is irradiated with electrons and one observes the photons produced by bremsstrahlung within the surface. As for the electrons fall into a lower finial state by emitting photons, this process is called inverse photoemission (IPE). Through the amount of photons produced with respect to their energy, the density of states can be probed by this technique.

1.4 Photoelectron Spectra and Line Shapes

For determining the electronic states within the solid, the electrons leaving its surface are separated by their kinetic energy. This is done by an electron analyzer (cf. Ch. 4). The number of electrons of a certain energy is finally determined by a channel photomultiplier (cf. Ch. 4.3). Scanning all possible kinetic energies results in a graph as shown in Fig. 1.4. Here, the number of electrons passing through the analyzer within a given span of time, is plotted versus their kinetic energy. Several features, each of which representing excitations and states of the solid, can be distinguished. Besides the core level peaks and Auger lines, as discussed above, the steep slope at the left end of the spectrum contains secondary electron and electrons that were inelastically scattered within the crystal. The right end side of the spectrum, i. e. at high kinetic energies,

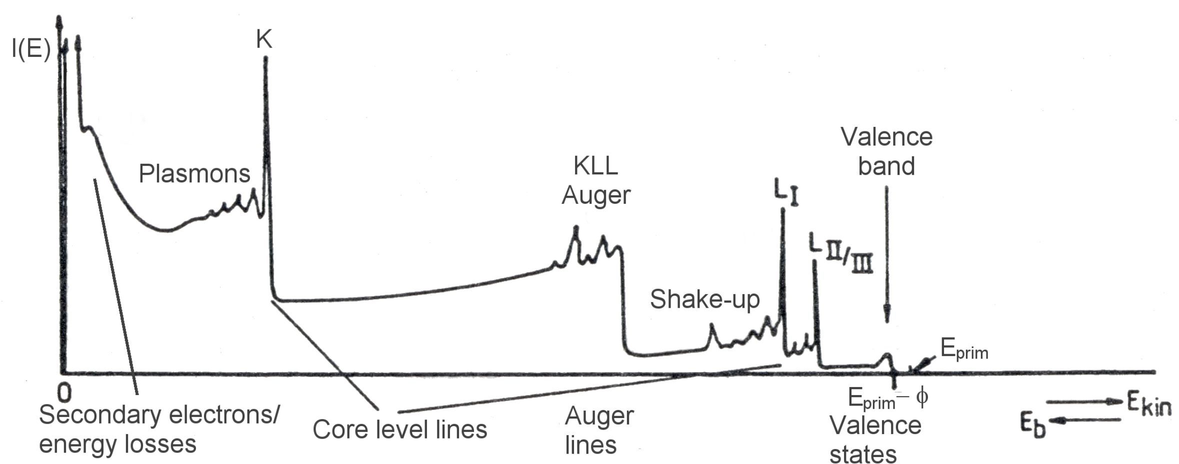

Figure 1.4: Typical x-ray photoelectron spectrum of a metal surface [19]. The different features appearing are explained in the text.

exposes the valence band structure and finally the Fermi-edge. Angle-resolved measurements of those features yielding information about the band structure and the morphology of the Fermi-surface in k-space and can be combined with photoelectron diffraction [22].

Further structures in an XPS spectrum are generated by interactions of core level photoelectrons with the electron system of the crystal. (Surface-)plasmons are collective excitations of the electron system [23]. Plasmons are oscillations of the electrons with respect to the atoms; several higher modes can be excited beside a base frequency. This leads to a set of equidistant lines besides the core level peak towards lower kinetic energies. The plasmon base frequency can be estimated in a free electron model [23] as

$$\omega_p = \sqrt{\frac{ne^2}{m\varepsilon_0}}, \tag{1.4}$$

where n represents the density of valence states, e the charge, and m the mass of an electron. Typical excitation energies of plasmons are in the order of $3-10\,\mathrm{eV}$. In contrast to the plasmon, a shake-up process reflects the excitation of one or more electrons of the atom from which the photoelectron escapes, changing the ground states of the system. The complex dynamics of this process is still investigated [24]. Nevertheless, excitation energies for shake-ups are in the same order as plasmon energies. If another electron leaves the atom as a result of a shake-up, the process is called a shake-off.

Up to now, only intrinsic effects of the surface have been discussed. Especially for x-ray tube measurements there are some additional effects that must be accounted for. Firstly, the light of the sources is often not fully monochromatic causing so-called “x-ray satellites”. Despite of the use of filters and monochromators, fractions of other characteristic lines close to the main line can irradiate the sample. This leads to additional and slightly shifted XPS peaks. Their intensity is usually severely lower compared to the signals excited by the main line so that they are often mistaken for impurities of the surface. Secondly, older or not well fabricated x-ray tubes tend to produce “ghost lines”. They are in fact characteristic lines of other elements. The anode of an aluminium x-ray tube, for example, often consists of an aluminium coated copper block. If the coating is damaged, a copper K_α-line ($h\nu = 8979\,\mathrm{eV}$) can be produced. If the anode is oxidized, oxygen K_α-radiation ($h\nu = 543.1\,\mathrm{eV}$) can be excited [17].

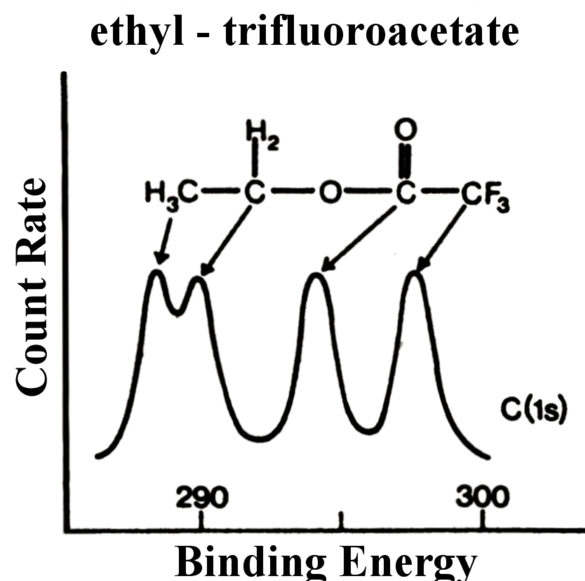

Figure 1.5: The chemical shifted C 1s signal in ethyl-trifluoroacetate is one of the first and most prominent examples for the effect of the chemical environment on core level binding energies [25–27].

1.4.1 Chemical Shift

An important resource for the chemical analysis of surfaces via XPS is the so-called chemical shift [26, 27]. In some cases conclusions regarding the structure can be drawn by its use. If an atom is surrounded by other atoms, the solution of the Schrödinger equation differs from the solution for a free atom. Thus the ground states for the electrons are shifted by a small amount. The extent of the shift depends not only on the species of the neighboring atoms, but also on the configuration of the lattice.

Fig. 1.5 displays chemical shifted XPS signals of the carbon 1s state in the ethyl-trifluoroacetate molecule. That state's binding energy in a pure carbon environment, i. e. in graphite, is around $E_b = 284.4$ eV [28,29]. One sees that the binding energy can be significantly influenced by vicinal atoms depending on their electron affinity. Typically those shifts are in the order of fractions of electronvolts up to more than 10 eV. Thus they can easily be accessed by photoelectron spectroscopy using synchrotron radiation.

Since atoms close to interfaces or surfaces are in a slightly different chemical environment compared to atoms of the same species in the bulk, their orbitals exhibit a shift of their binding energies. This is how photoelectrons can be distinguished by their origin within the crystal structure. If the shifts for a certain environment or chemical compound are known, structure

determinations for different parts of a layer stack become possible. This includes the recording of atom-specific diffraction patterns (cf. Ch. 1.5) using x-ray photoelectron diffraction.

1.4.2 Line Shapes

The intrinsic (inherent) line width of photoelectron signals is at first determined by the lifetime of the electrons' system excitation and hence the uncertainty relation. The shape of such a peak can be expressed as a Lorentzian function:

$$L(x) = \frac{1}{\pi} \frac{\frac{1}{2} w_L}{(x - x_c)^2 + \left(\frac{1}{2} w_L\right)^2} \tag{1.5}$$

In the given form the area below the curve is normalized to unity. The parameter w_L determines the width of the peak. x_c denotes its maximum.

If the signal originates from a state with angular momentum l≠0, the coupling between spin and orbit of the electrons leads to a splitting of the electrons' energy levels depending on whether the spin $\vec{s}$ is aligned parallel or anti-parallel compared to the angular momentum $\vec{l}$ of the orbital (see e. g. [30]). This leads to the quantum numbers j_+=l+$\frac{1}{2}$, and j_-=l-$\frac{1}{2}$ denoting the overall angular momentum. In addition, the degeneracy of each state can be written as 2j + 1. From this, one can derive the intensity ratio of the split states, which corresponds directly to the number of states possible. One example for the "L-S-coupling" will be given in Ch. 5.2.1.

In addition to the inherent line width, other phenomena can influence the resulting peak shape. The generation of electron-hole pairs can lead to asymmetric Doniach-Sunjic [31] or Mahan-profiles [32], especially in metals. Moreover, the peak can be broadened by the limited energy resolution of the electron analyzer. Most extrinsic effects add a Gaussian energy distribution of the form

$$G(x) = A \cdot exp\left(-\frac{(x - x_c)^2}{2w_G^2}\right) \tag{1.6}$$

to L(x). The width of that distribution is labelled with w_G. The resulting numerical peak function

$$V(t) = \int_{-\infty}^{t} L(x)G(x-t)dx \tag{1.7}$$

is yielded by the convolution of L and G and is called a Voigt-profile [33] (after Woldemar Voigt). In fitting procedures the use of numerical functions is often circumstantial. For this reason several analytical so-called “pseudo-Voigt” functions were developed, which are very similar to a Voigt-profile. In this work the function “PsdVoigt2”

$$pV(x) = A\left[\mu\frac{2}{\pi}\frac{w_L}{4(x-x_c)^2+w_L^2} + (1-\mu)\frac{\sqrt{4\ln 2}}{\sqrt{\pi}w_G}\exp\left(-\frac{4\ln 2}{w_G^2}(x-x_c)^2\right)\right] \tag{1.8}$$

of the Origin 7.0 program package was used [34]. The terms in Eq. (1.4.2) correspond to Lorentzian and Gaussian contributions. The parameter μ gauges the strength the two parts are contributing. It has been set at $\mu = 0.5$ here. Further discussions concerning pseudo-profiles and their applicability to photoemission spectra can be found in [35].

Nevertheless, in many cases the inherent line width turns out being much smaller than the peak broadening ($w_G \gg w_L$) so that the Lorentzian distribution can be neglected and the spectra can be suited to pure Gaussian distributions.

As mentioned before, surfaces having a metallic characteristic can produce asymmetric line shapes. Again, these profiles have a non-analytic form, but can be expressed as a pseudo profile of analytic form. In the case of the Doniach-Sunjic profile an exponential function can be used and be multiplied to the ascending slope of the Voigt-profile [35] by:

$$\begin{aligned} pDS(x) &= pV(x) + (1-pV(x)) \cdot T(x), \text{ where} \\ T(x) &= \begin{cases} \exp(-\frac{x-x_c}{w_{GL}}) & \text{if } x < x_c \\ 1 & \text{otherwise} \end{cases} \end{aligned} \tag{1.9}$$

The width w_{GL} in the pseudo Doniach-Sunjic function stands for the convolved line width of the Gaussian and Lorentzian profiles. To suite this kind of profile to the experimental results the program FitXPS [36] was used.

1.5 Photoelectron Diffraction

The method XPD (x-ray photoelectron diffraction) is based on XPS and employs the fact that the directly emitted photoelectron wave is elastically scattered by surrounding atoms. The scattered wave's components coherently interfere with the directly emitted component, leading to an observation-angle depending intensity modulation of the XPS signal. The quantitative analysis of these modulations can provide information about the local structure around the emitting atom. An extended review on the methods concerning theoretical aspects as well as experimental capabilities can be found in [37–40], for example.

The phenomenon was firstly discovered by K. Siegbahn et al. in 1970 while observing photoelectron spectra from a sodium chloride (NaCl) crystal [10]. The first theoretical approach was given by A. Liebsch in 1974 [41]. Several key parameters have to be considered for calculating the photoelectron intensity $I(\theta,\phi)$ depending on the emission angles θ and ϕ. The inelastic mean free path λ determines the radius around an emitter from where scattering events from neighboring atoms have to be taken into account (cf. Ch. 1.2). As a direct consequence the surface sensitivity of the experiment is determined by λ.

An important parameter is the atomic scattering cross-section, that further dependents on the energy and the scattering angle. Fig. 1.6(a) displays scattering factors of silicon with respect to the scattering angle for various electron energies [42]. The curves are normalized by the scattering factors at $\theta = 0°$, i. e. "forward scattering". Two significant features emerge from the graph. At first, there is a strong forward scattering maximum at $\theta = 0°$ that appears throughout all the energies from $50 - 1000$ eV. Secondly, there is a maximum appearing at a scattering angle of $\theta = 180°$, i. e. "back scattering" takes place. Even though forward-scattering is emphasized for all energies, back-scattering becomes more significant at lower kinetic energies (around 100 eV). The scattering pathways for a forward and a backward single-scattering event are illustrated in Fig. 1.6(b).

Besides the angular dependent cross-section, a scattering event also involves a phase shift of the scattered wave, also depending on the electrons' energy [39]. For higher energies, above $450 - 500$ eV, the phase shifts for forward scattering events, as shown in the upper part of

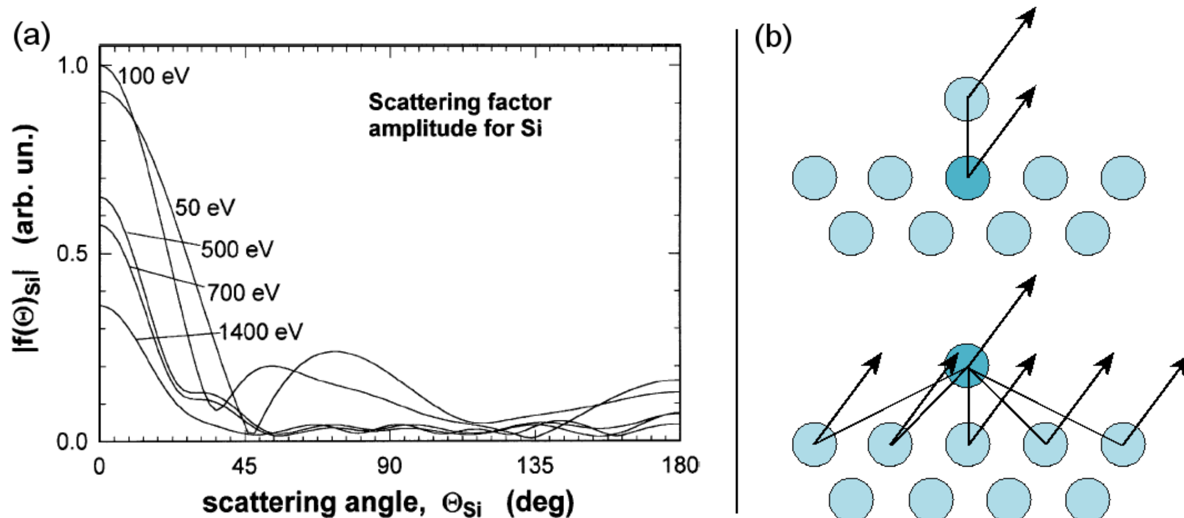

Figure 1.6: Normalized angle and energy dependent electron scattering factors of silicon (a) [40]. Pathways of a forward scattering event (b) and a backward scattering event (c) in XPD. Further explanation is given in the text.

Fig. 1.6(b), are always smaller than π. Because of this, only constructive interference takes place in single scattering leading to strong scattering peaks along the connecting line between emitter and scatterer. In a simple version of XPD this can be used for determining the crystal orientation of a surface, or binding angles between the first and the second layer atoms. As long as the effect does not depend on kinetic energy, it can be probed by various conventional x-ray tubes. No diffraction effects have to be considered in this case, but it is often difficult to tell the layer from where the signal originates. Except for some special cases the signals from the second, third, and forth layer are often hardly separable.

Furthermore, multi-scattering events have to be taken into account. In a crystalline structure atoms are lined up in chains in certain directions. Although the scattering phase shifts are small here, they can add-up by multiple-scattering along the chain and finally become destructive [39].

One can see that forward scattering can be used to get a rough picture of the geometry and symmetry within a system at least in some cases. Some favored systems can be fully solved by this method (an example is given below). However, in most cases it is inevitable to conduct detailed diffraction simulations of model structures. A schematic of a photoemission and diffraction event as well as the associated magnitudes are shown in Fig. 1.7.

Here, the photoelectron wave with wave vector $\vec{k}$ is emitted from a core shell of an atom located at the point $\vec{r}$ within the surface. The scattering event takes place at a neighboring atom j located at the coordinate $\vec{r}_j$. The primary and scattered waves have a locked phase that is

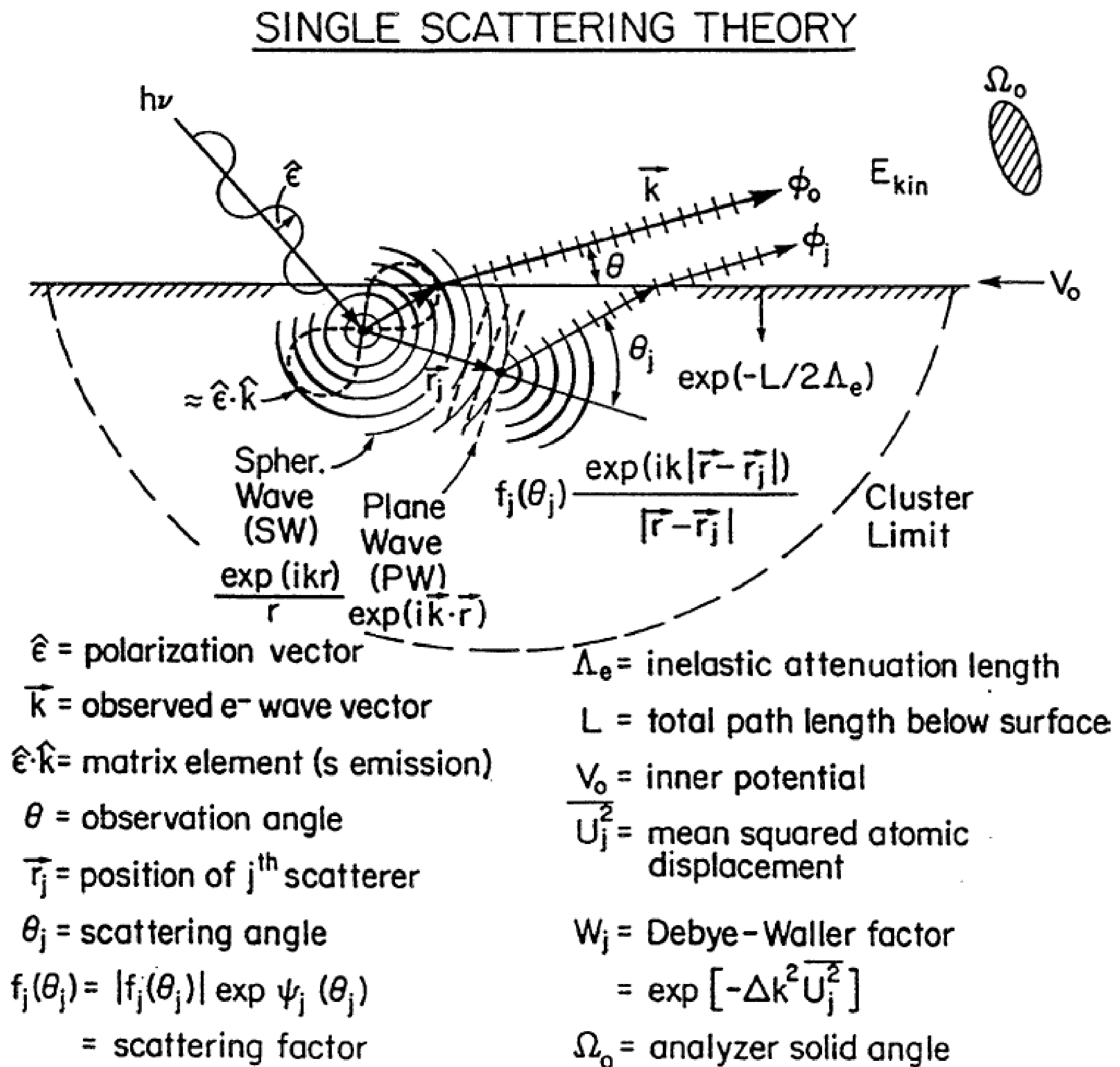

Figure 1.7: Schematic drawing of the processes involved in photoelectron diffraction (single scattering). A core-level photoelectron propagates and part of the propagating wave is scattered at the near-neighbor environment of the emitting atom. The primary and the scattered part are coherent [43].

determined by their distance and the scattering phase shift, as described before. The spherical character of the s-wave assumed here is introduced by multiplying a factor $\frac{1}{r}$ to the propagating wave. The exponential decay of the wave's intensity inside the surface is included by the factor

$$\exp\left(\frac{-L}{2\lambda}\right), \tag{1.10}$$

where L and λ describe total path length and the inelastic attenuation length, respectively. By summing up the amplitudes for all possible scattering events within the cluster radius, one can in this case explicitly calculate the modulation function $\chi(\vec{k})$ by

$$\chi(\vec{k}) = \sum_j \frac{\hat{\varepsilon} \cdot \hat{r_j}}{\hat{\varepsilon} \cdot \hat{k}} \cdot \frac{W_j}{r_j} \exp\left(\frac{-L}{2\lambda}\right) \cdot \mid f_j(\Theta_j) \mid \cdot cos\left[kr_j(1 - \hat{k} \cdot \hat{r_j}) + \Theta(k, \hat{k} \cdot \hat{r_j})\right]. \tag{1.11}$$

The Debye-Waller factor W_j includes the dampening of the wave by vibrations of the scattering atom. For $j = 0$, i. e. the source of the primary wave, $f(\Theta)$ is set to unity. As the phase of the electron wave is not observable in quantum mechanics, this information is lost during the measurements. Electron analyzers can only detect intensities. Those can be written as the absolute square of the modulation function

$$I(\vec{k}) = I(\Theta_{obs}, \phi_{obs}) = \mid \chi(\vec{k}) \mid^2. \tag{1.12}$$

To obtain structural information from the interference, the $\vec{k}$-vector has to be varied. This can either be done by changing its modulus or its direction. Changing its absolute value goes along with changing the energy of the impinging photons [39, 44]. This kind of experiment can only be conducted using synchrotron radiation, where the excitation energy can be varied continuously. In contrast to that, an angle scanned experiment, wherein the observation angles θ and ϕ are varied, can be performed by using a synchrotron light source as well as a conventional x-ray tube. All measurements presented in this work use the angle scanned version of XPD.

Eq. (1.11) accounts for all effects involved in a photoemission event, nevertheless its provides only a simple picture of the process, as the primary wave is approximated to be spherical, and multiple scattering within the surface is neglected. Except for some favored cases, those effects have to be taken into account leading to rather complex mathematical problems (cf. Ch. 2.1).

The effects described so far are similar to those used in the method of extended x-ray absorption fine structure (EXAFS) [45, 46]. Nonetheless, there are some key differences regarding the sensitivity of the two methods in terms of the local structure around an atom. While in XPD the differential, i. e. the angle-resolved, photoelectron cross-section is evaluated, the EXAFS

technique relies on the total, or spherical, cross-section. This magnitude is mainly influenced by components of photoelectron waves that are back scattered onto the emitting atom by its closest neighbors. Through this, the presence of the vicinal atoms leads to a variation of the cross-section close to the main absorption edge, depending on their distance to the emitter, which is in fact the bond length. If one can isolate these variations, which is usually possible, the inter-atomic distances can be determined, but not their coordination with respect to the emitter. Measuring the angle resolved cross-section by means of XPD delivers a lot of additional information about the environment of an emitter compared to EXAFS, including the exact geometry and coordination of atoms within the surface, even though the interpretation of the data is usually more difficult. More details on this are given in Ch. 2.1.

One example where an adsorbate structure on a surface could be determined by photoelectron diffraction is the system CO/Ni(110). In this case the zero-order diffraction from a CO molecule was used for determining the tilt of the molecule adsorbed on Ni(110) by Wesner et al. in 1988 [48]. Earlier studies using quantitative LEED techniques were able to determine the molecule to occupy a bridge site on the surface [47], as shown in Fig. 1.8(a). Further investigations yielded inclination angles of the molecule of around 18°. In Fig. 1.8(b) a series of XPD polar

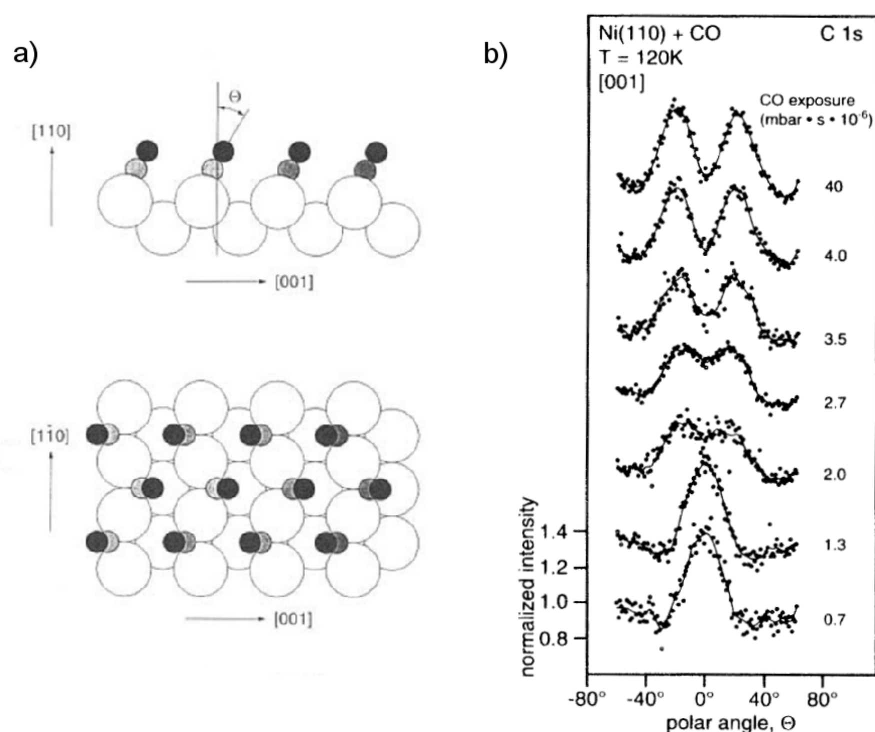

Figure 1.8: CO adsorption on a Ni(110) surface (a), studied by quantitative LEED [47]. XPD analysis (polar scans) (b) concerning the same system [48]. The forward scattering peaks appearing in the carbon 1s signal indicate the binding angle of the molecule.

scans is shown that were obtained by the group of Wesner from the C 1s photoelectron yield for increasing CO exposure up to the surface's saturation. A conventional Mg K_α x-ray tube with an excitation energy of $h\nu = 1253.6\,\mathrm{eV}$ was used for the experiments. It can be seen that a strong scattering peak appears at an angle of 0°, i. e. in normal emission, attributed to forward scattering at the oxygen atom. This indicates a perpendicular alignment of the molecule to the surface. For subsequently higher surface coverage, its inclination angle rises up to 21° with respect to surface normal and nicely resembles the previous results on this system.

To clarify the structure of more complex systems, buried interfaces in particular, a multiple-scattering approach becomes inevitable. In the course of this work the rather complex zirconium silicide structure, proposed for bulk hafnium silicide [49], will be used with such a multi-scattering approach. Successful multi-scattering investigations were already reported on comparable systems [50]. However, a much higher computational effort has to be put into this kind of system compared to the single-scattering approach of Wesner.

2 Computer Simulations and Algorithms

2.1 Simulating Diffraction Patterns

Yet the technique of XPD has advanced drastically by the use of synchrotron radiation, it is still not possible to retain the surface structure directly from the experimental data, in most of the cases. In contrast, the measurement of diffraction of electromagnetic waves back-scattered from an object with a coherent reference beam allows to record the intensity at a certain point of the wave-field, as well as its corresponding phase. This technique is usually referred to as holography [51]. It enables one retaining the scatterer's spacial information by an inverse Fourier-transform from the k-space of the wave field back into the real space of the scattering object. This method gives an unambiguous three-dimensional picture of the probed object. It even can be applied to x-ray investigations as shown in [52, 53]. In the case where the phase cannot be recorded there are approaches present to solve this problem by dealing with phase retrieval algorithms that do not have any need for a reference beam, e. g. the Gerchberg-Saxton algorithm [54]. But unlike in holography the underlying structure is usually not uniquely deducible from the data. For the phase retrieval method, an initial "guess" concerning the missing phase information is needed. Iterative simulations must be performed to approach the true phase for the problem. This method turns out be similar to the structural simulations in photoelectron diffraction as shown below.

Since the interference of electrons is a quantum mechanical effect, the phase information is not observable. Thus, one cannot perform an inverse Fourier-transform in order to retrieve the atoms' positions from experimental XPD data. They only contain the angular distribution of electrons having a certain energy. Presently, there are some approaches available to compensate for the lack of phase information by recording angle-scanned XPD patterns from the same sample with different excitation energies. This method is referred to as photoelectron holography. Up to now, investigations were only conducted for rather simple and known systems [55], as calculations often lead to artifacts that usually cannot be distinguished from true atom sites.

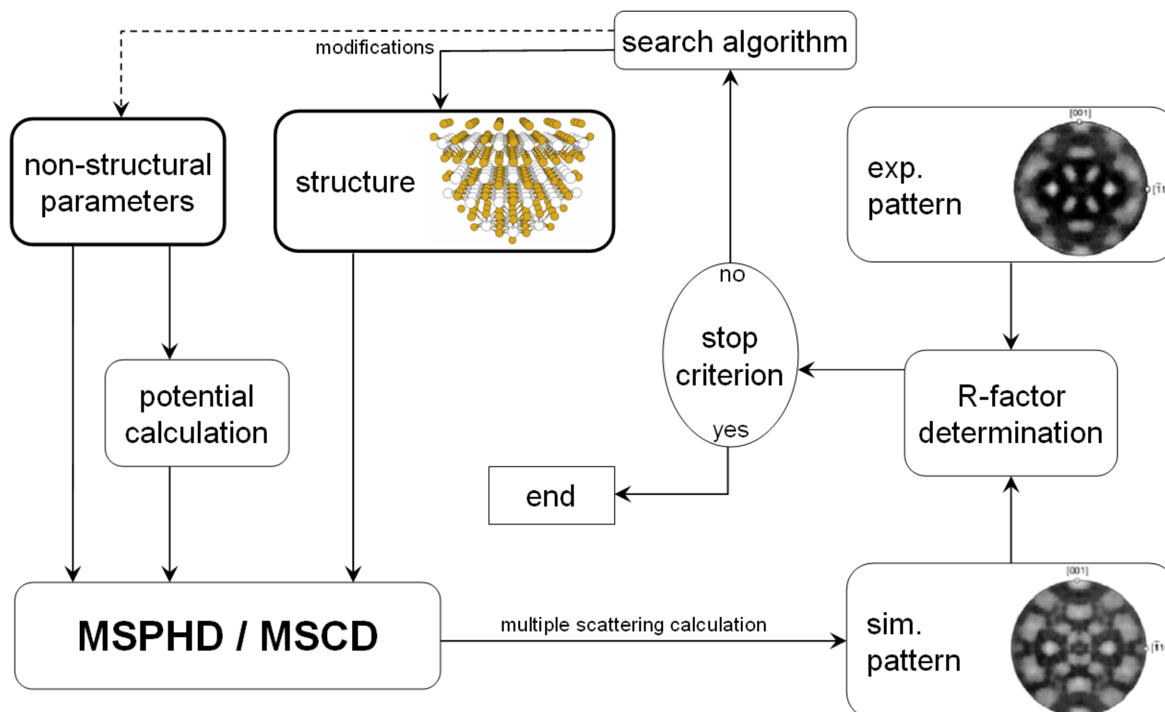

Figure 2.1: Flowchart of a standard XPD simulation procedure. The starting point is the initial guess of a base structure, marked by a bold bordered frame in the schemata.

For the rather complex systems investigated in this work it was inevitable to conduct XPD simulations of model structures and to compare the calculated patterns quantitatively to the experimental results. The course of such a simulation is schematically shown in Fig. 2.1. The initial guess that is necessary here is a base structure, analogous to the initial phase-guess in optical diffraction, as mentioned before. To calculate an XPD pattern from the structure, an atomic potential for every atom in the structure must be considered at first. The potential is approximated by a muffin-tin model in this case. The phase shifts occurring in a scattering event (as discussed in Ch. 1.5) are mainly connected to this atomic potential. Finally, some non structural parameters, as there is the excitation energy, the Debye temperature of the structure, and the work-function at the surface have to be measured, or in some cases estimated. Using all these structural and non-structural parameters a full photoelectron diffraction pattern can be calculated by the programs MSCD [56] and MSPHD [57], respectively. More details on that will be given in Ch. 2.1.1, and Ch. 2.1.2.

The resulting XPD pattern can then be compared to the experimental one (Fig. 2.1). To quantitatively determine the match between calculation and experiment, an R-factor is introduced according to [56, 58]. In particular the R-factor

$$R = R_a = \sum_{\theta,\phi} \frac{(\chi_{exp}(\theta,\phi) - \chi_{calc}(\theta,\phi))^2}{\chi^2_{exp}(\theta,\phi) + \chi^2_{calc}(\theta,\phi)} \tag{2.1}$$

has been used in this work. The quantity χ stands for the so called anisotropy function describing the relative modulation of the photoelectron intensity distribution. An extended explanation can be found in Ch. 5.1. The R-factor, as defined in Eq. (2.1), is in other words the normalized sum of the square deviations between experiment and calculation and comparable to the magnitude χ^2 used with statistical methods. By the definition above, the allowed values of R are in the range of $0 \leq R \leq 2$. Illustrations for different R-factors are displayed in Fig. 2.2. R-factor values close to zero stand for a good agreement, or a good positive correlation, between a calculated pattern and the experimental pattern (Fig. 2.2(b)). For an R-factor of around one, the patterns are not correlated at all. For $R \rightarrow 2$ it is indicated that the patterns are anti-correlated.

Going back to the simulation process, the calculated R-factors suggest changes in the structure model and a restart of the simulation until a certain stop criterion is reached and the process is interrupted, as indicated in Fig. 2.1. What changes are done to the model can be decided in different ways. First, a grid search method can be applied, where a given parameter space, spanned by predefined structural or non-structural parameters of the model, is simply scanned completely. Besides this, there are several search algorithms possible that can be implemented. A more convenient overview of those algorithms will be given in Ch. 2.2.

Even if the base structure for the simulations was chosen correctly, and the global minimum can be found by the simulations, the R-factor unlikely reaches the zero level. On the one hand this is due to the finite size of the model cluster and the cut at a certain scattering order, because

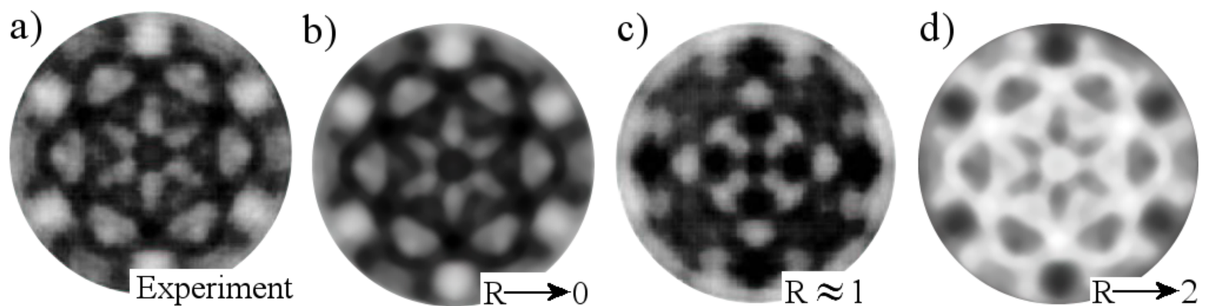

Figure 2.2: R-factor illustrations of simulated patterns regarding an experimental one, shown in (a). Rather good simulation of low R-factor (b), no correlation between experiment and simulation (c), negative correlation between the patterns (d).

of computational limitations. On the other hand the simulations assume a perfectly ordered surface leading usually to a much higher anisotropy compared to the experimental results. Also vibrational damping of diffraction and the experimental angular aperture acceptance, in this work 5°, both of which will tend to smooth out fine structure.

To summarize, finding the correct structural parameters through this method is usually possible, if the initial assumptions regarding the underlying model are correct. Although a certain diffraction pattern can principally be generated by an infinite number of geometries, there are a number of constraints in existing crystal structures that drastically scale the theoretical parameter space. For example, only positive bond lengths are allowed, which in addition can only be altered slightly from their relaxed values. Further more, the elements present in the surface are usually known, and only a limited number of base structures are physically allowed at the first place.

2.1.1 The MSCD Program

In this work,the program MSCD (multiple scattering cluster diffraction) [56, 58] was used for the XPD investigations in the high energy regime, i. e. for Mg K_α radiation as an excitation source. The necessary atomic potential and the phase shifts can be calculated within the MSCD program package, or by separate programs. In this work, phase shift calculations were provided by the program PWASCH (Partial Wave Analysis Schrödinger) [59].

In order to save computing time, the MSCD package uses the Rehr-Albers formalism (RA) [60] in order to reduce the size of the scattering matrices that have to be inverted. To accurately conduct a multiple scattering calculation, the size of the scattering matrix can be roughly estimated by $(l_{max}+1)^2 \times (l_{max}+1)^2$, where l_{max} is the maximum angular momentum that is required for an accurate result of the calculations. For an f initial state, as used for the Hf 4f XPD patterns, l_{max} needs to be in the order of 20 [58]. Using the RA-formalism, the required matrix for an f state is reduced to a size of 15×15. The exact representation of the multiple scattering propagator can be found in [58].

By additionally introducing an automated cut-off, called “pathcut”, for weakly contributing elements like hydrogen, it is possible to reduce the computing time by at least one order of magnitude. Further on, the computing time T_{tot} depends on the number of scattering events that are taken into account. By an improved iterative summing method for the scattering paths [61], T_{tot} can be estimated by $T_{tot} \sim n$, where n represents the scattering order.

The result of the calculation is finally printed into a text file and is further processed by applications developed during this work.

2.1.2 The MSPHD Program

For the results obtained from the investigations in the soft X-ray regime ($180 - 250$ eV excitation energy), the program MSPHD was used to conduct multiple scattering calculations. It is designed to deliver reliable and fast results in a range of $30 - 100$ eV kinetic energy [57]. The program is self containing and delivers sub-routines for all parts of the XPD calculation. The patterns are calculated in four steps:

- At first, an atomic potential relying on the muffin tin approximation is calculated within the so-called "VGEN" routine. This is how the Coulomb potential and the charge density across the cluster, using relativistic atomic charge densities, is calculated. The results are used for calculating the scattering phase shifts by an energy-dependent exchange and correlation potential according to the complex potential introduced by Hedin and Lundqvist [62]. The complex nature of this potential allows for including the effect of the electron waves' attenuation within the solid.
- In the second step, the final-state wave functions are calculated using the symmetry group of the cluster, severely reducing the size of the scattering matrices and thus the computing time of the problem. A variety of symmetry operations are included within the package and are automatically applied to the given atom cluster.
- At next, the atomic T-matrices and the solution of the scattering problem are calculated. For the matrix inversion, the so called "NAG" package [63] is used. The matrices needed to be inverted in this work can be estimated by a size of around 5000×5000 for a cluster of 100 atoms.
- As final step, the angular cross-section for the experimental geometry of the problem is calculated (independently from the solution of the scattering problem). It yields the cross section for an electron travelling along the vector $\vec{k}$ pointing towards the entrance of the analyzer.

A typical calculation of this kind takes between 5 and 30 minutes using a 2 GHz CPU depending on the cluster size and the maximal angular momentum of the electron final-state waves used. More details on those parameters will be given in the course of the work.

2.2 Algorithms

Different types of algorithms were used for analyzing experimental data and the results of computer simulations. Each of them has different advantages and disadvantages. Different computational problems required different approaches to reach a good trade-off between the quality of the results and the required computing time.

2.2.1 The Levenberg-Marquardt Method

For a further interpretation of XPS data, for example, it is necessary to decompose XPS-spectra into their different spectral components. Here, a Levenberg-Marquardt algorithm [64] was used to fit an analytical function f to the spectra consisting of data pairs (x_i, y_i). This numerical method uses a least-squares routine to find the best solution to this problem by minimizing

$$F(c) = \sum_{i=1}^{n} (y_i - f(x_i|c))^2, \tag{2.2}$$

wherein the parameter c is varied between the iteration steps. During the optimization, the routine changes smoothly from the inverse-Hessian method to the steepest descent method [64].

The advantage to this method is its numerical stability. As the routine is locally equivalent to the method of Newton, its convergence is quadratic. The implementation of this algorithm led to very long runtimes when a large number spectra had to be analyzed, i. e. in XPD patterns (cf. Ch. 5.1). Also, an analytical function f is needed that cannot be provided in any case (see below).

2.2.2 The Nelder-Mead Method

To be more efficient in analyzing the spectra within XPD patterns consisting of around 8000 spectra, an implementation of the Nelder-Mead [65] algorithm for Java 1.4 was taken from the literature [66] and adapted to the program package that was developed in the course of the work.

The algorithm uses the topological simplex method to approximate the minimum of a given test function without using derivatives. For an n-dimensional problem, an n-dimensional polyhedron

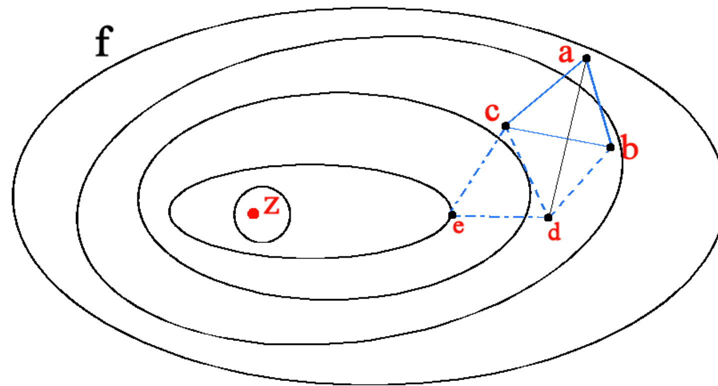

Figure 2.3: Schematic of a simplex algorithm.

with n+1 corner points is defined. The polyhedron is called a “simplex”. A sketch of such a problem is displayed in Fig. 2.3. In the case of a two dimensional problem the simplex has the form of a triangle. The point z stands for the (unknown) minimum of a two dimensional function, sketched by level curves.

The first simplex is given by the triangle (a,b,c) with $f(a) > f(b) > f(c)$. To generate the second simplex, the point (or vertex) with the highest value, in this case a is reflected with respect to the axis between the vertices with lower values, generating the first iteration simplex (c,b,d). In the next step e is generated, and so on, until a certain stop criterion is fulfilled. The accuracy of this base method is limited by the size of the initial triangle. To significantly enhance the accuracy of the procedure, Nelder and Mead allowed expansions and compressions of the triangles for each iteration.

This algorithm allowed an automation and a significant runtime drop for XPS fitting procedures. However, the convergence of this method is only proven up to two dimensional problems, yet. Also, the starting conditions must be chosen carefully, otherwise it is likely to end up in a local minimum. Because of this, some of the spectra of each photoelectron diffraction pattern were fitted by a Levenberg-Marquardt method for determining adequate starting conditions.

2.2.3 Genetic Algorithms

For the R-factor analysis between experimental and simulated diffraction patterns both of the algorithms described above are insufficient due to the necessary computing time for each diffraction pattern. If an analytical function f is available in the problem, each of the test values, which have been called $F(c)$ in the case of the Levenberg-Marquardt approach and vertex in the

Nelder-Mead case, can be calculated in a time scale of milliseconds. Within the R-factor analysis no analytical function is available. Every single test value, in this case the R-Factor between the patterns, requires the calculation of a photoelectron diffraction pattern. This takes around $5-30$ minutes and the runtime of the Nelder-Mead algorithm would arise by a factor of around 10^6 in comparison to a similar problem with a known function f. In addition, the parameter space that has to be searched in an XPD R-factor analysis is usually much larger than in the case of a peak fitting problem as described before.

Based on these facts, it was decided to implement a genetic algorithm (GA) to solve this kind of problem. In contrast to the first two methods introduced here, this kind of algorithm is non deterministic. This means that the same set of starting conditions does not lead to the same iteration steps each time the algorithm is started. This kind of approach is called probabilistic, or stochastic.

The main principals of this kind of algorithm are very similar to the basic principals of evolution in nature. This is why biological schemes are usually used to label the building blocks of this method. A set of key parameters c_i is called the “chromosome”, the parameters themselves are called “genes”. The whole of the chromosomes existing within one iteration step is called the “population”. The literature about that kind of algorithm is sizable, raw models that have partially been used to develop the GA in this work, can be found in [67] and [68], for example.

Applying the new glossary to the two dimensional simplex method, for example, would mean that every simplex has a population of three chromosomes, while everyone of which consists of two genes. Iterations within a GA are calculated by procedures called “generation”, “selection”, “crossing”, and “regeneration” (“mutation”). The basic mechanisms of the GA developed in this work are sketched in Fig. 2.4.

generation The first set of chromosomes, the first population, is generated using a random number generator. A reasonable range $[c_{i,min}, c_{i,max}]$ of allowed values is specified for every single parameter c_i within a chromosome in advance. While for the gene representation itself whole numbers are usually used, the interval $[c_{i,min}, c_{i,max}]$ is divided up into N_i equidistant grid points. The index n of a grid point can be allocated to the corresponding parameter value by

$$c_i = c_{i,min} + n \cdot \frac{c_{i,max} - c_{i,min}}{N_i}, 0 \leq n \leq N_i. \tag{2.3}$$

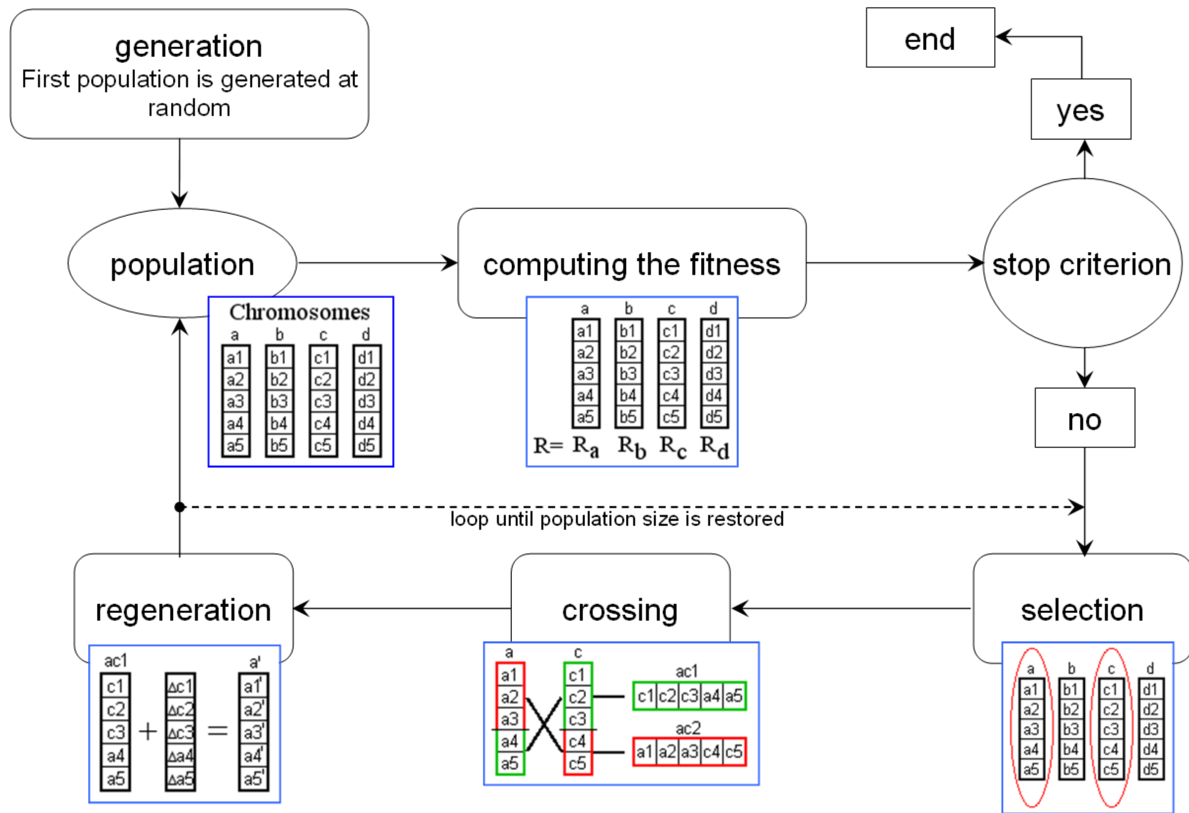

Figure 2.4: Chart of the work principals of the genetic algorithm.

The overall size S of the parameter space is given by

$$S = \prod_i (N_i + 1). \tag{2.4}$$

fitness In the case of the XPD simulations the fitness can be identified by the R-factor of the XPD patterns calculated using the parameter sets (chromosomes). The fitness is important for the further selection (see below) of a certain chromosome. If the R-factor fulfills the stop criterion, i. e. is below a given value, the algorithm is stopped at this point.

selection In this step chromosomes are probabilistically chosen to form the next population. The chance for a chromosome being chosen depends on its R-factor. Parameter sets with lower R-factors are taken into account with a higher probability. There are several different selection strategies. The GA described here uses a selection that can be categorized as “competition”. Six

chromosomes are randomly selected to form two groups of three chromosomes each. Afterwards the ones with the lowest R-factors within their groups are picked for crossing.

crossing The genes of two selected chromosomes are combined into new individuals. Therefore, one or more breakpoints are defined to divide up the chromosome into different parts. Those parts are recombined afterwards to form two new chromosomes (cf. Fig. 2.4).

regeneration This step stands for a special method of applying mutations to the new population. Instead of changing single genes randomly within the allowed range, all genes are altered slightly, depending on the R-factor of their chromosome. This is done by using a Gaussian probability distribution. The maximum of the distribution is set to the old parameter value and its width is influenced by the R-factor. This strategy allows the algorithm to search globally at the beginning, and more locally later, when the minimum of the parameter space is approached.

The implementation used here would allow the interchange of regeneration and crossing. After the last regeneration, a new population is ready for the next iteration step.

The main advantage of a GA is that vast parameter spaces can be searched in very short times, when no analytic test function is available. The transition between global and local behavior can be smoothly changed by varying the width of the regeneration function. Usually the algorithm approaches a possible minimum within the first 20 to 50 generations, which equals a computing time of $1-2$ days, depending on the population size and the sizes of the model clusters used in the XPD simulations. Due to the probabilistic character of the GA, the algorithm slows down in the vicinity of a potential minimum. It is not likely that the chromosome representing the minimum is generated coincidentally. To avoid extended computing times, the algorithm was stopped after an adequate number of generations and the best parameter set so far was used as the starting point for a simplex calculation or a grid search.

Like the other approaches for solving a fitting problem, a GA has several disadvantages that have to be considered:

- The convergence of such an algorithm cannot be proven.
- Depending on key parameters, like population size, and the width of the regeneration function, the effectiveness of the GA can be dramatically changed. Those parameters can only be optimized empirically. For different problems usually different sets of those key parameters have to be used. Further details on that are given in Ch. 5.4.

- A certain minimum cannot be unambiguously identified as a global one. Several calculation cycles on the same parameter space are necessary to verify whether a minimum can be reproduced.
- The GA does not work properly in the vicinity of the minimum, as mentioned above, making the use of deterministic algorithms mandatory.

Only a combination of all the methods described in this chapter can deliver reliable results for the different computational problems occurring in this work.

3 Technological Relevance of HfO_2 and $HfSi_2$

3.1 High-k Dielectrics

Silicides of transition metals attracted recent interest in various fields in surface science: In order to retain the design of MOSFET devices (cf. Fig. 3.1) new materials are needed in the semiconductor industry to proceed in the ongoing miniaturization. The currently used SiO_2 gate dielectric becomes inefficient for ultrathin layers of this material due to increasing tunneling currents through these films. It can be shown that the properties of the layer are sustained down to an oxide thickness of $7-8$ Å [1,4]. These results are reported by experimental as well as theoretical works [4, 70]. But beyond an estimated thickness of 12 Å no further gain in the performance of an actual MOSFET devices are expected [71].

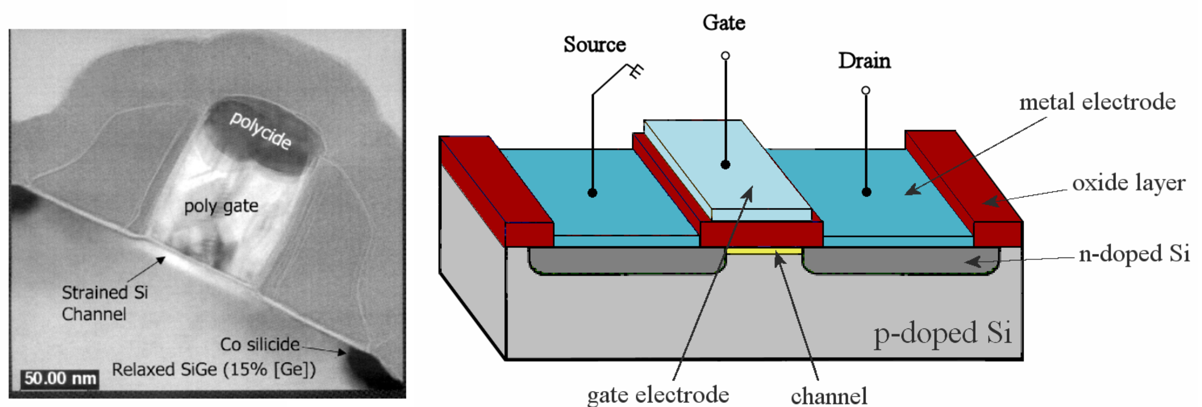

Figure 3.1: A transmission electron microscope (TEM) picture (left side) of an Intel MOSFET device [69]. Schematic view (right side) of the basic MOSFET design. Besides the metal contacts at the top, the different doped areas and the channel region within the silicon wafer are displayed.

Besides this effect, it is desirable to increase the drain current I_D. This leads to a further decrease of the devices' switching time [1]. Thus, the device could work on higher frequencies. The gradual channel approximation (GCA) that is a first order approximation for the drain current within the channel region states that the maximal I_D is connected to the key quantities of the MOSFET by

$$I_{D,max} \approx \mu C_{ox} \frac{W}{L} \frac{(V_{D,max})^2}{2}, \tag{3.1}$$

wherein $V_{D,max}$ is the drain voltage that leads to the maximum desirable field across the oxide, μ is the carrier mobility, W and L describe the dimensions of the channel region and C_{ox} stands for the capacitance of the gate. It was already proposed in 1952 by Shockley [5].

Even in this approximation the GCA states that rising I_D can be achieved by scaling the channel region or increasing C_{ox}. The decrease of the channel length is an ongoing process in the last decades in the semiconductor industry. Modern devices operate with a channel length of below 60 nm. A second approach to increase the performance of a MOSFET is to substitute the SiO_2 layer by a material with a significantly higher capacitance and thus a higher dielectric constant "κ".

Presently, several metal oxides are under investigation as a substitute for SiO_2 [2, 72]. One of the most promising candidates, besides zirconium oxide, is hafnium oxide, which fulfills the basic requirements for the designated application [2]: that is, a high dielectric constant ($\kappa \approx 25$), a large band gap ($\Delta E = 5.7$ eV), and a large band offset to silicon ($\Delta E_{Si} = 1.5$ eV). Today, the major concern is the thermal stability of the system HfO_2/Si(100). During the last five years it was shown that annealing of the system at temperatures above 700°C leads to the formation of metallic $HfSi_2$, which destroys the insulating properties of the dielectric film [73–75]. Although the knowledge of the ultra-thin Hf/Si(100) film-structure is one key to the solution of this problem, the surface structure is still unknown.

3.2 Nanowires

Furthermore, a detailed understanding of the system $HfSi_2$/Si(100) promises valuable information in order to control electronic and geometric properties of structures in the field of quasi-one-dimensional nanowires [77]. Those objects have gained recent interest for various fields of

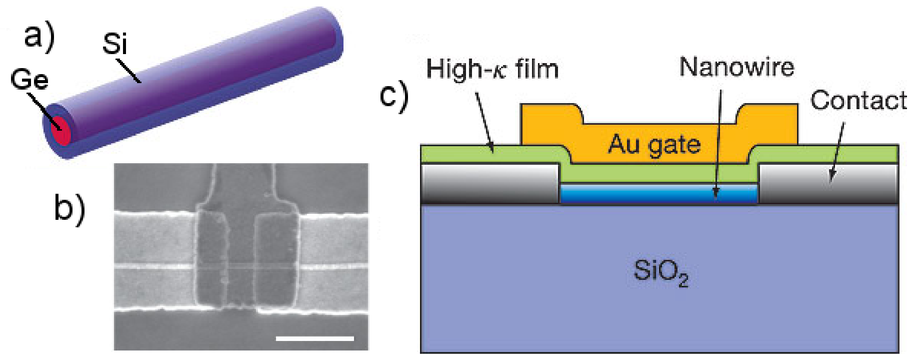

Figure 3.2: Schematic of a semiconducting core/shell nanowire (a) [76]. Transmission electron microscope image (b) of a prototype NWFET device. Schematic of a nanowire transistor. The Si/Ge nanowire replaces the channel region of a conventional MOSFET (Fig. 3.1).

applications. Semiconducting nanowires, for example, together with carbon nanotubes, are potential alternatives for future NWFET (nanowire field effect transistor) devices. Instead of keeping the current design of those devices, as described in Ch. 3.1, one could replace the channel region by a nanowire. By using such a quasi-one-dimensional system it is possible to drastically reduce electron scattering within the channel. NWFET devices using this principle were already fabricated [76]. So-called Ge/Si core/shell wires as shown in Fig. 3.2 can already be prepared with reproducible electronic properties in contrast to semiconducting carbon nanotubes.

In other fields, nanowires ought to work as optical probes for surface scanning applications [78]. For this purpose metal oxide nanowires, like potassium-niobate ($KNbO_3$), are under consideration.

Metallic nanowires gained interest by their potential for use in ultra small electronic devices, to contact NWFET, MOSFET, and CMOS devices, for example [80]. One approach to the

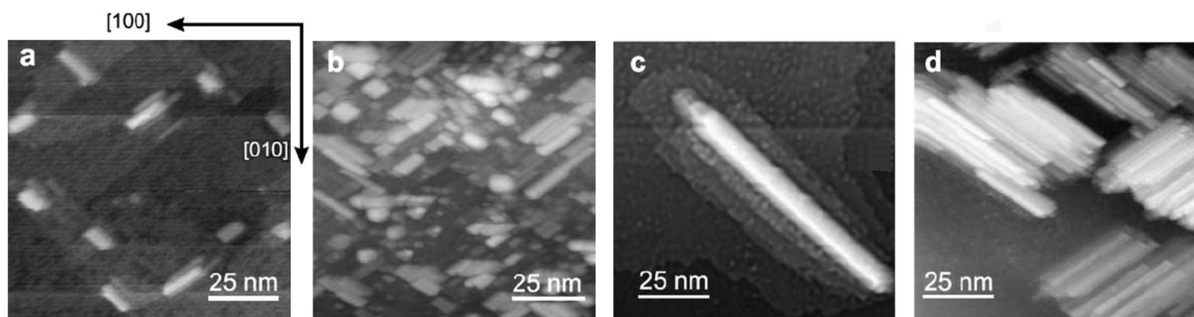

Figure 3.3: Scanning tunneling microscopy images of hafnium silicide nanowires on a Si(100) surface prepared by oxide mediated epitaxy [79].

fabrication of such structures is self-assembly, which can produce features smaller than those possible by conventional lithographic techniques. Among other silicides [81, 82], $HfSi_2$ is under consideration to form self-assembled nanostructures of a high lateral aspect ratio on a silicon surface upon annealing, which mainly depends on the amount of hafnium present on the surface. Nanostructures with an aspect ratio of 70 were already realized by appropriate preparations [7,79] (cf. Fig. 3.3).

The structure determination of the system $HfSi_2$/Si(100) is the subject of this work. Together with spectroscopic and complementary STM and AFM measurements an unambiguous picture of the structure and the morphology of this system will be drawn. Subsequently, the stability of the system HfO_2/Si(100) is tested after using the preparation method of electron beam evaporation (EBE) and is then compared to results in the literature. In a final investigation an attempt to stabilize the system by nitrogen incorporation at the surface is presented.

4 Experimental Setup

4.1 UHV Chamber

In surface sensitive experiments like photoemission very clean surfaces are needed. While the escape depth of low kinetic energy electrons (E_{kin}=50-150 eV) does not exceed a few Angstroms (cf. Ch. 1), even thin adsorbate layers can severely reduce the quality of XPS spectra by damping the photoemission lines and elevating the background of secondary electrons. Also, the chemical composition of the surface layers can be changed by residual gas atoms like oxygen.

To minimize these effects in the experiments presented here, all measurements were carried out in an ultra-high vacuum (UHV) chamber, displayed in Fig. 4.1, and in a comparable chamber placed at the LNLS in Campinas [83]. A turbo-molecular pump and an optional titanium sublimation pump [19] are used to produce a base pressure of around 1×10^{-10} mbar within the main chamber. The transfer chamber is also pumped by a turbo molecular pump and has a base pressure of around 5×10^{-10} mbar. The pressure is measured independently by a hot cathode and a cold cathode ion gauge. According to the approximation of Langmuir [84] an adsorbate layer forms within one second, if the pressure is in the order of 1×10^{-6} mbar. Using a mass-spectrometer it was possible to determine the partial pressures of the residual gas species. It was found that at least 90% of residual gas consists of hydrogen. The partial oxygen pressure that was the major concern in the experiments could be determined to be around 1×10^{-11} mbar, or lower. Based on this, one can reason that the investigated surfaces were hydrogen passivated after 3-4 hours. This conforms to the measured absence of oxygen XPS-signals, even after an exposure to the residual gas of several days.

To conduct in-situ sample movements a manipulator is built into the chamber that allows movements along all three translational directions, as well as rotations around the two main axes of the sample. Stepping motors are used to steer the movements along the z-axis, as indicated in Fig. 4.1, and both the angular directions, which will be referred to as ϕ and θ, are comparable to

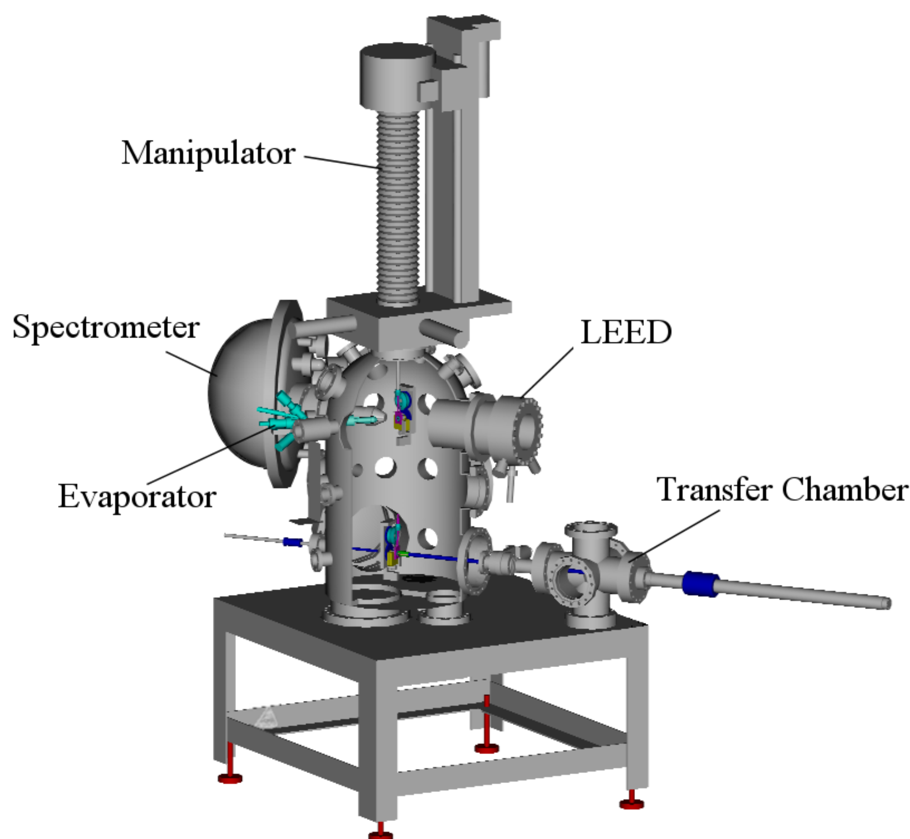

Figure 4.1: UHV chamber for photoemission experiments. All necessary devices needed for the surface characterizations are equipped in the chamber, such as an Mg K_α-x-ray tube, a LEED system, and an electron analyzer.

spherical coordinates. The resolution of the motorized movements is $\Delta z = 1\mu$m, $\Delta\phi = 0.12°$, and $\Delta\theta < 0.1°$.

4.2 Sample Holder

The barrel-shaped holder, displayed in Fig. 4.2, consists of around 35 pieces and has a size of 25×14 mm. The basis is made of molybdenum, while copper is used for the three electrical sliding contacts. The insulation between them is realized by Saphire rings and balls. Through these contacts, semiconductor samples can be annealed by direct heating and can be grounded during the measurement. Currents up to seven amperes can pass the holder. Due to the cylindrical shape of the sliding contacts, the sample holder can be rotated around its main axis (ϕ-axis) without interrupting the contact to earth. Outside the vacuum, the holder is cleaned in an ultra sonic cleaner within a bath of isopropanol (C_3H_7OH).

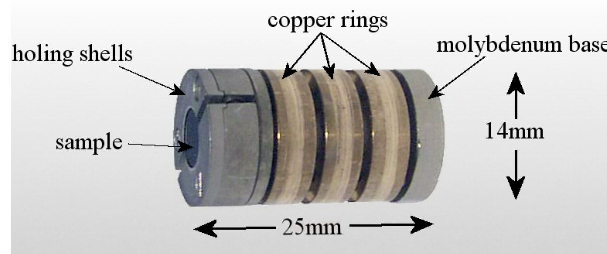

Figure 4.2: Sample holder for semiconductor samples. The sample is mounted at the front end of the holder by molybdenum clamps.

4.3 Analyzer / Detector

The photoelectrons' energy is measured using an energy-dispersive hemispherical analyzer of the type CLAM 4 [85]. A schematic of this kind of analyzer is displayed in Fig. 4.3. After a photoemission event, the electrons travelling towards the entrance of the analyzer pass through a collimator at first. Its aperture mainly determines the acceptance angle of the analyzer, i.e. the angular resolution. Before entering the analyzer by passing through the entrance slit, the electrons travel through a first lens systems and a retarding field of value R that is used to enhance the energy resolution $\frac{\Delta E}{E}$ of the analyzer. This is possible, because the retarding field changes the absolute energy E of the electrons, while leaving the energy distribution ΔE untouched. By this, one can enhance the energy resolution by an order of 10^2. After passing the entrance slit, an electrical field between the inner and outer hemisphere images the electrons onto the exit slit. Electrons not having a certain pass energy, which is mainly determined by the potential ΔV

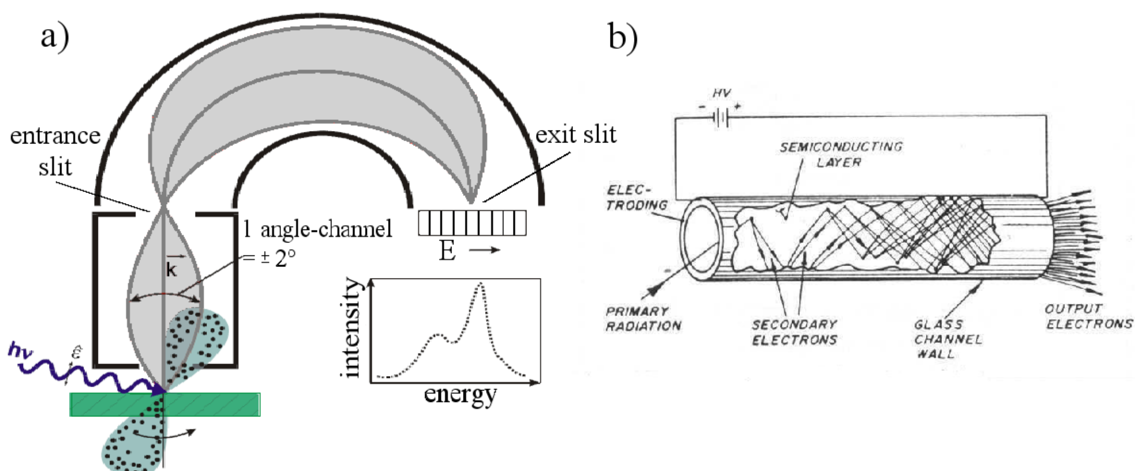

Figure 4.3: Scheme of a hemispherical electron analyzer (a) (a further description is given in the text). Scheme of a channel electron multiplier (b). Some designs use a funnel shaped entrance and a curved channel.

between the hemispheres, cannot pass the analyzer. At the site of the exit slit, the electrons have a kinetic energy of

$$E_{kin} = E_{el} - R - \phi. \quad (4.1)$$

The work function ϕ for the CLAM 4 analyzer is in the order of 4 eV.

To count the electrons leaving the analyzer through the exit slit, an array of nine channel electron multipliers (CEM) was used. Analogue to a secondary electron multiplier (SEM) the impinging high energy particles, in this case electrons, create a significant number of secondary electrons out of a low work function material. In contrast to an SEM, the CEM uses a continues funnel shaped dynode. High voltage is applied between entrance and the end of the funnel for a further acceleration of secondary electrons towards its inner walls. By this, a single electron can produce an avalanche of 10^9 electrons that can be detected as an electrical pulse at the rear end of the CEM. The pulses typically have an amplitude of $5-20$ meV and a width of a few nanoseconds. After further amplification, the pulses are counted by a computer program. Using this setup, up to one million single electron events per second can be recorded.

4.4 Evaporator

The constitution of the system $HfSi_2$/Si(100) and HfO_2/Si(100) is done by evaporating hafnium or hafnium oxide onto the cleaned surface of a sample. An electron beam evaporator (EBE) [86] was used to evaporate these materials. A schematic view of such a device is displayed in Fig. 4.4. The metallic hafnium is evaporated from wires. In order to generate temperatures high enough to melt the metal at the tip of the Hf-wire, its front end is bombarded with electrons. Those are delivered by thermal emission out of a ring shaped filament at the front end of the EBE. By applying a voltage of around 1000 V between filament and wire, the electrons are accelerated towards the wire tip. The deceleration of the electrons within the wire delivers a sufficient amount of energy to heat up the metal up to 3000°C.

Unfortunately, the vapor pressure of metallic hafnium is extremely low and has value of 0.00013 Pa at 2240 K [87]. In comparison, other metals that are typically used in an EBE, like copper or gold, have a significantly higher vapor pressure of 0.1013 Pa at 1800 K [88], and 0.1915 Pa at 2100 K [89], respectively. To compensate for the low vapor pressure, temperatures far above the melting point (cf. Appendix A) were necessary. Hence, a droplet of liquid metal was formed at the tip of the wire during evaporation.

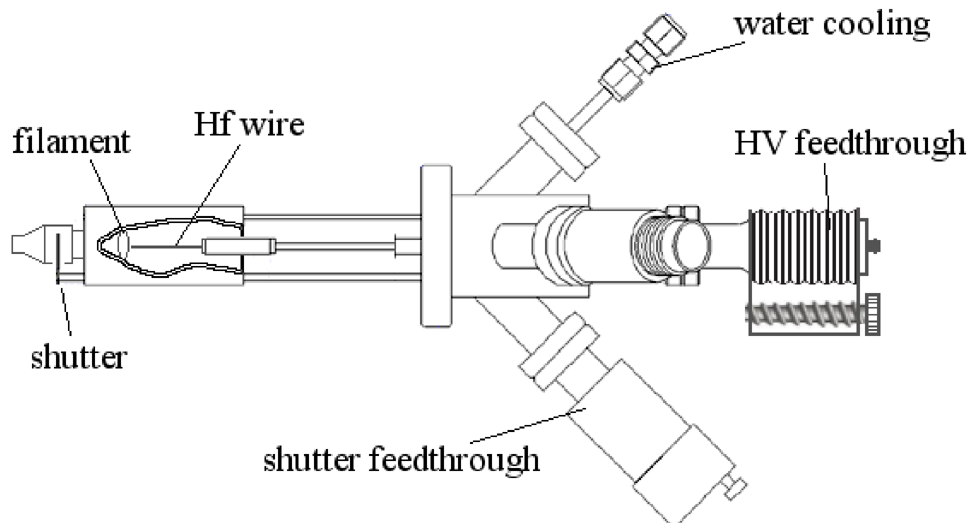

Figure 4.4: Electron beam evaporator used to prepare hafnium, zirconium oxide, and hafnium oxide onto silicon samples.

For evaporating hafnium oxide (HfO_2) or ZrO_2, the front end of the device had to be altered. Instead of a wire, a tungsten basket was placed at the filament's front. By bombarding the cage with electrons, the enclosed hafnium oxide grains could be heated indirectly. Since the vapor pressure of HfO_2 is much higher compared to that of metallic hafnium, the material could directly be evaporated.

Despite the high temperatures within an EBE, the evaporation rate for both HfO_2 and ZrO_2 was rather low. Exposing times up to five hours were necessary to produce nanometer thin layers on the silicon substrates.

4.5 Beamline

For most of the experiments synchrotron radiation was used. Excitation energies ranging from $h\nu = 180\,\mathrm{eV}$ to $h\nu = 600\,\mathrm{eV}$ were required for the different experiments. Throughout the work measurements were conducted at three different beamlines, namely beamline 5 at DELTA, beamline 11 at DELTA, and the SGM beamline at the LNLS (Campinas, Brazil). As an example for the general principles of beamlines for soft x-ray light, a more detailed description of beamline 11 at DELTA is given [18]. A sketch of its assembly is displayed in Fig. 4.5.

Distances are provided with respect to the source, i.e. the middle of the undulator (not shown in Fig. 4.5). Synchrotron radiation is generated within the undulator by an array of permanent

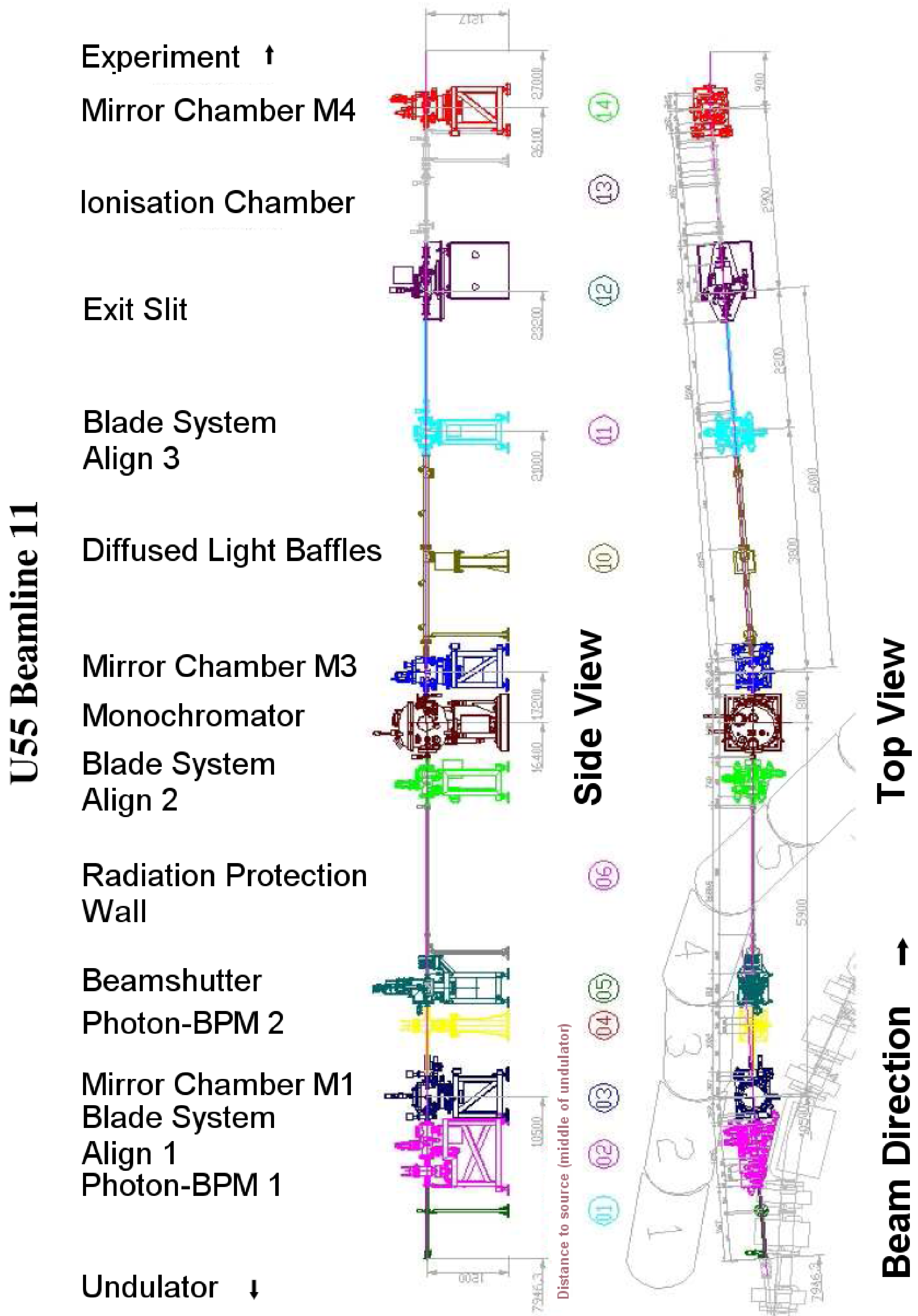

Figure 4.5: Schematic of the plane grating monochromator beamline 11 at DELTA [90].

magnets causing a transverse acceleration of DELTA's main electron beam. While the radiation propagates into the beamline on a straight line, the electrons' trajectory is bent by 7° by a dipole magnet placed between the U55 undulator and the beamline. Since windows mounted within the beamline would fully absorb soft x-ray light, the pressure in the beamline is connected to the pressure in the main ring and has to be kept below 10^{-8} mbar. Partial absorption of the radiation at the optical elements leads to thermal expansions. To ensure the light's pathway through the optical elements, the elements' temperatures are stabilized by a water cooling. Beam-Position-Monitors (BPMs) are used to gauge the light's position within the beamline. They function via several metal blades placed close to the beam. The photoelectric ionization at the blades, induced by the synchrotron light, can be monitored. The relation of the photo-currents measured at different blades hints to the beam's position. The align-systems within the beamline work as collimators. Position and size of the beam can be constrained by blades within these systems. The width of the blades also influences the energy resolution at the experimental site.

To select a certain energy form the continuous synchrotron spectrum and to focus the beam, several optical elements are required. The toroidal mirror M1 absorbs hard x-ray light, while soft x-rays are bent by 4°. Due to its shape the beam is horizontally focused and is vertically collimated. The plane mirror M2 is placed within the monochromator and reflects the light towards a plane grating separating the different photon energies. Two different gratings are available, one with 400 lines per millimeter, and one with 1200 l/mm. An energy range of $55 - 1500$ eV is covered by the gratings. The monochromatic beam is subsequently bent by the mirror M3 onto the exit slit, going along with vertical focusing. M4, finally, is a refocussing mirror imaging the exit slit into the experimental setup. Its image size at the focus plane can be estimated to be $70 \times 200\,\mu$m.

5 Results and Discussion

5.1 XPD Data Treatment

Computational processing of the experimental XPD patterns is necessary in most cases to make the data suitable for use in an R-factor analysis. One effect that has to be corrected for is the inconstant light intensity at a synchrotron light source, for example. But first, the manner in which the design of the diffraction patterns, shown is this work, is obtained from the raw data will be described.

As mentioned in Ch. 1, in XPD the photoelectron intensity is recorded as a function of the two spatial angles $I = I(\theta, \phi)$ as illustrated in Fig. 5.1(a). Thus, the angles are labelled according to spherical coordinates. This is why the polar plot representation of the data covers the surface of a hemisphere above the sample, displayed in Fig. 5.1(b). Each dot on such a surface stands

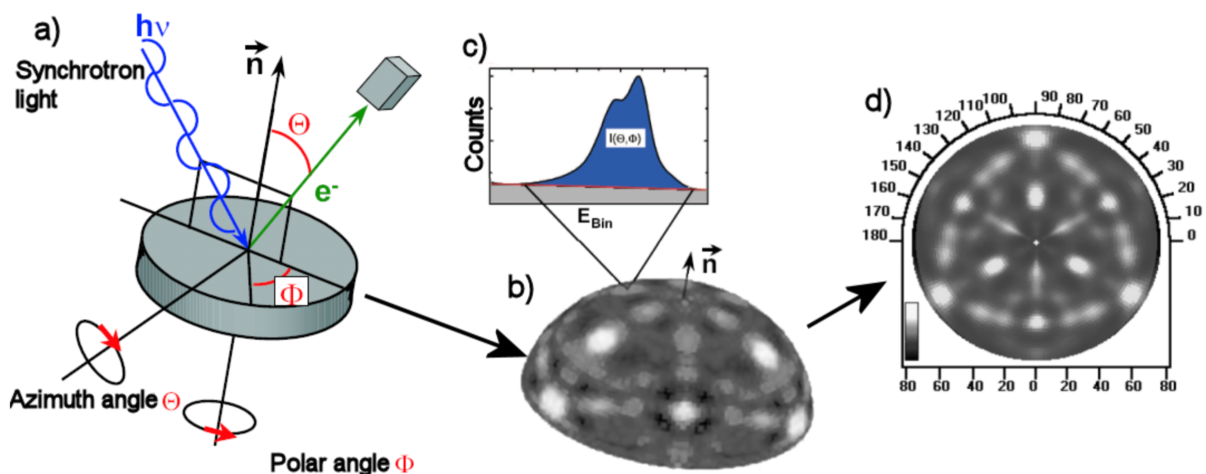

Figure 5.1: Geometry for recording XPD patterns (a). Hemispherical shaped raw data (b), showing angular depending diffraction effects. Illustration of an XPS spectrum (c). Its peak area is transferred into one spot of the color image in (b). Projected XPD pattern (d).

for the integrated intensity of the XPS spectrum taken under the corresponding angle pair, as illustrated in Fig. 5.1(c). Brighter colors would mean a high signal strength and darker colors would mean a less photoelectron signal. The sample holder (cf. Fig. 4.2) was rotated in oder to obtain such a pattern, instead of moving the hole analyzer setup. The pattern's color scheme can be freely chosen, of course. For all the patterns shown in this work, a simple linear gray scale has been used.

For more clarity the hemispherical surface is usually projected back onto the surface plane, as one would look onto the hemisphere from above (Fig. 5.1(d)): $I = I(\theta, \phi) \rightarrow I = I(r, \phi)$. Instead of projecting the pattern by $r = \cos(\theta)$, as one would suspect from the geometry of the problem,

$$r = \tan\left(\frac{\theta}{4}\right) \tag{5.1}$$

is chosen. Again, this is only done for clarity's sake. As a result, the distortion of the outer angles is relaxed and the diffraction features for high θ can be observed more easily. The transformation described above only affects the visualization of the patterns. Hence, for the comparison with the simulated patterns, the function $I = I(\theta, \phi)$ continues to be used.

The separation of the modulating part, i. e. the diffraction effects, from the non-oscillating background signal and arbitrary fluctuations, is more important than the visualization of the patterns. As a first step, the background of secondary electrons is removed from all off the spectra recorded, as already denoted by the gray area in Fig. 5.1(c). For photoelectron lines appearing on a smooth background in a PE spectrum without vicinal Auger or other PE lines, the so-called Shirley background [91] turns out to be a good approximation to calculate the amount of secondary electrons generated by the peak. The main assumption made by Shirley is that the overall background U generated by a certain peak containing n points, is proportional to the peak area towards higher kinetic energies:

$$U = u \cdot \sum_{i=1}^{n} c_i = uI \Leftrightarrow u = \frac{U}{I}, \tag{5.2}$$

where c_i is the count rate at a certain point i in the spectrum. The constant u can be seen as the background proportionally generated by a single count of the main peak. The background U_i at a

certain point i of the spectrum can then numerically be calculated by evaluating the fractional peak area I_i generated over the interval $[c_i,c_n]$ by

$$U_i = U \cdot \frac{\sum_{k=i}^{n} c_k}{I} = u \cdot \sum_{k=i}^{n} c_k \qquad (5.3)$$

generating a curve with a positive slope towards lower kinetic energies that shows inflection points below the maxima of the spectrum. This is not surprising as long as U is more or less proportional to the area of the peak function.

In a second step, attention is drawn to the function $I(\phi)$ at constant θ, i. e. to the intensity distribution within one polar angle. An example for such a function is shown in Fig. 5.2(a). It displays the modulation within one ring of the Si 2p pattern shown in Fig. 5.2(b). One can observe the four-fold modulations of signal as a function of ϕ. The amplitude of those modulations is usually much smaller than the overall signal. To separate the modulation from the average signal, usually a smooth background function is subtracted, as indicated by the dashed line, and the so-called χ-function

$$\chi(\theta,\phi) = \frac{I(\theta,\phi) - \bar{I}(\theta)}{\bar{I}(\theta)}; \quad \bar{I}(\theta) = \frac{\sum_{i=1}^{n} I(\theta,\phi_i)}{n}, \qquad (5.4)$$

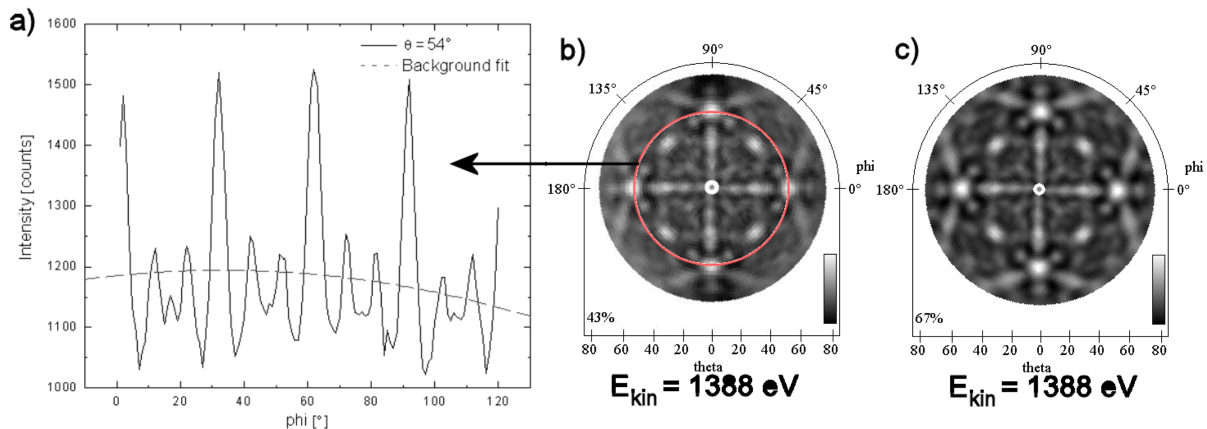

Figure 5.2: Azimuth dependence of diffraction effects (a) extracted from the circle shown in pattern (b) displaying a Si 2p XPD pattern excited by Al K_α-radiation. Part (c) displays the processed pattern after subtracting the background indicated by the dashed line in (a).

is introduced. Thus, $\bar{I}(\theta)$ is the average signal within a ring of constant θ. Finally the χ-function is transferred to a gray scale as described above where black color is assigned to the lowest χ value and white color to the highest one. As long as the gray scale is chosen regardless of the initial amplitude of the modulation compared to $\bar{I}$, the strength of the diffraction cannot directly be derived from such a pattern. To have a measure of it, the maximal anisotropy

$$\chi_{max} = max\{\chi(\theta,\phi)\} - min\{\chi(\theta,\phi)\} \tag{5.5}$$

is defined. It returns the fraction of the modulations compared to the average signal. In this work it is referred to as a percentage quotation in the lower left corner of each diffraction pattern. Since χ_{max} for simulated patterns reflects modulations occurring for a perfect crystal, much higher values are achieved here. Those values usually have no practical use and thus will be left out for most of the calculated patterns shown.

In a last step random fluctuations are suppressed by averaging out the symmetry equivalent positions in the pattern. To justify this step the diffraction patterns must show a certain symmetry from the beginning. For most of the patterns shown here this should be a four-fold symmetry. If this symmetry is not clearly visible before the symmetrization takes place, it is likely to produce artefacts that can have the appearance of a pattern, but do not hold any physical information. At this point one sees the advantage of full-2π pattern over those covering only a fraction of the ϕ-range: the systems´ symmetry can be directly extracted from the raw data, no initial guess concerning the symmetry is required. The trade-off at this point is, of course, that recording a full pattern is much more time consuming.

There are some other enhancements that are necessary in some cases. These will be discussed as they arise. The pattern that is finally obtained is displayed in Fig. 5.2(c).

5.2 Clean Silicon

The substrate material investigation plays an important role for the understanding and interpretation of the systems that will be formed on the silicon substrate later on. The XPS spectra taken for the clean surface will later be compared to those obtained from Hf/Si systems to follow the evolution of the chemical environment of the substrate's surface layers. The second use they have is to check for the cleanliness of the surface.

Diffraction patterns recorded from the silicon substrate will be used for distinguishing diffraction effects originating from the hafnium from those caused by the substrate. They are also important in order to verify the reliability of the simulations using the MSPHD and MSCD program. Therefore, the clean silicon (100) has been investigated using high excitation energies (HE) from a Mg K_α source (hν=1253.6 eV), and low energies (LE) using synchrotron light with an excitation energy of hν =180 eV.

For all the measurements presented here, the silicon samples had a size of 6×8 mm and were cut out of a silicon wafer with a diamond-studded cutting tool. To remove dust and residual contaminations from the surface, the samples were washed with iso-propanol (C_3H_7OH) and dried in air. The final cleaning of the samples, i. e. the removal of the native oxide from the surface, took place in ultra high vacuum by flash annealing at temperatures of around 1000°C for one minute. Afterwards, the surface was reconstructed into the (2×1)-phase with two domains by gradually cooling the sample to room temperature (RT) within a time span of 15 minutes. To verify the reconstruction low energy electron diffraction (LEED) was used. An example of the reconstructed surface, as it appears in LEED, is displayed Fig. 5.3(b).

The XPS results presented in Figs. 5.3 and 5.5 were already reported in a previous work [92]. They are repeated here briefly for completeness and in order to demonstrate the clarity of the new spectroscopic and real space imaging results presented.

5.2.1 High Energy Results

An overview spectrum of the clean silicon surface is shown in Fig. 5.3(a). All peaks are labelled according to the literature [93]. The residual oxygen and carbon signals as well as those of molybdenum do not originate from the sample itself, but from the molybdenum holding-clamps of the sample holder (cf. Ch. 4.2). They are excited within the relatively large area irradiated by the x-ray tube. As we will see for the synchrotron experiments, where the light can precisely be focussed onto the sample site, no impurities are present on the sample itself.

The black dots in Fig. 5.3(b) display the signal obtained from a clean surface and the decomposition in its components. According to the rules of L-S-coupling (cf. Ch. 1.4.2) the intensity ratio between the $2p_{3/2}$ and $2p_{1/2}$ peak is given by $\frac{2\cdot 3/2+1}{2\cdot 1/2+1} = 2:1$. According to [17] the separation between the two peaks is 0.6 eV. The Gaussian doublet that was used here was set to these parameters.

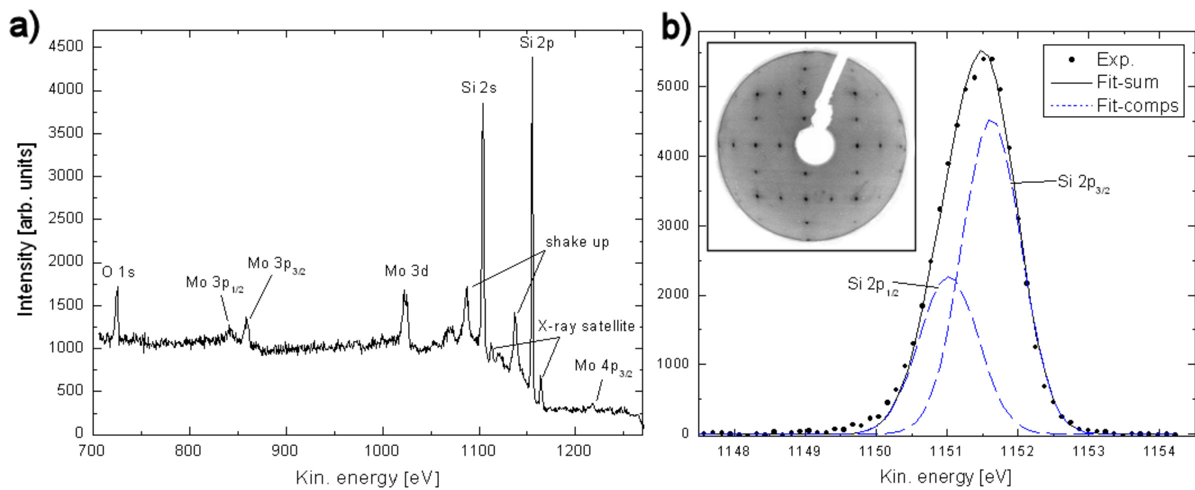

Figure 5.3: Overview spectrum of a clean silicon surface (a). The origin of the impurities is discussed in the text. High resolution spectrum of the Si 2p signal (b) and the decomposition into its components [92]. The inset shows a color inverted LEED pattern obtained from the surface.

The inset of Fig. 5.3(b) shows a typical LEED picture obtained from the clean silicon surfaces of all the samples investigated here. For recording this picture the primary energy of the LEED system was set to E_{prim}=100 eV. To enhance the contrast, the colors of the picture were inverted. Those pictures were mainly used to check for the purity of the surfaces and the presence of the reconstruction and not in the manner they are used in quantitative LEED [94], for structure determinations.

Photoelectron diffraction patterns were obtained from the clean surfaces several times. The result of one of those investigations is shown in Fig. 5.4. The upper part of (a) displays the experimental raw data. In the lower part the processed data are displayed (cf. Ch. 5.1). The raw data are already very much alike the processed data due to the constant flux that a conventional x-ray tube provides. The pattern also exposes very few random fluctuations. Still, the maximum anisotropy of simulated patterns is usually much higher compared to such experiments, because the simulations always assume a non-faulted and fully even surface that produces much less background intensity.

As discussed in Ch. 1.5 computer simulations of model structures are needed to solve the structure of a system by its XPD pattern. A cluster consisting of around 150 atoms was constructed representing a silicon bulk structure. Single-crystalline silicon usually forms in the diamond structure [95]. Therefore it is a cubic fcc-phase (with a two atom basis) and it can be described by only one lattice constant which in the case of silicon is a=5.43 Å. This leads to bond lengths of 2.35 Å. The muffin tin radius of the inner potential was chosen to be 8 % less in

the simulations than half of the next neighbor distance. A section from the model cluster formed upon the structural parameters is displayed in Fig. 5.4(b).

All atoms within this structure are in the same chemical state. Therefore it makes no difference at which of the slabs within the unit cell the cluster is cut, i. e. which of the slabs terminates the clusters' surface. For the systems discussed later on, it will turn out to make a difference. To be exact for the silicon system, one would have to add a (2×1)-phase reconstructed layer to the surface. In the case of the HE investigations the contribution of the surface layer compared to the contribution of the bulk is negligible due to the rather large mean free path for the electrons of around λ=18 Å [96]. For this reason patterns simulated by the MSCD program [56] using the cluster in Fig. 5.4(b) are already in very good agreement with the experimental data. With the order of multiple scattering set to three, the R-factor could be calculated to R=0.15. In the next part of the work it will be shown that comparable results can be obtained for the low energy measurements.

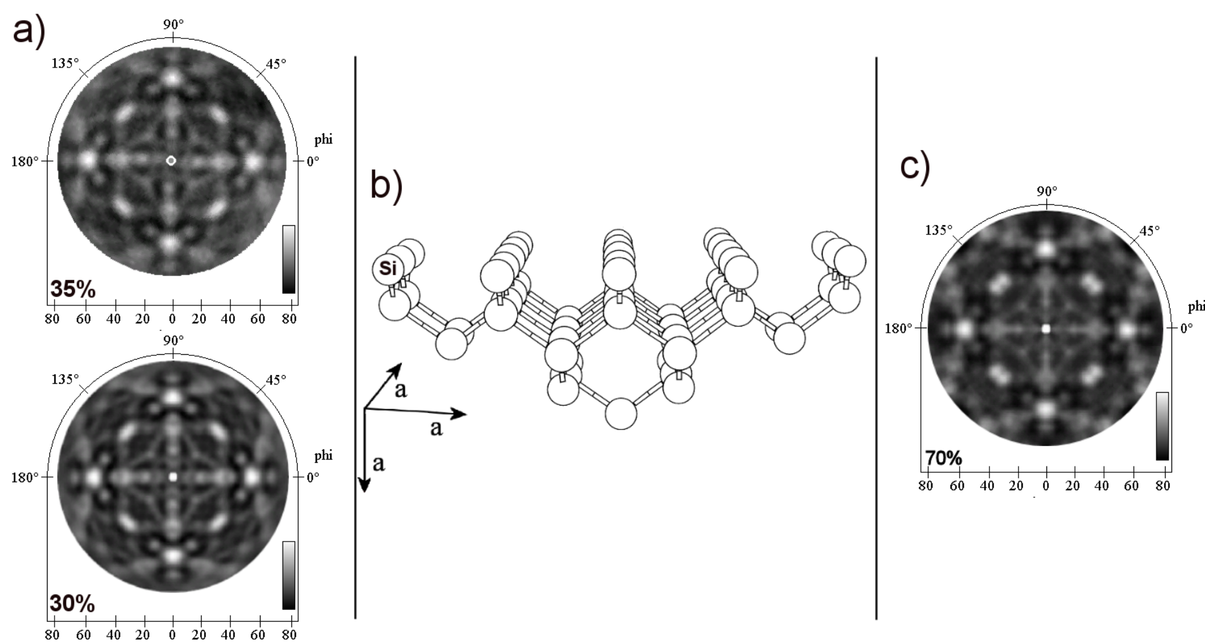

Figure 5.4: Experimental XPD pattern of the Si 2p signal of a Si(100) surface (a), excited with Mg K_α-radiation, before and after background removal. Top and side view of the model cluster (b) used in the simulations for the pattern in (a). Final result of the computer simulations (c).

5.2.2 Low Energy Results

The experiments to be presented next were conducted with an excitation energy of $h\nu = 180\,\text{eV}$ using synchrotron radiation at the DELTA synchrotron radiation facility. An overview spectrum obtained from the clean surface is shown in Fig. 5.5(a). No surface impurities can be found in the spectra. In addition to the photoelectron lines of silicon, the LMM-Auger intensity can be found at a kinetic energy of $E_{kin} = 91.6\,\text{eV}$ [97]. A high resolution spectrum ($\Delta E \approx 100\,\text{meV}$) is displayed in Fig. 5.5(b). The spectrum obtained from the clean surface, indicated by the dotted curve, can be easily decomposed into one bulk and two surface components, according to [42, 98, 99] they originate from the surface reconstruction of the uppermost layer, which can be no longer neglected, in contrast to the discussion of the HE measurements. The left hand component will be referred to as S' in the course of the work. It originates from the uppermost layer of the silicon bulk and its chemical shift with respect to the main line of Si was set to $\Delta E_{kin}(S') = -0.3\,\text{eV}$ (again according to [42, 98]). The other component will be referred to as S. It originates from the surface reconstruction and has a chemical shift of $\Delta E_{kin}(S) = +0.4\,\text{eV}$. The energy separation for the three doublets used in the fit has been set to 0.6 eV [17], their intensity ratio has been set to 2:1.

The LEED patterns for the clean surfaces were identical with the pattern in the inset of Fig. 5.3(b). The photoelectron diffraction investigation of the surface resulted in the pattern displayed in Fig. 5.6(a), showing raw data. Part (b) displays processed data as they appear after background removal, smoothing, and symmetrization. The rather large difference in contrast

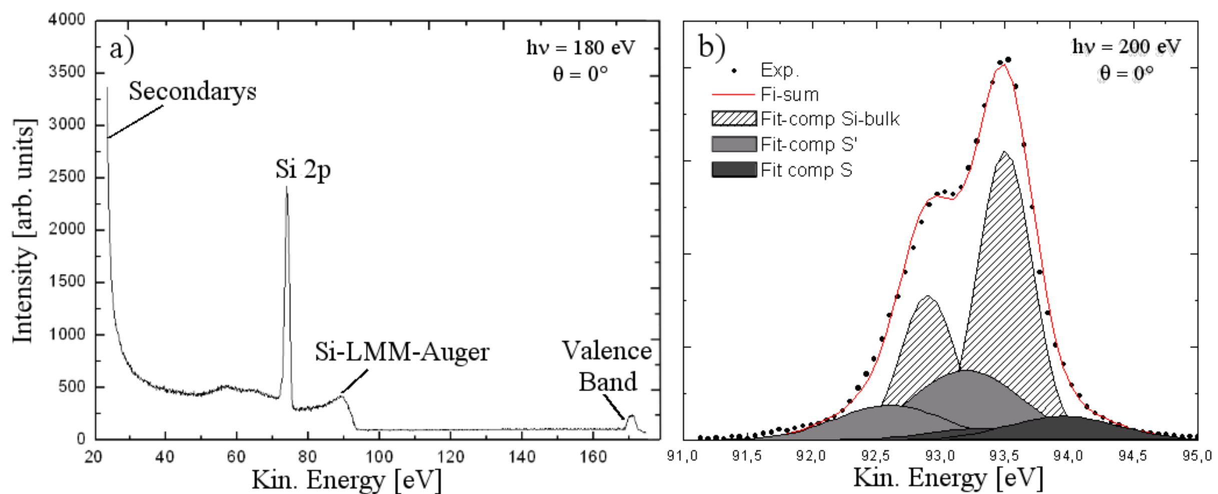

Figure 5.5: Overview spectrum of a clean silicon surface (a). The excitation energy is hν=180 eV. High resolution spectrum of the Si 2p signal of the same surface (b) and the decomposition into its components (see text).

and clearness between those two patterns is typical for synchrotron radiation investigations. Throughout the recording time of such a pattern, around six hours, the intensity of the incident beam is never constant, but decays with time. Since the average intensities $\bar{I}$ are calculated for every single θ-angle (cf. Ch. 5.1) the signals show a gradient in brightness for all θ. For more on the data enhancement, see Ch. 5.4. The comparison of raw data and processed data is very important to verify whether new modulations were created during the data processing. These kind of artefacts would eventually disturb the simulation process.

A model cluster was set up containing around 100 atoms. The structural and non-structural parameters from the HE simulations of this surface were adopted. Additionally, a (2×1)-reconstruction was included on top of the cluster because of the very small mean free path ($\lambda \approx 5$Å) and thus the higher surface sensitivity in this experiment. Simulations were conducted using the program MSPHD [57]. The maximum angular momentum was set to $\ell = 6$. Within a computing time of 40 hours a relaxation of the R-factor to R=0.22 could be achieved, the corresponding simulated diffraction pattern is shown in Fig. 5.6(c). The positions of the two dimer atoms, the first two layer distances, and the number of emitters placed in the bulk served as variables in the calculations. Further improvement seemed probable, but since the general reliability of the simulation procedure was already indicated by these results, the R-factor analysis was stopped at this point.

In summary, three main results can be reported: First, it is evident that the experimental procedures as well as the simulation procedures with the MSCD/MSPHD packages do work properly, if the correct models are assumed. Second, the same model cluster (except for the

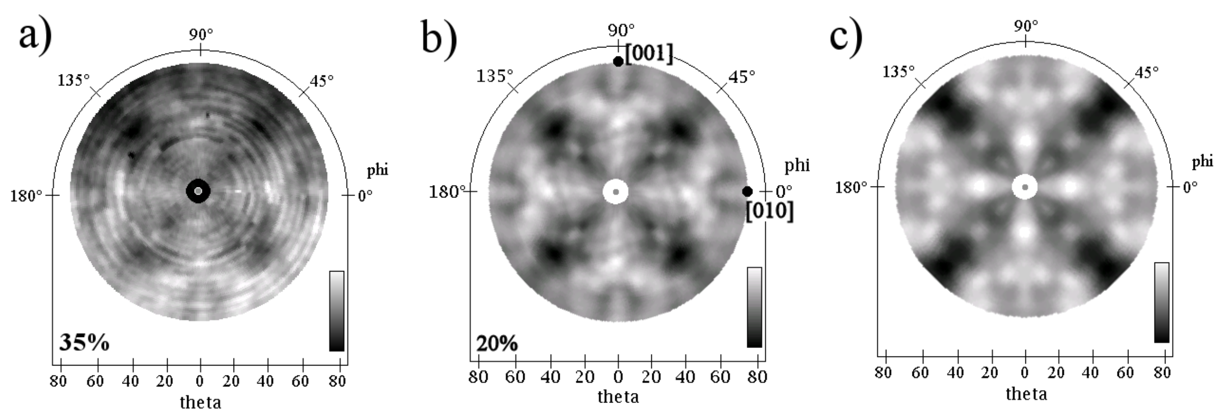

Figure 5.6: Experimental XPD pattern (raw data) of the Si 2p signal of a Si(100) surface (a), excited with synchrotron radiation at hν=180 eV. Appearance of the pattern after the data processing procedure (b). Final result of the computer simulations (c) using diamond-type model clusters.

presence of surface dimers) could be used to describe both the high and low energy experimental results. Two different programs were used, which rules out a coincidental match of the results. Finally, the results are suitable to exclude background effects originating from the silicon in the investigations presented later of, by a direct comparison of the Si 2p patterns with patterns recorded from the Hf 4f signal.

5.3 $HfSi_2$/Si(100) High Energy Investigation

In this chapter the first part of the final results on the system $HfSi_2$/Si(100) is presented. There are two reasons for investigating the system with two different energies, as presented here: First, one can adjust the surface sensitivity by changing the electrons' kinetic energy. The bulk-like behavior of the system may be investigated using electrons of high energy (Chs. 5.4 and 5.5). This includes probing for stacking faults, for example, as discussed below. Experiments using electrons of low kinetic energy are more sensitive to the surface structure. Second, the diffraction patterns' appearance is drastically different at E_{kin}=1100 eV compared to those of XPD patterns recorded at E_{kin}=100 eV. This is due to the different wave length of the photoelectrons. For the HE investigations forward-scattering in predominant, for the LE investigations backward-scattering becomes more significant (Ch. 1.5). Therefore, the two investigations can considered to be independent. For the two energies two different programs were used to conduct simulations. If the same base structure can be used for both the investigations, one can exclude a coincidental similarity between the structural model and the experiments.

Extended experimental details, as well as the evolution of initial results of the HE investigation were already reported in [92] along with the thickness determination of the layers used. In the following, a brief summary of the conclusion will be given. In the current work, the results of the subsequent investigation are reported as published recently [75, 100].

The system is formed by evaporating metallic hafnium onto a clean silicon surface by electron beam evaporation (EBE). Stepwise annealing up to temperatures of 950°C repeatable produces a unique phase of $HfSi_2$ [75]. A high resolution XPS spectrum of the Hf 4f photoelectron signal is shown in Fig. 5.7(a). The additional components found in the spectrum are comparable to those discussed in Ch. 5.2.1 and can be allocated to the oxidized species on the sample holder. These components show no diffraction at all. A sudden decrease of the signal during annealing indicates the formation of islands on the surface. As it will be shown later, this presumption is supported by the new results. The experimental diffraction pattern obtained from the Hf 4f signal is displayed in Fig. 5.7(b). The pattern recorded from the silicon signal of the same sample manifested no

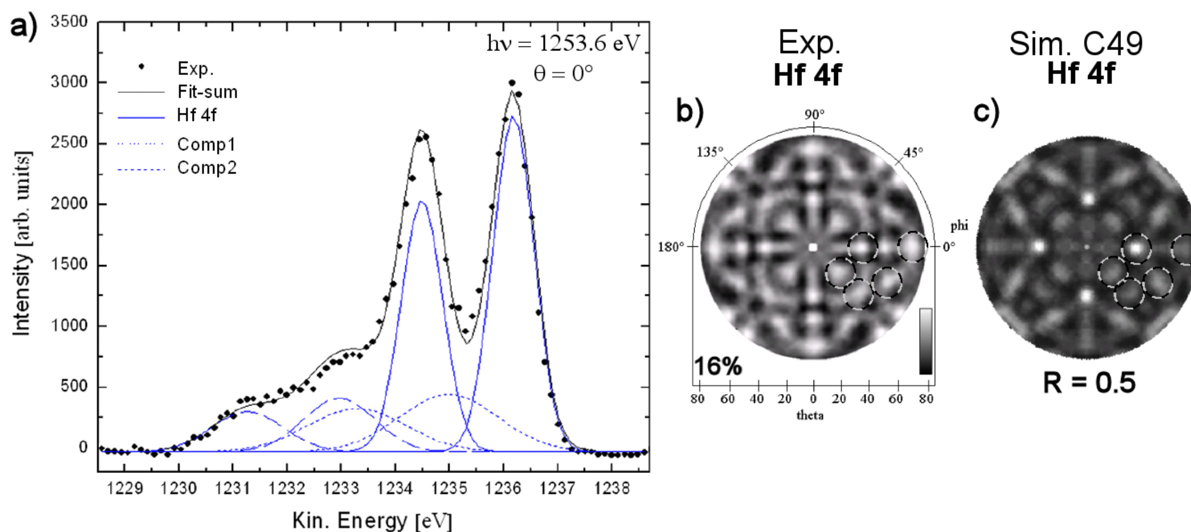

Figure 5.7: High resolution spectrum of the Hf 4f PE intensity (a) [92]. Experimental diffraction pattern (b) obtained from the signal in (a). First calculation result using the C49 structure (c).

visible differences compared to the pattern of the clean surface (cf. Fig. 5.4(a)). This can easily be understood by the bulk sensitivity of the investigation. Assuming a C49 structure for the $HfSi_2$, also called zirconium silicide structure [49, 101], the first XPD simulations led to a calculated pattern as shown in Fig. 5.7(c). Initial relaxations of interlayer distances and the tests for different surface terminations are already included here.

The preliminary result shows a number of matches between experiment and calculation (marked by the circles in Fig. 5.7(b)/(c)). For the continuation of the investigation in this work, it seems reasonable to check for similarities within simulations performed for other structures than the C49 lattice, in order to rule out the similarities being coincidental.

Further structures were reported for transition metal silicides similar to $HfSi_2$, e. g. for $TiSi_2$ [102], in the literature. According to these findings the so-called $C11_b$ and C54 structures were tested for matching to the experimental pattern. The results of the simulations are displayed in Fig. 5.8(b) and (c). The experimental result, as shown in Fig. 5.7(b), is repeated in Fig. 5.8(a) for the comparison with the result of the simulations for the $C11_b$ and C54 structures. For each simulated pattern, the structural model with the optimal surface termination was used. The displayed patterns show only poor agreement with the experimental data. The corresponding R-factors are far above R=0.5. Also, statistically combined patterns for the C49, C54, and $C11_b$ structures were tested to probe for a possible mixture of those phases within the surface. In all those approaches the R-factor could be minimized if the pure C49 phase was used.

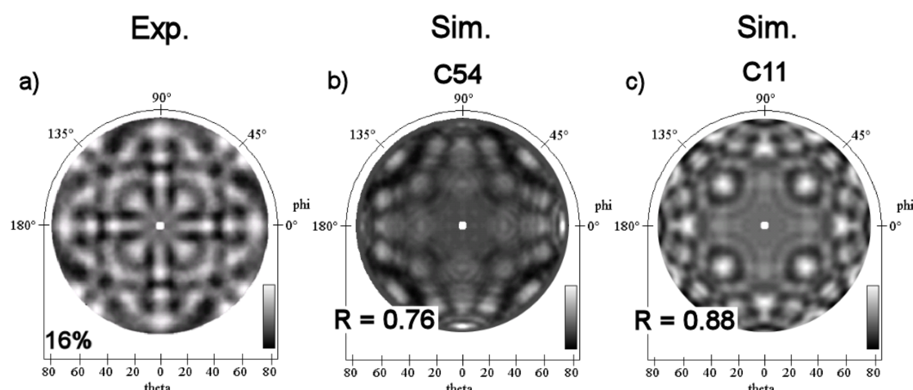

Figure 5.8: Comparison of the experimental results (a) with simulations of different structural models shown in (b) and (c), together with their associated R-factors.

An improvement of the R-factor could be obtained if stacking faults of the C49 structure were included, as predicted for this structure in literature [103]. Two different types of stacking faults are likely to occur in this structure: According to the scheme of the unit cell as displayed in Fig. 5.9(a), the cell (without stacking faults) consists of two equivalent slabs shifted by a lattice parameter $a/2$ with respect to each other, as indicated on the right hand side of Fig. 5.9(a). This structure of transition metal silicides was proposed by Smith and Bailey in 1957 for the first time [49]. Its lattice parameters are a=3.677 Å, b=14.550 Å, and c=3.649 Å. This structure will be referred to as "non-faulted". The structure tends to be rigid at the connection between the two parts of the slabs, where a silicon double layer occurs, i. e. at $b/2$. Both stacking faults to be introduced refer to the alignment between those two parts of the unit cell. The first one can be obtained by a translation of $(a+c)/2$ between them and will be referred to as "stacking fault A" (SFA). The second one results from a rotation of $\pi/2$ around b and a shift of $(a+c)/4$. This one will be called "stacking fault B" (SFB).

For both of these stacking faults diffraction patterns were calculated. The results are shown in Fig. 5.9(b) together with the associated R-factors compared to the experiment. On the first sight the SFA structure resembles the experimental results quite well, while the SFB structure is only in poor agreement with the pattern shown in Fig. 5.8(a). As it is most probable for the true structure to be a mixture consisting of the not-faulted structure as well as the others, statistical combinations of the structures were tested.

The patterns obtained for the different stacking fault structures can be summed up by including their statistical contribution, because the scattering events causing a particular pattern are uncorrelated, hence no interference occurs between different electron emission events. Due to the mean free path of electrons being rather low within the structure, the local emitter environment

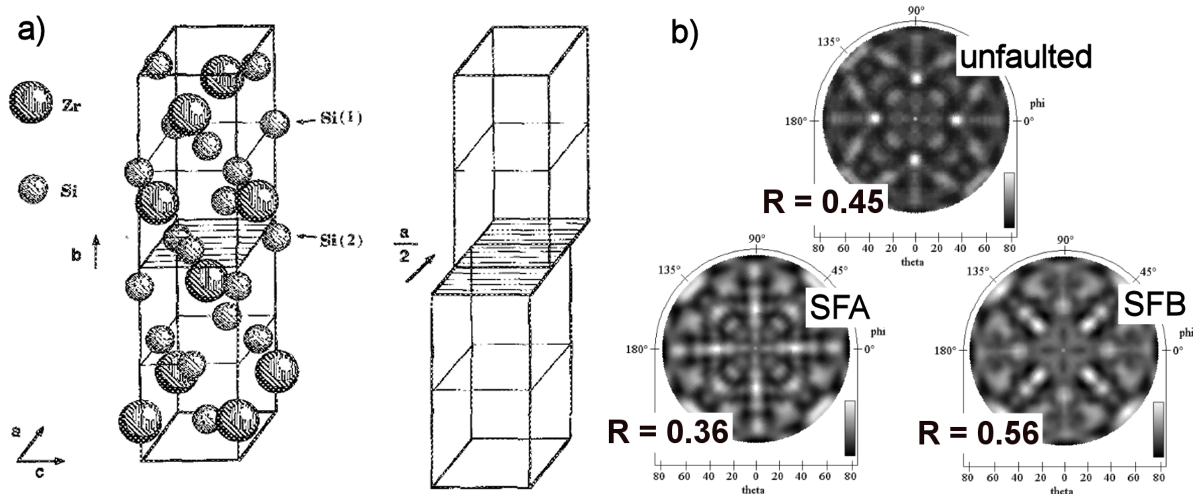

Figure 5.9: Zirconium silicide structure (a), as suggested in [49] for bulk $HfSi_2$. The unit cell can be formed from two displaced slabs. Simulated diffraction patterns (b) for two different kind of stacking faults in comparison with the non-faulted structure calculation.

consists of only one type of the possible structures, leading to one of the patterns in Fig. 5.9(b).

For all possible combinations the lowest R-factors were obtained for SFA without contribution of SFB. The mixture of SFA with the non-faulted structure reduced the R-factor to R=0.30 which is below the value obtained for both the pure faulted and pure non-faulted phases. This suggests both phases are present at the surface. Further on, a rough estimate of the fractions of these two phases within the lattice becomes possible. In Fig. 5.10(a) the R-factors of the resulting patterns are plotted versus the mixture of the structures. The lateral axes show the percentage contributions of the non-faulted phase and the stacking fault A. The contribution of SFB at a certain point of the plot-surface is indirectly given by the residual fraction to fill 100 %. It can clearly be seen that a rising fraction of SFB (towards the top-left corner of the plot) also rises the R-factor of the resulting patterns. The valley along the line where %(SFB)=0 indicates a minimum for a contribution of around %(SFA)=55, and %(non-faulted)=45. The resulting pattern has an R-factor of R=0.30 compared to the experiments. Both experiment and simulation are displayed in part (b) of Fig. 5.10. The circles in the patterns point at the similar features that appear in both of them. For the inner angles, especially up to $\theta = 50°$, the match between the patterns is extremely good. Some of the polar angles expose an R-factor of around R=0.10, compared to the experimental pattern. This indicates a good accordance of the C49 structure together with the stacking faults used with the actual lattice. This can be understood because the diffraction features in the inner angles are mainly caused by deeper layers of the cluster. For the outer angles the main diffraction peaks could still be reproduced, but the fainter

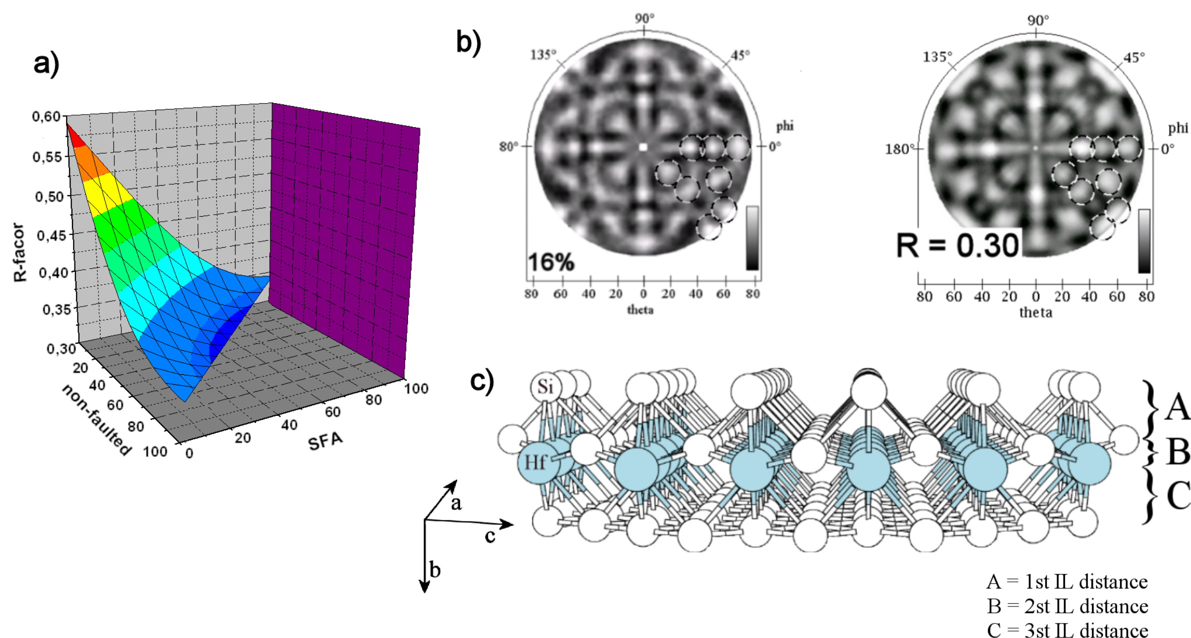

Figure 5.10: R-factors (a) obtained by statistically combining faulted and non-faulted structures (see text). Experimental XPD pattern for Hf 4f (b) and best simulation obtained by the simulations. Model cluster (c) used for the simulation in (b).

intensities in these angles could not be fully resembled. The features appearing for higher θ are mainly influenced by the upper layers of the cluster. One may conclude from this that on the surface either additional stacking faults occur or arbitrary sites are present on the surface, which could not be included in an appropriate way. The main problem here is the rather poor surface sensitivity of the experiments presented. Reconstructions or relaxations only affecting the surface layer cause a small effect on the diffraction patterns. In many cases those effects cannot be distinguished from small random fluctuation of the R-factor, as they occur in the simulations. A clarification of the surface layers, in an experiment more sensible to it, is given in the next chapter.

The uppermost part of the model cluster used for the final simulation are displayed in part (c) of Fig. 5.10. The explicit distances and relaxations included here are summarized in Tab. 5.1 labelled according to the nomenclature in Fig. 5.10(c). For all calculations, surfaces exposing a silicon termination led to the lowest R values. In order to include surface reconstructions experiments with a higher surface sensitivity are required. Those will be presented in the next part of the work.

The R-factor of R=0.30 for the final pattern can considered being rather low, especially when taking the electrons' high kinetic energy into account. The mean free path of photoelectrons with $E_{kin} = 1200$ eV and $E_{kin} = 150$ eV is $\lambda = 18$ Å and $\lambda = 5$ Å, respectively. The mean free path

at high kinetic energies is more than three times larger than at low kinetic energies. Therefore, the cluster size in the calculations for high kinetic energies has to be increased, too. In order to take all important scatter events into account and to ensure a good convergence, the assumed cluster size is $1.5 - 2.0$ times larger than the mean free path of the photoelectrons. With an increase in the cluster size, the number of contained atoms rises as well. This leads to a drastic increase of the parameter space. The maximum possible cluster radius of $r = 24$ Å, as used in this investigation, resulted from the limitations in computer memory and the time needed to calculate patterns for the model clusters. Computing times above one hour were omitted. The limited cluster radius could be one reason for relatively high R-factors at higher polar angles. The computing time for the presented results was around 1200 hours, with an average computing time of 30 minutes for a single pattern. These results were obtained without the use of the genetic algorithm, since the GA was not adopted to XPD in the first year. Later, the GA was applied to the structure search yielding very similar results as obtained by grid-search, but on shorter time scales.

Lattice Parameters [Å]

Parameter	Value	Original
1st IL dist.	1.680	1.717 (= -2 %)
2nd IL dist.	0.638	0.684 (= -7 %)
3rd IL dist.	2.097	2.095 (= ±0 %)
Cluster radius r	20	-
Cluster depth	15	-

Other Parameters

Parameter	Value
No. of atoms	282
Electrons' kin. energy	1239 eV
Inner potential	-8 eV
Order of multi-scattering	3
No. of emitters	5
Stacking faults	SFA & non-faulted
Surface reconstructions	none

Table 5.1: Summary of the final structural and non-structural parameters used in the simulation shown in Fig. 5.10.

5.4 $HfSi_2$/Si(100) - Thin Layer

In this part the results for the low energy investigation using synchrotron radiation of $h\nu = 180\,eV$ are reported. At first, a thin layer of hafnium with an initial thickness of around a monolayer, or 3 Å, was investigated. Most of the results were published in [104]. The experimental procedures are not part of the present work and are contained in [105].

Like in the previous chapter, the experiments were carried out in an ultra-high vacuum chamber with a base pressure below 5×10^{11} mbar. For enhanced surface sensitivity and sufficient energy resolution synchrotron light was used as an excitation source for the experiments (beamlines 5 and 11 at DELTA). After the evaporation and after annealing at 750°C for 10 minutes, photoelectron spectra and LEED images were recorded.

5.4.1 XPS Investigation

An overview spectrum obtained from the surface after annealing is displayed in Fig. 5.11(a). In contrary to the overview spectrum obtained by using a conventional x-ray tube as an excitation source, no impurities can be found, since the diameter of the incident beam was well below the diameter of the sample. Thus, no signals of molybdenum or hafnium oxide (originating from the holding clamps) can be found in the spectra. A high resolution scan of the Hf 4f region is displayed in Fig. 5.11(b). At a first glance, no additional components can be seen besides the main line. As it will be shown later on, the spectrum can be separated into a single doublet of

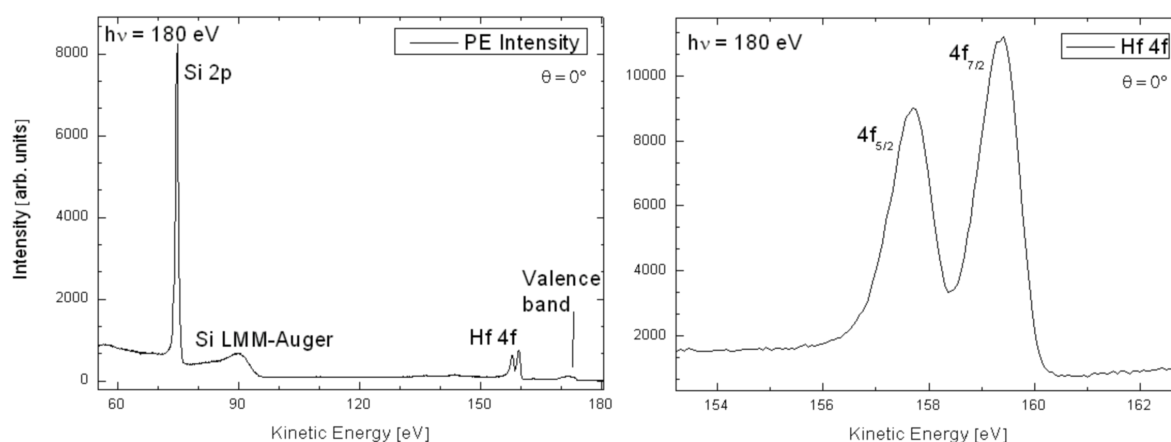

Figure 5.11: Overview spectrum (a) after evaporation and annealing the system. No impurities are visible on the surface. High resolution spectral window (b) of the Hf 4f photoelectron signal.

Doniach-Sunjic profiles. The LEED pictures obtained after annealing were similar to the LEED pattern already given in Fig. 5.3(b), but with a higher diffuse background signal (not shown).

The first important investigation was the clarification of the different chemical species of hafnium and silicon present on the surface. High resolved XPS spectra obtained from the silicon 2p signal are displayed in Fig. 5.12 as they appeared for two different polar angles. As before (cf. Ch. 5.2.2) the silicon signal could be separated into three different distributions. Their chemical shifts regarding to the bulk signal were set as before. There are some key differences visible compared to the spectra obtained from the clean surface. The S' component appears to be much broader than before. This can be easily understood by the origin of this component allocated to the uppermost layer of the silicon bulk. Due to the treatment of the sample, i. e. evaporation of hafnium and annealing (including island formation), the uppermost layer is much less ordered than before. Thus, a variety of almost equivalent configurations exposing only slight differences in their binding energies appear together as a broadened peak. For the spectrum in Fig. 5.12(a) a small gap appears between fit and actual data. It is caused by surface adsorbates. The XPS spectra at lower angles were recorded at a late point of the XPD investigation when the sample already was exposed to residual gas inside the UHV chamber for more than a day. In contrast to the clean surface the S-component of the silicon signal now appears to be more intense. At this point the component is overlaid by the new silicon component bond to hafnium within the islands. Unfortunately the chemical shift of this component turns out to be $\Delta E_{kin}(Si_{Hf}) \approx +0.35$-0.4 eV and is thus almost identical to the shift of the S contribution. For all the measurements presented it was not explicitly possible to decompose these components.

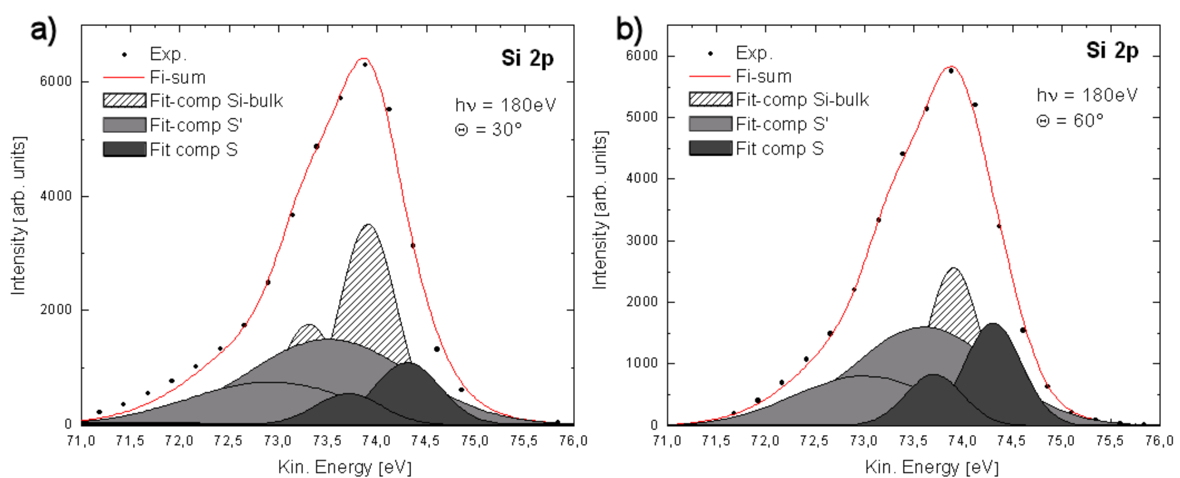

Figure 5.12: High resolved Si 2p spectra and the decomposition in their underlying components. Spectrum obtained for θ=30° (a), and for θ=60° (b). See also text.

Some further information can be derived from Fig. 5.12. Since the spectra were recorded under different emission (polar) angles, part (a) for $\theta = 30^\circ$, and part (b) for $\theta = 60^\circ$, the change of the intensity ratio between the different components holds information about the depth from where a signal originates, according to Eq. (1.5). Under high emission angles the portion of photoelectrons stemming from the surface rises with respect to those originating from deeper layers. Not surprisingly, the relative intensity of the surface and island components (S and S') increases in Fig. 5.12(b) with respect to the silicon bulk signal. This is, of course, the reason why the intensity distribution appears to be different compared to Fig. 5.5(b) as it has been recorded under normal emission. Also, the S/Si_{Hf} components grow relative to the S'-contribution. Again, this behavior is expected since reconstruction and islands are assumed to be above the surface. This behavior was not only checked for in the two angles presented, but in fact for all polar angles of the recorded XPD patterns.

Since it turned out to be difficult to separate the intensity stemming from the islands from the rest of the silicon signal, the Hf 4f peak is the most important photoemission line in this study. Therefore, it is of great importance to understand the peak shape displayed in Fig. 5.11(b). Different approaches for constituting the spectrum by known peak shapes were performed.

For the silicon signal, standard Gaussian profiles were used in this work leading to reasonably fitting results. Fig. 5.13(a) displays the decomposition of the Hf 4f signal by using two Gaussian doublets. Even subtracting the background of secondary electrons left the peak appearing asymmetric. One doublet turned out to be insufficient to resemble the experimental line shape. Using these two components with a chemical shift of $\Delta E = 0.44\,\text{eV}$ leads to a good match between experimental data (dots) and fit (solid line). This kind of fit was applied to the XPD data obtained from this signal. Fig. 5.13(b) displays the diffraction patterns for both of the presumptive components. If the decomposition would denote two *real* components present in the surface, their diffraction patterns ought to look different. The chemical shift of these components indicates slightly different chemical (structural) environments. Since XPD is extremely sensible to such changes, differences in the patterns are expected. In contrast, the diffraction features in the patterns are practically identical. This gave rise to the presumption that the use of Gaussian profiles as an approximation for the peak shapes might be not valid in this case, and the latter peak might hold only one chemical component. If a short lifetime of the state would lead to a significant Lorentzian contribution, the peak would appear as a Voigt profile, as discussed in Ch. 1.4.2. An attempted decomposition into a doublet of Voigt profiles is given in Fig. 5.13(c). The ellipse points to a region where a gap appeared between fit and experiment that could not be avoided by the available parameters. Furthermore, the Lorentzian width used was comparable to the Gaussian one, $w_L = 0.88\,\text{eV}$ and $w_G = 0.85\,\text{eV}$, which is at least surprising. Usually one

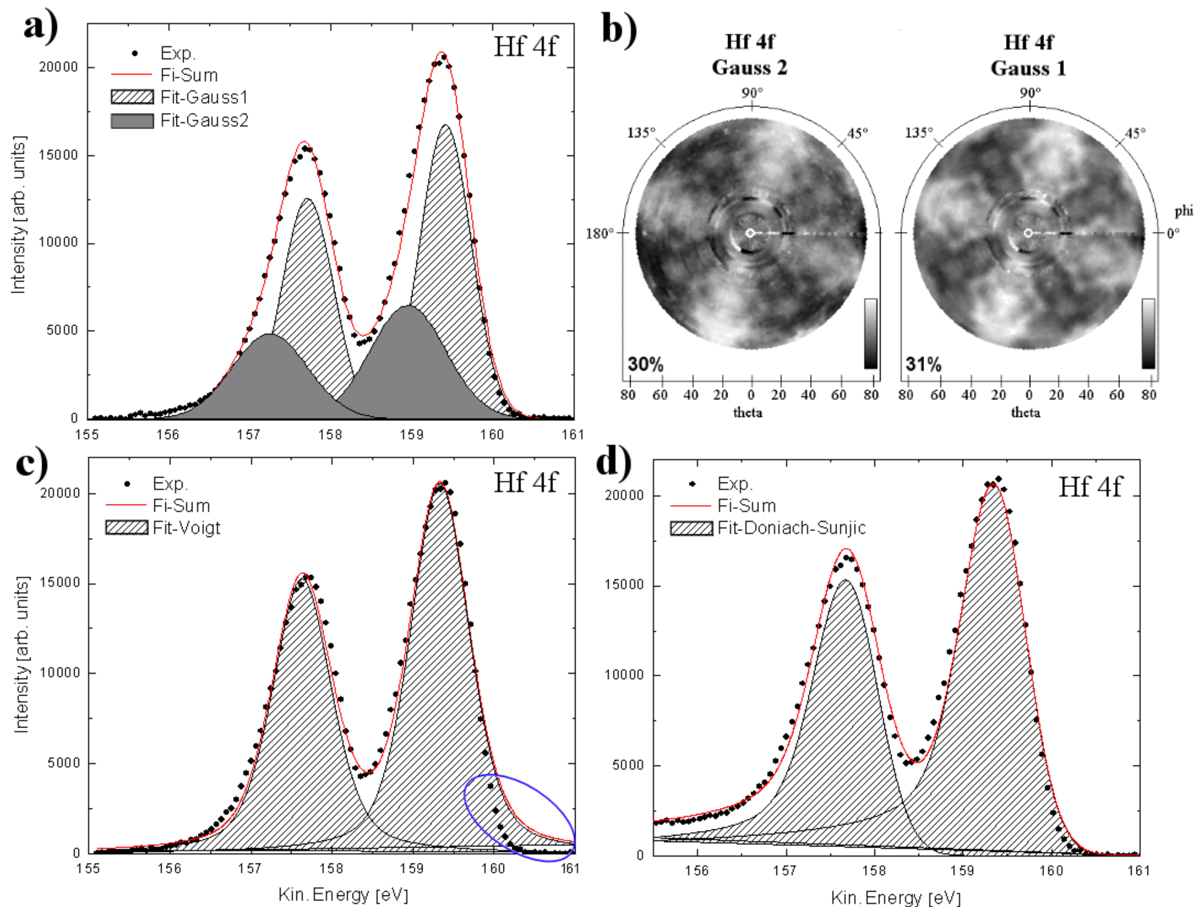

Figure 5.13: XPS spectra of the Hf 4f signal fitted using different theoretical approaches. Two Gaussian doublets (a) and corresponding XPD patterns (b). Voigt doublet (c) and Doniach-Sunjic doublet (d).

would expect a much smaller inherent line width here.

A further peak shape used for XPS is the Doniach-Sunjic profile (Ch. 1.4.2). Due to the asymmetric shape of the profile the background subtraction by the Shirley assumption is no longer valid. Some parts of the of peak, on the side of lower kinetic energy in particular, are mistaken to be part of the background of secondary electrons by the iterative Shirley function. As long as the fraction of diffuse background cannot be definitely distinguished from the contribution of the Doniach-Sunjic profile, this fraction must be taken into account as a variable in the fitting procedure. For the spectrum displayed in Fig. 5.13(d) the best results were obtained by setting the Shirley-background contribution to $\frac{1}{4}$U, where U is the overall background. Obviously this type of profile matches the peak shape much better than the previously discussed Voigt profile. The fact that this kind of profile is usually used for PE signals from metals indicates the metallic character of the hafnium silicide islands, where the whole of the Hf 4f signal is assumed to be

originating from. The fitting procedure's final parameters can be assumed to be quite reasonable: The Gaussian width was set to $w_G = 0.8\,\text{eV}$, while the inherent line width could be kept below 100 meV. The asymmetry parameter was set to $\alpha = 0.13$. The use of Doniach-Sunjic profiles to decompose spectra of hafnium silicide and hafnium nitride (in different phases) was also shown in [73] and [106], but for much thicker initial layers of hafnium where the appearance of metallic characteristics is more expected than for the ultra-thin films presented here.

5.4.2 XPD Investigation

Having only one component originating from the structures, at least within the energy resolution of the experiments, simplifies the extraction of the diffraction effects from the data. Besides the background subtraction, only the area of the hole peak has to be determined. The resulting diffraction pattern, recorded using a $2^\circ \times 2^\circ$ angular increment, is given in Fig. 5.14(a) before and after enhancement of the data. Sudden changes in intensity occur for some of the polar angles and the pattern appears to be noisy. These effects are due the variations in the signal strength of the synchrotron source's incident beam. The azimuth dependent intensity distributions for $\theta = 60^\circ$ and $\theta = 14^\circ$ are displayed as an x-y-plot in Fig. 5.14(b)/(c). These angles were chosen purposely to demonstrate two major effects to be handled. For $\theta = 60^\circ$ the graph exposes smooth,

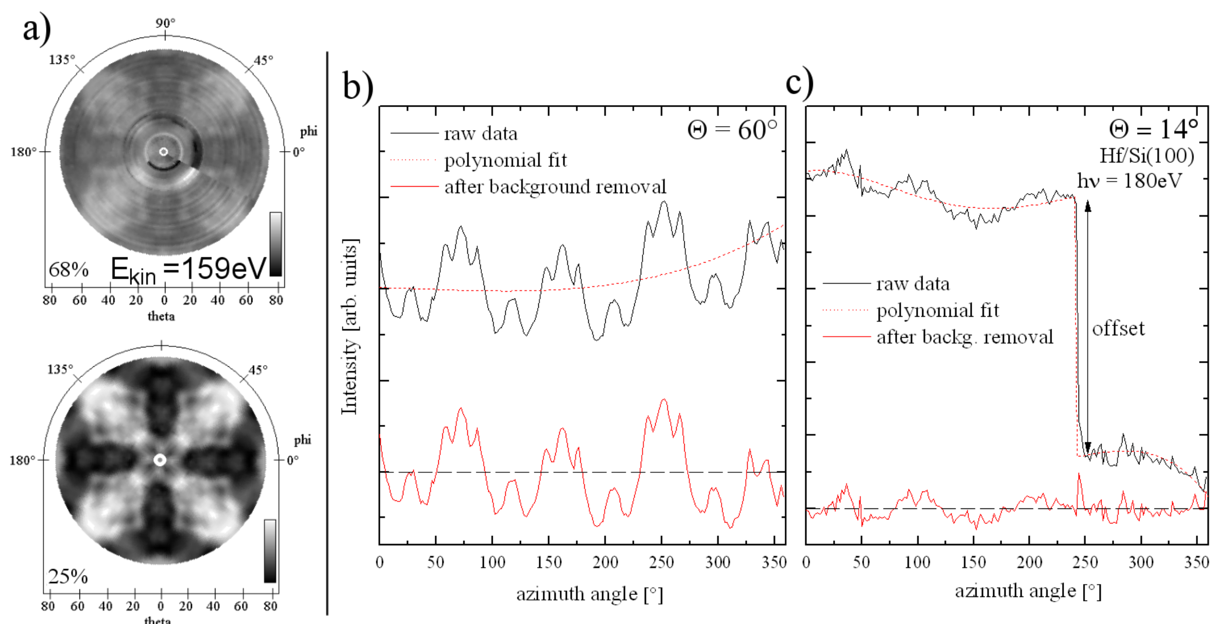

Figure 5.14: Experimental diffraction patterns (a) obtained from the Hf 4f signal before and after data enhancement. Polar scan (b) for $\theta = 60^\circ$ taken from the pattern in (a), and polar scan (c) for $\theta = 14^\circ$. Further details are given in the text.

random fluctuations that could be removed by a 3rd grade polynomial indicated by the dashed line. For $\theta = 14°$, in addition, a sudden step in the overall intensity occurs, which is not an intrinsic effect. As the variation caused by the step is much bigger compared to the diffraction effects, the XPD pattern at this angle exposes only black and white color before and after the step, respectively. These kinds of steps, caused by shifts of the incident beam, were removed manually from the patterns by applying an appropriate offset at one side of the step. The dashed line indicates a fourth grade polynomial function used to calculate the intensity distribution shown in the lower part of Fig. 5.14(c). This function was applied after including the offset. Furthermore, spikes in the intensity occurred for some angles. Those can either be caused by rapid fluctuations of the incident beam and by changes in the grounding of the sample while it is rotated beneath the sliding contacts. Spikes were removed by software routines using a pre-set discriminating window. By applying this routine and those discussed in Ch. 5.1 the diffraction effects in pattern 5.14(a) could be preserved, while no additional artifacts were added during the enhancement. To further suppress random fluctuations, an averaging method regarding the four-fold symmetry of the pattern was applied. The pattern could now be used for comparisons to computer simulations of the system.

For the calculations with the program MSPHD a model cluster had to be set up containing around 80 atoms. The pre-set cluster shape allows semi-hemispherical shaped clusters with a radius r, set to values of around $r = 7 - 10$ Å (cf. Fig. 5.15). In the course of the simulations the cluster radius, and thus the number of atoms within a cluster, was raised up to $r = 15$ Å.

Besides the structure itself, several non-structural parameters are required. Some of them,

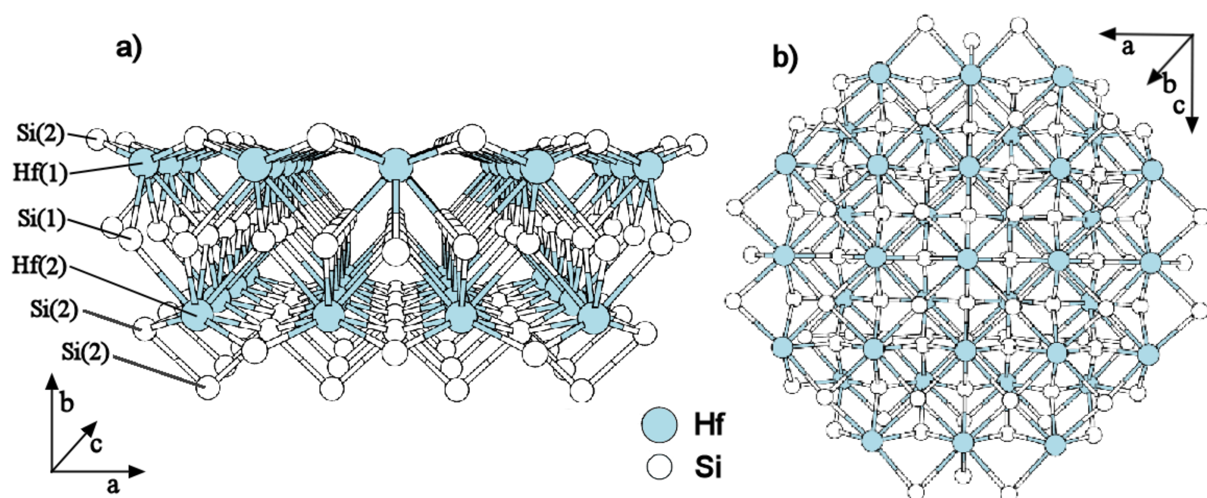

Figure 5.15: Side view (a) and top view (b) of an atoms cluster representing the C49 (zirconium silicide) structure. The layers in (a) were labelled according to [103].

such as inner potential, order of the wave expansion, and Debye temperature were varied during the simulation process. As with the high energy investigation the C49 structure was used as a structural basis for the clusters. Due to the complexity of the unit cell, several surface terminations were again possible. In the soft x-ray regime this uppermost part of the cluster contributes significantly to the appearance of the simulated diffraction patterns. The appearance of the patterns for all five possible terminations, as indicated in Fig. 5.15, are given in Fig. 5.16, each of which was labelled according to its surface termination. The nomenclature was taken from [103]. Most of them are only in poor agreement with the experimental pattern. The Hf(2) terminated surface even delivers a result slightly anti-correlated compared to the experiment, expressed by the R-factor of R=1.3. Only the two surfaces, one terminated by a single layer Si(2), the second one terminated by Hf(1), respectively, resemble the basic appearance of the experimental pattern. Both of them were investigated by an R-factor analysis, but only the results for the Si(2) termination will be presented in detail here. A more detailed view on the Hf(1) termination is given in [105].

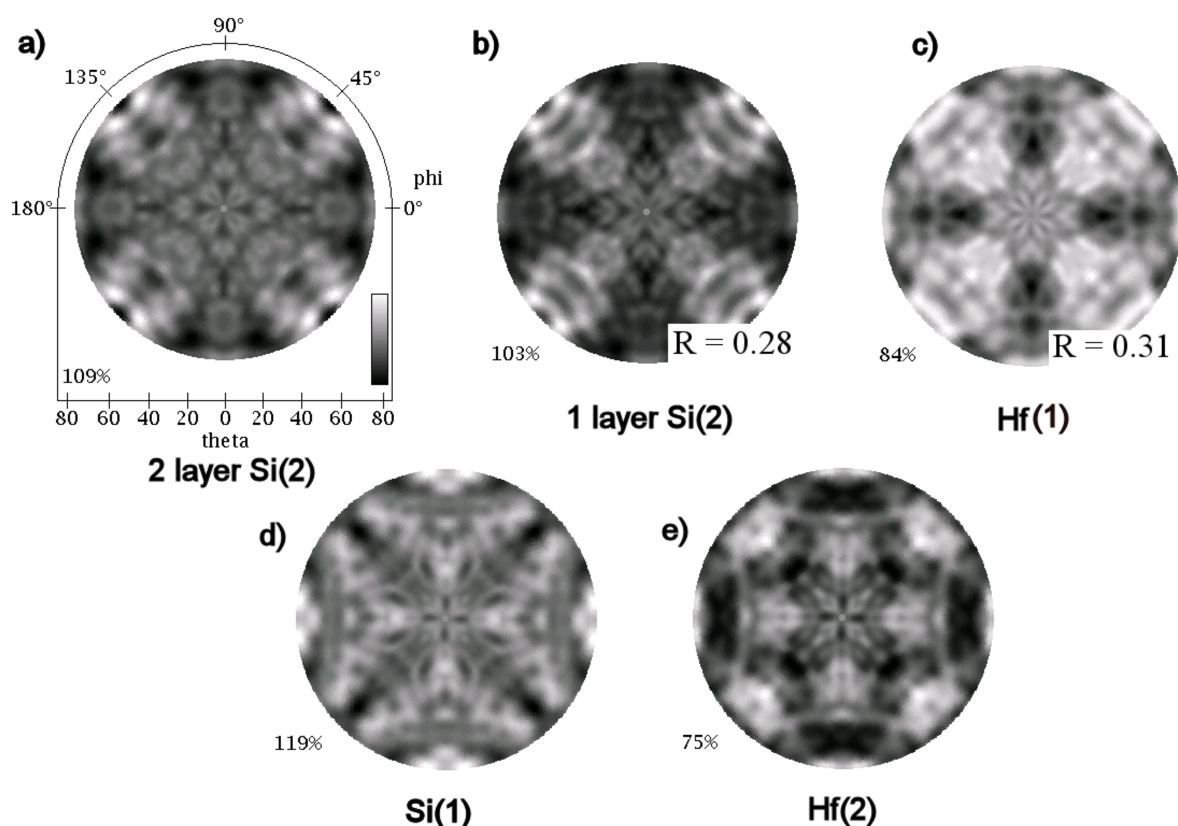

Figure 5.16: Simulated Hf 4f XPD patterns (E_{kin} = 159 eV) of the C49 structure for different surface terminations. Simulations (b) and (c) were chosen for further investigation. The surface termination below each pattern is indicated in Fig. 5.15

Many parameters of the atom cluster and its associated non-structural parameters can be taken into account for the analysis, but only some of them were relaxed at once. A set of three to five parameters was usually chosen for relaxation. For the reasons already given in Ch. 2.2 conventional downhill and simplex algorithms show poor performances on non-analytic minimization problems like an R-factor analysis.

This is why the genetic algorithm was developed and adopted to this problem. As tests using analytic test-functions indicated, population sizes of $10-20$ chromosomes, each representing one set of parameters, had the highest performance on the minimization of these functions. Those results could be verified in tests on an actual R-factor problem, namely the relaxation of the chromosome $\{D1_x, D1_y, D1_z, D2_z\}$, representing the lateral positions of the Si dimers at a clean silicon surface, and their distance with respect to the bulk. This set of parameters was chosen because those parameters were expected to have the biggest influence on the R-factor of a cluster. The results indicate that the Gaussian regeneration of the of the parameter sets led to good minimization results if the width of the distribution was linearly connected to the R-factor achieved by the chromosomes. For the simulations presented here, the width is defined as

$$w_G = I_i(\frac{R_{chrom} - R_{min}}{R_{max} - R_{min}}). \tag{5.6}$$

The parameter I_i stands for the width of the interval of parameter i. R_{max} and R_{min} were chosen with respect to the expected R-factors in a certain simulation procedure. Typical values for R_{max} lay between 0.7 and 1.0. The parameter R_{min} was lowered in the course of the simulation from R_{min} = 0.2 to R_{min} = 0.05 according to the lowest R-factors achieved so far.

Relaxations of a certain parameter-set were usually performed twice or three times to confirm the vicinity where the minimum was found. In cases where even more repetitions of the relaxation led to no unambiguous result, a new set of parameters was simply chosen. This is more likely to appear if parameters were used that only had a small influence on the R-factor. Moreover, at the end of the R-factor analysis when this R measure already achieved values below R=0.15, most of the parameter sets led to no further enhancement of R.

In the cases where the vicinity of a minimum could be confirmed, its exact location in the parameter space was usually probed by a grid search or by manual fine adjustment of the parameters. Again, this procedure turned out to be the most efficient as the GA used here worked quickly on vast parameter spaces, but slowly in the vicinity of the minimum as the parameter

sets are generated at random. Even for relatively low R-factors, and thus a small w_G, it is still unlikely to find the parameter set representing the absolute minimum by chance.

To preserve the results that were already obtained within a simulation, the concept of “elites” was used. This means that the best chromosome found was always conserved and put into the next generation unchanged. By this the R-factor can never increase in the course of the calculations.

A typical runtime for a simulation sequence exceeded between 30 and 50 generations. In fact, it was individually decided by observing the progress in the R-factor. If no progress for more than 7-10 generations was made, the simulations were interrupted. The overall time for a simulation strongly depended on the parameters chosen. The most crucial of them were:

- ➢ cluster size ($30-130$ atoms)
- ➢ wave expansion ℓ ($\ell=5-8$)
- ➢ size of the parameter space (3-5 parameters with $20-40$ grid points each)
- ➢ overall number of patterns (population size $\times$ generations, $(10-20)\times(30-50)$)

From the enumeration above it can be extracted that parameter spaces principally could contain up to 10 million grid points, but a standard simulation usually did not exceed $1-2$ million points. The values above also allow the calculation of the runtime for a simulation procedure, if the calculation time for one XPD pattern is known. Depending on the cluster parameters a simulation took between five and thirty minutes. A runtime of around 10 minutes was common. Overall this leads to a runtime of around 100 hours per relaxation. Taking into account that two CPUs were used reduces the time to around two days. Especially at the beginning of the R-factor analysis much smaller clusters and ℓ-values have been used, coming to a runtime below one day. The overall computing time used for the thin-layer system was not explicitly logged, but can be estimated to be around 1500 hours.

In the following some examples for the relaxation of parameter sets and the development of the R-factor are presented. At the end, the final cluster, its associated XPD pattern, and a comparison to the experimental data is given.

One very significant parameter for every XPD calculation is the cluster radius r. It determines the distance with respect to an emitter atom from where the diffraction of other atoms contribute to the XPD pattern. It determines the total number of atoms within the cluster. The behavior

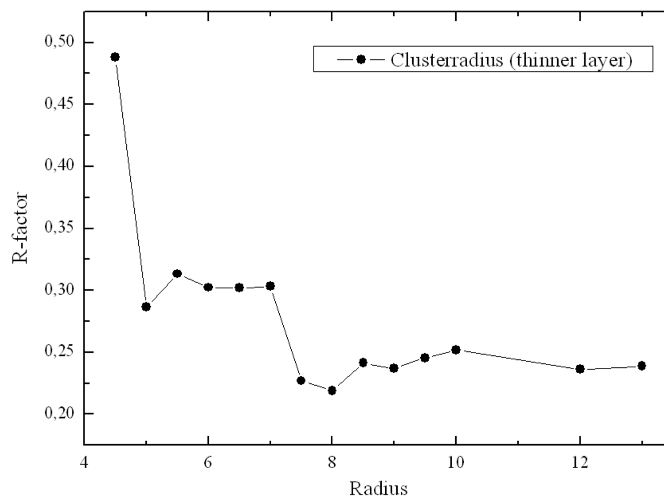

Figure 5.17: Development of the model clusters R-factors by changing the cluster radius and thus the number of atoms contributing to the diffraction patterns. The connector line between the dots was inserted to guide the eye.

of the R-factor by variation of r can indicate either if the chosen structure model is correct, or indicate the size of the ordered structures on the surface.

Fig. 5.17 displays lesser accordance between experiment and simulation for a cluster radius r below 7 Å, compared to larger clusters. By increasing cluster radius and thus a rising number of atoms, the absolute minimum in the R-factor can be found for $r = 8$ Å. Also, for a subsequently larger cluster radius the R-values archived in the simulations are not significantly higher, i. e. they are around R=0.24, compared to R=0.22. Besides the fact that the reliability of the chosen model structure is supported by the results, it points to the presence of ordered structures at the surface exceeding an area at least as large as the models used. In fact, the cluster size in the simulation was limited by the computer memory available. Clusters bigger than $r = 15$ Å could usually not be tested. To save computing time most of the simulations were conducted using a cluster radius of $r = 10$ Å.

Besides the structural parameters, some of the none-structural key values were also used as variables in the calculations. In the following, two examples are given: The influence of the inner potential, and the electrons' kinetic energy on the quality of the simulations. The left-hand side of Fig. 5.18 displays the influence of the kinetic energy. As shown in Ch. 1.5, the kinetic energy of the electrons mainly does not affect forward scattering, but it does effect backward-scattered intensities in the XPD patterns. For small variations of E_{kin} the scattering angles of certain features grow smaller when E_{kin} is increased, and vice versa. The graph in Fig. 5.18(a) exhibits a minimum for a kinetic energy of E_{kin}=160 eV. If one is already sure about the structure used in

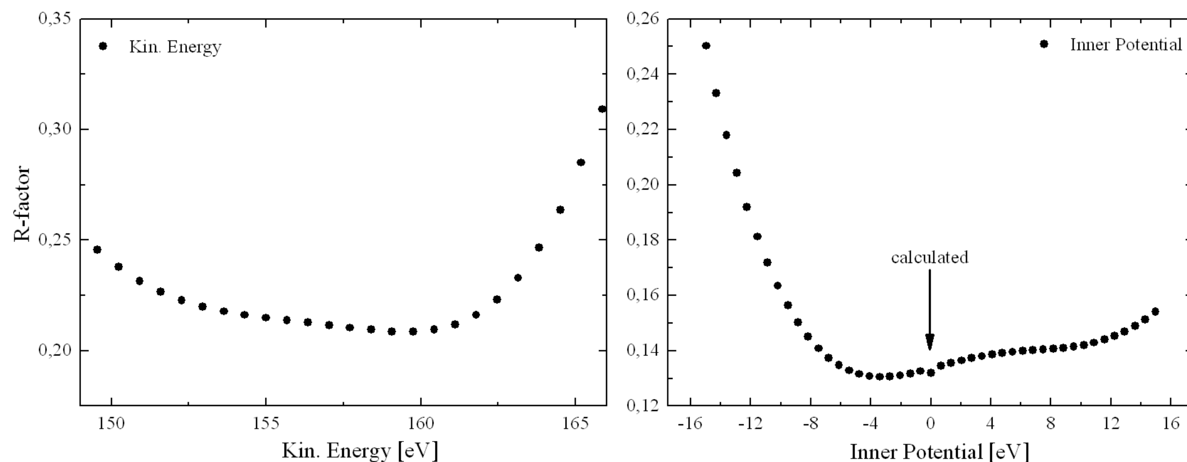

Figure 5.18: Development of the model clusters R-factors by changing the incident beam's energy and thus the kinetic energy of the emitted electrons (a). Variation of the inner potential (b).

the calculations, these results can be used as a measure for the kinetic energy of the electrons observed. But after there are gauges available to determine the kinetic energy of the electrons in the present experiments, it was not necessary to use the results from this relaxation to set E_{kin}.

The right hand side of Fig. 5.18 displays the R-factors obtained from a variation of the inner atomic potential V_{inner}. This number is usually used as a free parameter in XPD or IV-LEED studies. As this quantity influences the absolute kinetic energy of the emitted electrons, its effect on the quality of the simulations is expected to be comparable to the effect of varying the electrons' kinetic energy. Indeed, the obtained R-factor curve appears to be more or less a mirror image of part (a) of Fig. 5.18. The minimum R-factor was obtained for $V_{inner} = -3.5$ eV. For $V_{inner} = 0$ eV the potential is calculated by the MSPHD program leading to a value of $V_{inner} = -4.5$ eV, and an R-factor only slightly worse ($\Delta R \approx 0.004$), compared to the minimum value found. This difference can be considered insignificant. Regarding this result it was decided to automatically calculate V_{inner} in the simulations by the MSPHD program.

The introduction of a missing-row reconstruction led to a significant drop in the R-factor. Besides this surface termination, a double-row reconstruction (cf. Ch. 5.5), dimers (like for the (2$\times$1)-Si reconstruction), and non-reconstructed surfaces were also tested. The second-best result was obtained by using a single missing-row reconstructed surface. On a certain test cluster this surface exposed a minimum R-factor of R=0.135, while a double missing-row reconstruction terminating the same cluster led to an R-factor of R=0.105. From these results and complementary AFM studies on the same system [6,79], even though they were obtained by different preparation methods, it was decided to apply a double missing-row reconstruction to the surface layer, as

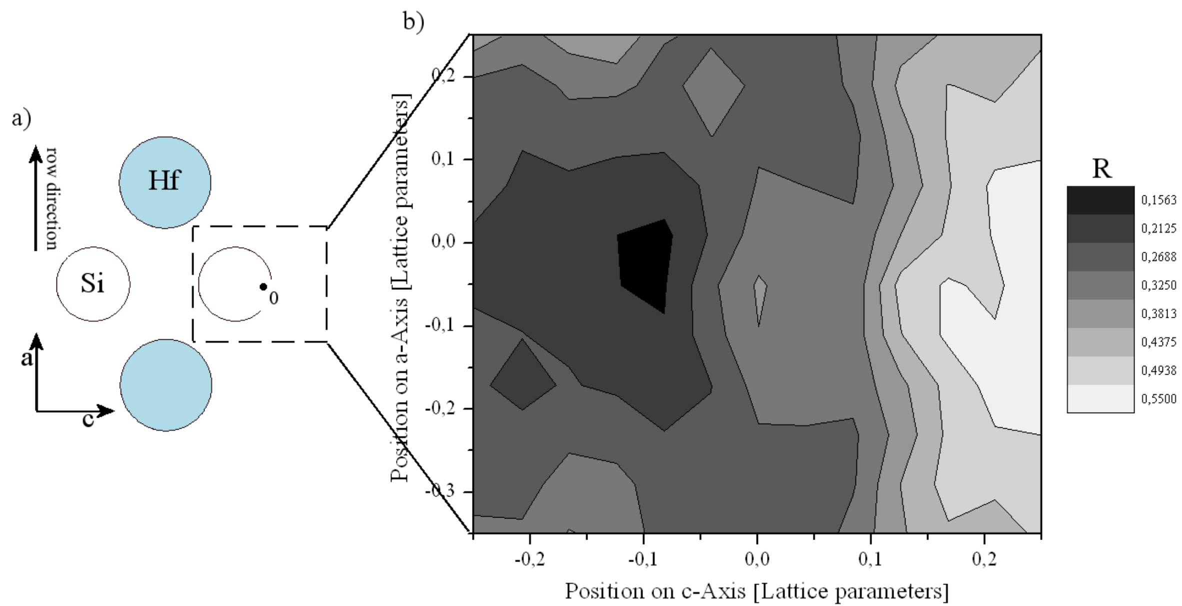

Figure 5.19: Schematic top view (a) onto a fraction of the double row site on top of the model clusters. The direction of the rows is indicated by an arrow. In addition the initial position of the Si atoms in this layer is marked by a zero. The R-factors obtained by varying the *a* position of the rows, and their distance (*c* direction), respectively, within the dashed area, are shown in part (b).

partially displayed in Fig. 5.19(a) and later in Fig. 5.21.

Although the lattice parameters *a* and *c* are slightly different in the basic structure, no significant change of the R-factor could be observed by aligning the row main axis to one or the other parameter. Besides relaxing the interlayer distance with the rest of the cluster, the lateral position of this layer was tested. Here, a grid search was applied to find the absolute minimum in the parameter space. Fig. 5.19(b) displays the results of that investigation. The gray-scale map illustrates the R-factor obtained by varying the lateral position of the reconstruction and the distance between the double rows. In stead of the double-row, only the R-factor space for one of its atoms is shown with respect to its lateral position. The dashed rectangle in part (a) illustrates the searched parameter space. The findings here clearly indicate an absolute minimum at a shift of $\Delta c = 0.1$ lattice parameters away from the original atoms' position in this layer. In the perpendicular direction the simulations indicate practically no shift of the atoms. The associated model cluster will be given in Fig. 5.21. Using this result, the inter-row distance can be calculated to be $d_{row} = 2.43$ Å. The interlayer distance remained quasi unchanged at 99 % of its original value (cf. Tab. 5.2).

At the end of the investigation the model clusters' R-factors were calculated regarding the

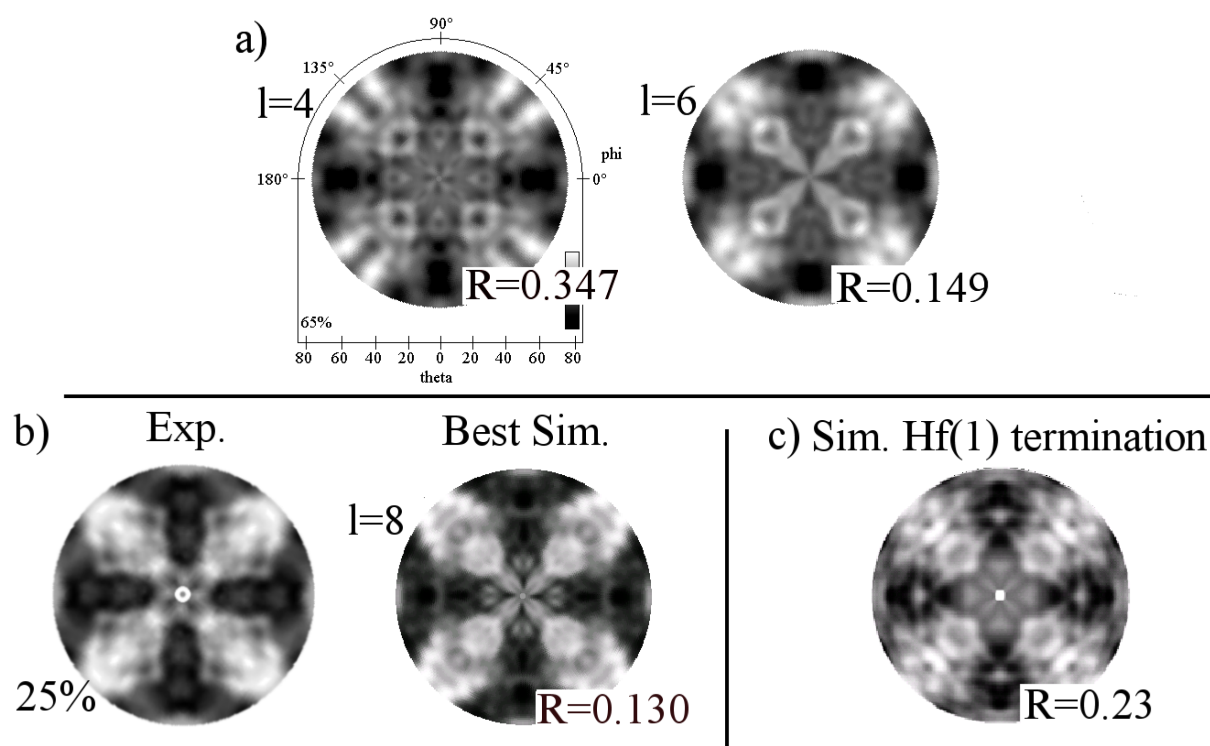

Figure 5.20: Simulated diffraction patterns (a) for different preset ℓ-values. Best simulation obtained (b) compared to the experimental findings. Best simulation obtained using the Hf(1) surface termination (c).

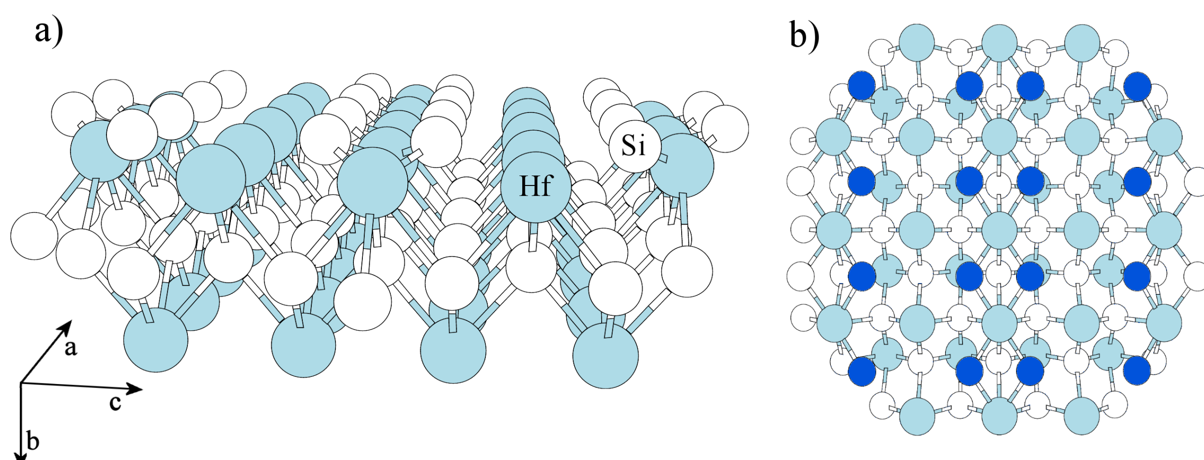

Figure 5.21: Final model cluster used to obtain the simulation displayed in Fig. 5.20. Part (a) shows a side view of the modified C49 structure, while part (b) shows the same cluster from an above perspective. Here, the atoms of the surface reconstruction are colored differently for more clarity.

ℓ-value used in the simulations. Fig. 5.20(a) displays calculated patterns for ℓ-values of four and six exposing R-factors of 0.35 and 0.15. The improvement of the match between experiment and simulations with increasing ℓ can clearly be seen. For a better comparison, the experimental pattern is again shown on the left hand side of Fig. 5.20(b). The best and final simulation obtained by using an ℓ-value of eight is displayed on the right hand side of Fig. 5.20(b). The assigned R-factor could be calculated to R=0.130. Obviously major parts of the fine structure also match the findings of the experimental pattern. In part (c) the final result of the cluster relaxation using the Hf(1) terminated cluster is shown. The R-factor here could only be minimized to R=0.23 and the appearance of the pattern does not resemble some of the major diffraction intensities and the fine structure features, appearing in the experiment. This points to the Si(2) termination to be the preferred one at the surface. Its corresponding model cluster is displayed in Fig. 5.21 by a top view, part (a), and a side view, part (b), respectively. The cluster contains 103 atoms representing a semi-spherical section through the first five layers of the surface and containing two layers of hafnium. The C49 structure, yet modified, is still the underlying basis here. The corner parameters used to obtain this cluster of atoms are given in Tab. 5.2.

Lattice Parameters [Å]

Parameter	Value	Original
1st IL dist.	0.670	0.684 (= -2 %)
2nd IL dist.	2.173	2.095 (= +4 %)
3rd IL dist.	2.053	2.095 (= -2 %)
d_{row}	2.43	-
Cluster diameter	26	-
Cluster depth	13	-

Other Parameters

Parameter	Value
No. of atoms	103
Electrons' kin. energy	159 eV
Order of wave expansion	8
No. of emitters	2
Surface reconstruction	double row

Table 5.2: Interlayer (IL) distances in Angstroms and other corner parameters for the thinner layer model given in Fig. 5.21.

The R-factor of R=0.105 can be considered as rather good for a more complex system as investigated here. All observations made within the simulation procedures gave a consistent picture of the system. The finding regarding the cluster radius indicate that the ordered structure on the surface has a larger span than the maximum cluster size used here (due to hardware

limitations). Usually the parameters sub-spaces probed by a grid search showed an absolute minimum at the same position found by the genetic search algorithm. The results form this investigation were used to set up the first models for the subsequent investigation involving the structure obtained for thicker initial hafnium coverage.

5.5 $HfSi_2$/Si(100) - Thicker Layer

During the measurements it turned out that the XPD patterns obtained from the surfaces changed by the initial amount of hafnium on the surface. While in the previous chapter the structure for Angstrom thick films was determined, in this part of the work the structure modification for nanometer thick Hf-layers is presented. The findings will be published in [107]. As the principal approach is comparable to the one in the previous chapter, some results will be presented more briefly, even though the overall CPU time was longer in this case (around 1800 hours).

5.5.1 XPS Investigation

As seen for the previous investigation, one has to tend to the XPS results to justify the further XPD data treatment. Fig. 5.22(a) displays an overview spectrum obtained after evaporation of hafnium for around one hour and subsequent annealing at 750°C for 10 minutes. All the intensities appearing could be allocated to the known species of Hf and Si on the surface. Thus, impurities can be estimated to be below 1 % of a monolayer. Here, the calculations involving the inelastic damping of the silicon signal by the overlaying hafnium gave evidence that the initial thickness of the evaporated film was $1-1.5$ nm.

Part (b) of Fig. 5.22 displays a high resolved spectral window containing the Si 2p photoelectron signal. The decomposition in its components shows a small PE signal originating from the silicon species bond in the $HfSi_2$ structure on the surface to the side of higher kinetic energies. The components used are comparable to those in Fig. 5.12. Due to the higher initial coverage on the surface the resulting component allocated to the Si_{HfSi} structure does contribute slightly more significant to the spectrum than before. One has to account for the higher excitation energy of $h\nu = 400$ eV used for this spectrum. However, the overlap between this component and the S-component of the Si substrate still inhibited the recording of an unambiguous XPD pattern from the silicon species bond in the $HfSi_2$ structure. The S-component in this case can be considered as not negligible, because the strong decrease in the Hf 4f intensity during the

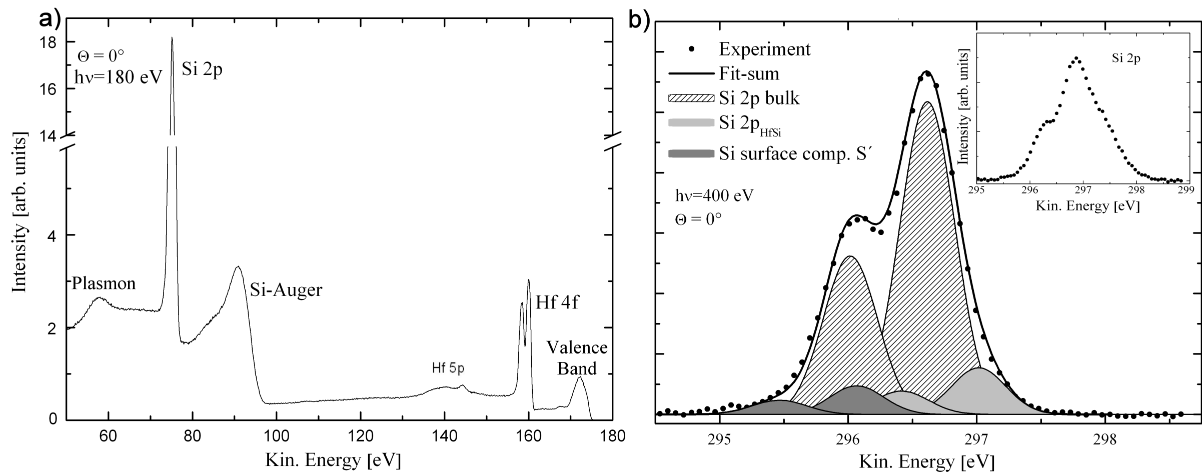

Figure 5.22: Overview spectrum (a) after evaporation and annealing of the sample. No impurities are visible on the surface. High resolution spectrum (b) of the Si 2p signal and its decomposition into sub-components. The same peak before annealing is shown in the inset (see text).

tempering of the sample. This points again to island formation at the surface and the exposure of vast amounts of the underlying silicon substrate. The final proof of this assumption will be given in Ch. 5.6, where real space images of the surfaces will be presented. The inset of Fig. 5.22(b) displays the same energy interval recorded before annealing the sample. It consists of a mixture of several sub-components that could not be unambiguously identified.

A high resolution spectrum obtained from the Hf 4f signal is given in Fig. 5.23. As in the thin-layer investigation, the most reasonable fit was obtained by using a doublet of Doniach-Sunjic

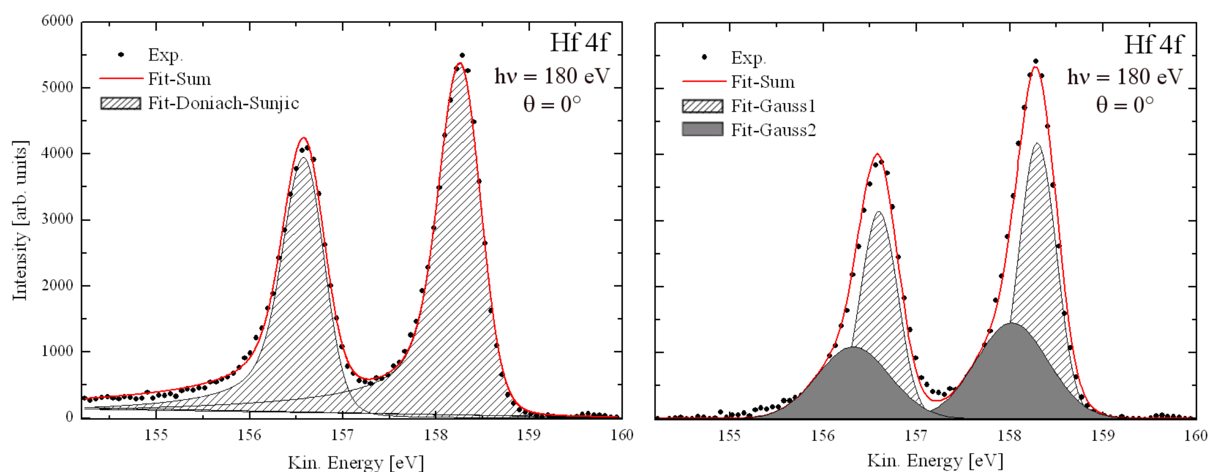

Figure 5.23: High resolution Hf 4f spectrum and the decomposition in its components by using a Doniach-Sunjic doublet (a), and two Gaussian doublets (b).

profiles. The asymmetry used here is α=0.125. The widths of the Gaussian, and Lorentzian distribution, respectively, are w_G=0.47 eV, and w_L=0.06 eV. A decomposition in two Gaussian doublets, as displayed in part (b) of the figure, did not lead to separable diffraction patterns. Also, the accordance between fit and data is worse compared to the case where the Doniach-Sunjic profiles are used. In other words, the spectrum can be expressed by only one chemical component with respect to the resolution of the experimental data. The asymmetric line shape indicates the formation of metallic compounds on the surface. From this signal and the Si 2p intensity XPD patterns were recorded using an angular increment of $2^\circ \times 2^\circ$.

5.5.2 XPD Investigation

Hafnium and silicon patterns are displayed in Fig. 5.24(a). On the left-hand side the diffraction pattern obtained from the Si 2p signal (after evaporation and annealing) is displayed. The pattern exhibits almost no difference compared to the pattern of a clean surface, and is nearly undistinguishable from the pattern shown in Fig. 5.24(a). The R-factor between them is R=0.05. But it strongly differs from the pattern on the right hand side of Fig. 5.24(a) obtained from the Hf 4f signal. This points out once more that the diffraction observed is truly an effect caused by the structural order of the hafnium itself. Besides the raw data, the processed and symmetrized data are also shown. To enhance the diffraction effects a 5th grade polynomial was subtracted from the data and an averaging method regarding the expected four-fold symmetry was applied. The application of this method can be justified by looking at the raw data exposing only four-fold features, beside some random fluctuations. The usage of this methods plus the removal of steps within the polar angles has already been discussed in Ch. 5.4. In addition, the removal of a random spike is illustrated in Fig. 5.24(b): Those effects can be produced by a temporarily change in the grounding of the sample, or electrical disturbances in the detection system. The appearance of this spike in the XPD pattern is indicated by a black arrow. To automatically remove those effects from a pattern, a method operating as a window discriminator was developed. Count rates beyond the preset window aperture (dotted lines), in this case [5000,8000], are removed by substituting them with the average count rate of the adjacent angles. Here, the method was applied to the points $I(\theta = 24^\circ, \phi = 46^\circ)$, and $I(\theta = 24^\circ, \phi = 48^\circ)$, respectively, as well as to some other coordinates within the pattern that are not shown explicitly. After subtracting the non-diffracting background, the data exhibit the shape of the line shown in the lower part of the graph. The four-fold symmetry of the data is clearly evident here, even without symmetrizing the data set. By applying all those methods to the pattern it was possible to enhance the diffraction

effects without adding additional artifacts to it. The pattern shown in the lower part of Fig. 5.24(a) was then used for the following structure determination.

Cluster relaxations by using an R-factor analysis were conducted, as before, by applying a combined genetic algorithm and grid search method. The clusters used typically had a size of around 60-120 atoms and a radius of $9-12$ Å. In the course of the calculations those numbers were increased slightly. The ℓ-values were set to $5-6$ at the beginning and were increased to $\ell = 8$ later on. Those changes in cluster size and ℓ-value also increased the CPU time for one XPD pattern from 10 minutes at the beginning to $30-40$ minutes at the end of the simulation procedure. One example input-file is given in Appendix B. Typical parameters used are summarized in Tab. 5.3. In the course of the simulations the cluster was reshaped from a semi-hemispherical morphology to a trapezoid appearance, thus further reducing the R-factor. This procedure will be discussed below. For the alternate cluster shape the magnitude of the radius r turned obsolete,

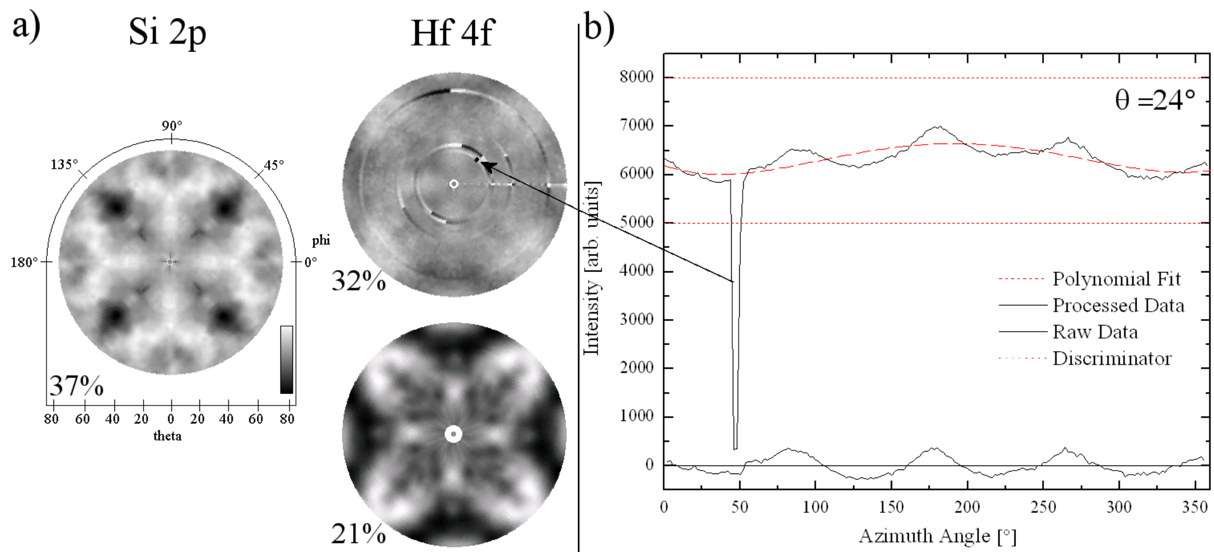

Figure 5.24: Experimental XPD pattern (a) obtained from the Si 2p signal, and from the Hf 4f signal, respectively. The Hf pattern is displayed before and after the data processing procedure. Sample azimuth scan (b) taken out of the Hf pattern displayed in (a) before (upper part) and after (lower part) data processing.

Parameter	Value	Parameter	Value
Kin. energy	159 eV	Reconstructions	none, dimers, (double)-missing row
Inner pot.	-4 eV	Lattice distortion	0-5 %
No. of atoms	60-120	ℓ-values	5-8
No. of layers	3-5	Cluster lengths	10-30 Å
No. of emitters	2-4		

Table 5.3: Typical parameters used in the simulation procedure for the thicker hafnium layer.

and at a certain point in the calculations it became necessary to introduce the length l_c of the clusters together with their width w_c.

The most significant choice is again the surface termination for the model clusters. After the appearance of the diffraction patterns changed by increasing the initial amount of hafnium on the surface, the termination of the structure might also have changed. Simulations for C49 model structures with different possible surface terminations were already shown in Fig. 5.16. The best R-factor was obtained for a model with two layer Si(2) termination, shown in Fig. 5.16(a), explicitly R=0.32. The second best match, compared to the pattern displayed in part (b), was only R=0.53 and regarding (c) only R=0.80. From that result it was decided to use the 2Si(2) (Si(2) double-layer) surface termination for the clusters, while some attempts were also made using the 1Si(2) termination. The relaxation of the latter structure did not lead to satisfying results after it was not possible to generate the diffraction features along the $\phi = 0°$, $\phi = 90°$, etc. direction (cf. Fig. 5.24(a)). Thus, the two layer Si(2) termination was used in the following investigation.

One of the major results of this investigation is the influence of the clusters' geometry on the quality of the simulations. Up to now XPD only has been used to determine interface structures, or surface reconstructions [108, 109]. Here, a three-dimensional island structure was introduced, reflecting also the morphology of the $HfSi_2$ islands on the surface. Using the geometry of the

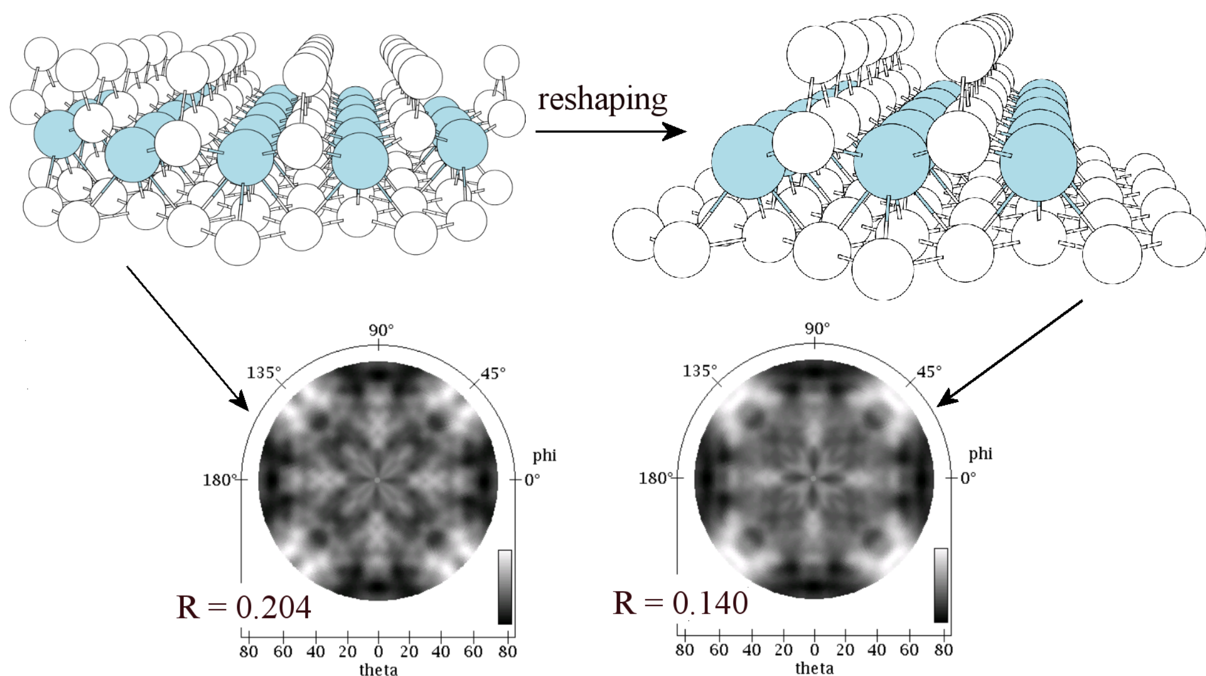

Figure 5.25: Influence of the model cluster shape on the quality of the resulting diffraction patterns.

cluster as a free parameter in the simulations led to a trapezoid-like structure with an elongated rectangular base, as in Fig. 5.25. The cluster shape's influence was discovered coincidentally while testing for the influence of the atoms at the edge of the initially hemispherical cluster. The results are illustrated in Fig. 5.25. The XPD pattern for the same basic structure is shown twice: once for a hemispherical cluster geometry, and then after reshaping the cluster into an elongated island. By this operation the R-factor dropped from R=0.20 to R=0.14 for a cluster that already had been relaxed with a CPU time of around 1000 hours. A drop of $\frac{\Delta R}{R=30}$ % can be considered as drastic. At these low R-values, it hints to a true situation on the surface. Unfortunately most of the relaxations so far turned obsolete by this new finding, and had to be repeated. This new insight was again applied to 1Si(2) terminated structures to check for possible advances here, without reasonable results.

In the following a few examples for relaxing some crucial cluster parameters will be given. They all relate to the trapezoid island structure. At the end the final model cluster and its associated XPD pattern will be presented.

One important magnitude of the islands was their length. AFM pictures presented later show the islands spanning several tens of nanometers, well above the sensitivity horizon of XPS. The expectation here would be that the R-factor should not increase with an increasing length of a model cluster representing a section of such an island. The behavior of the quantity in the present case is displayed in Fig. 5.26. For lengths below 8 Å the width w_c was also influenced by the investigation, because the main parameter that could be controlled in the MSPHD program was still the radius r around an emitter that contributed to the patterns. For a length below 1 nm obviously some atoms mainly contributing to the patterns are missing and the match between

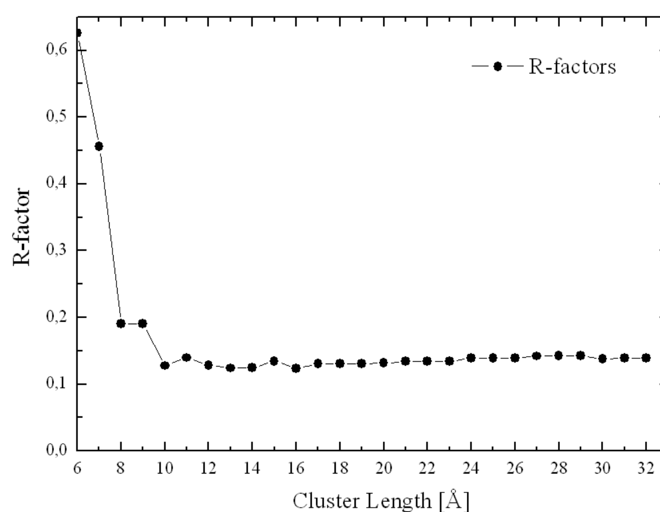

Figure 5.26: R-factor plot for varying the length of the elongated island structure.

experiment and simulation gets worse. The lowest R-factors were obtained for a cluster length of around 15-20 Å. With increasing cluster length, the R-factors increase slightly, but the loss of accordance of only ΔR=0.02 cannot be considered significant. One reason, if any, could be the fault density within the surface structure, causing the experimental patterns to differ slightly from the perfect surface that has been assumed in the calculations even for bigger clusters.

For all the chosen length, the double-row feature at the surface, consisting of silicon atoms, strongly contributed to the appearance of the calculated XPD patterns. To find the optimal positions of these atoms as well as the distance between them, their lateral coordinates were used as variables in many of the parameter sets minimized by the GA. At some point in the investigation a grid search was applied to the x and y surface coordinates. The results are given in Fig. 5.27. Part (a) illustrates a top-view of the structures indicating two atoms of the silicon double-row, and four Si atoms of the second layer (dotted circles). The dashed rectangle frames the x-y-space probed by the grid search displayed in part (b) of the figure. The “zero” in marks the atoms’ position of the non-relaxed layer. In contrary to the structure found for the thinner layer, the R-factors found point to a position close to the initial one. Also the longitudinal positions stayed unchanged. As a third parameter (not shown), the first interlayer distance between the double-row feature and the next Si-layer underneath was taken into account. A value of 1.93 Å was found. This corresponds to a 12 % expanded distance. An attempt to form asymmetric dimers to terminate the structure led to no progress in the match between the patterns. Another try to

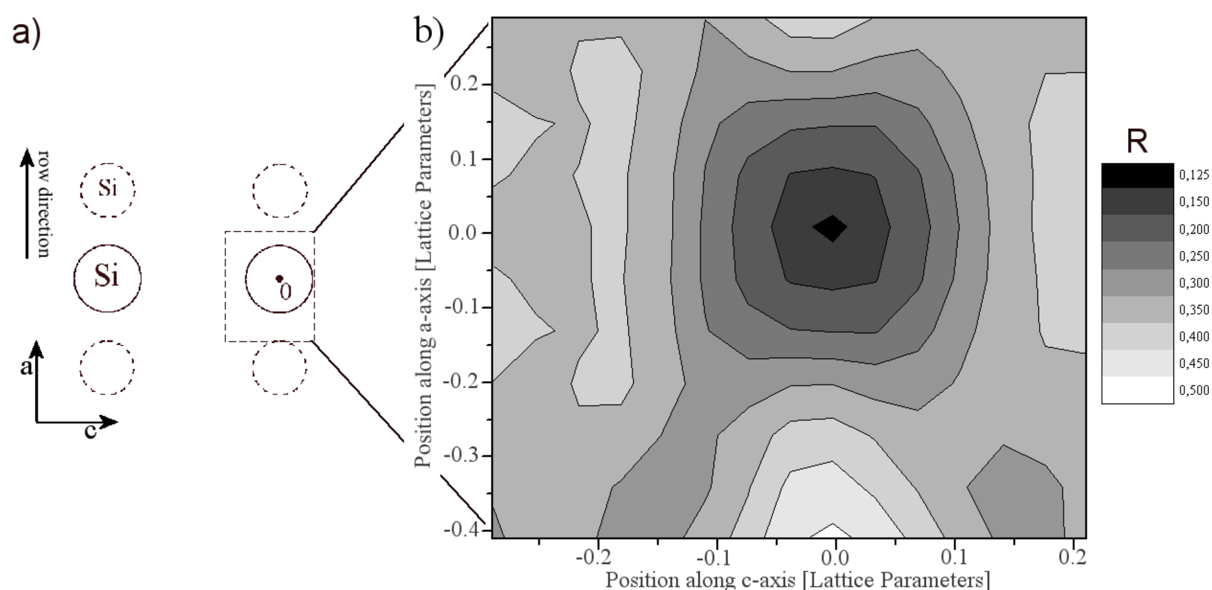

Figure 5.27: Illustration of the double row feature at the top of the clusters (a). The parameter space spanned by the lateral lattice vectors that was probed in (b) is indicated by a dashed rectangle in (a).

substitute the double-row by a single atomic row led to R-factors 30 % worse compared to those obtained from the structure described above.

The XPD pattern exhibiting the lowest R-factor is displayed in Fig. 5.28(a). For an easier comparison the initial experimental results are repeated here. The reliability factor between them is R=0.11. It can easily be seen that almost all experimental diffraction features could be resembled by the calculations. The forward scattering peaks are all present in the calculations. But also the diffuse appearing scattering-intensities could mostly be generated for many polar angles. For the higher values of θ, in particular, the R-factor was below 0.05 in some cases.

The right-hand side of Fig. 5.28 displays the final model cluster used to calculate the pattern shown in part (a). It consists of 115 atoms, has a length of 32 nm, and a width at its base of 1.5 nm. The position of such a cluster inside the presumed island structure is displayed below. The structural parameters used here are summarized in Tab. 5.4.

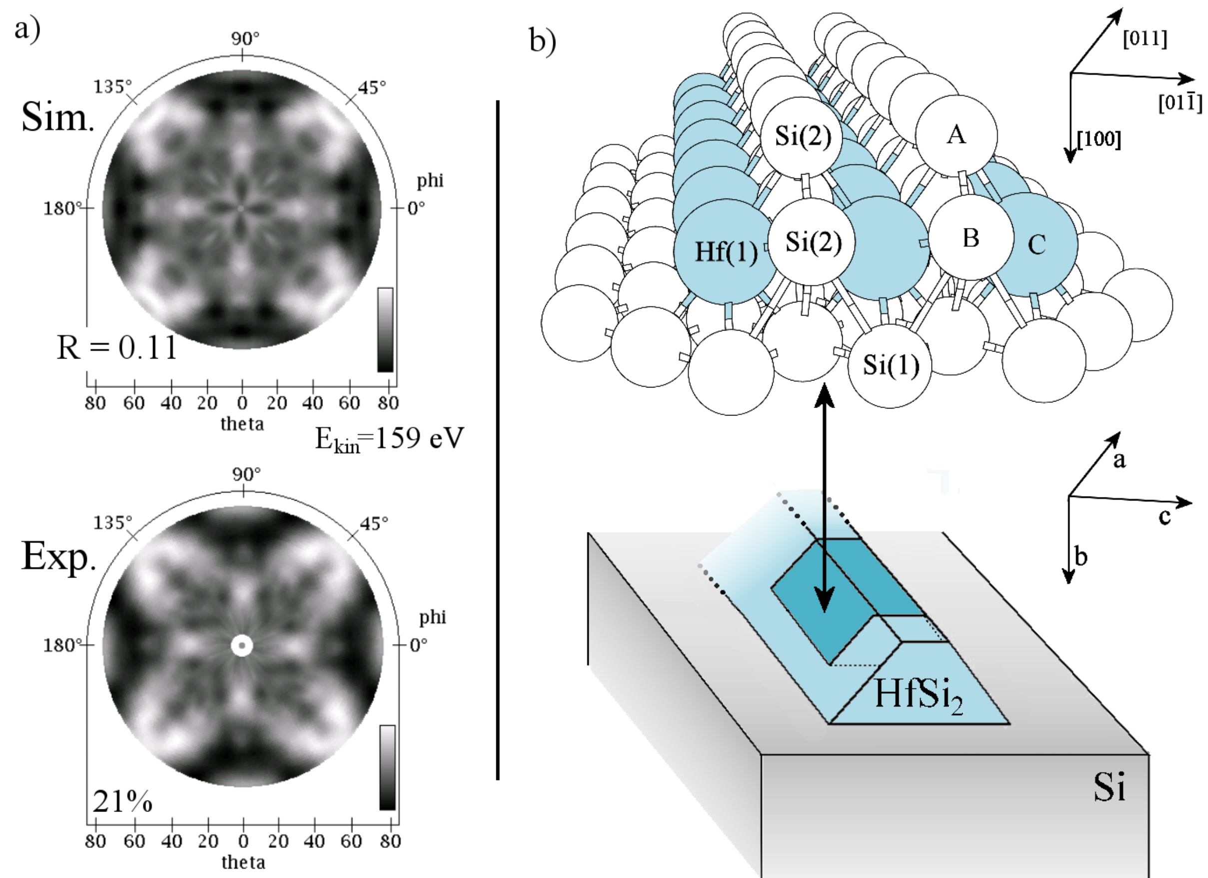

Figure 5.28: Final simulation (a) (upper part) exposing a low R-factor compared to the experimental results (lower part) of R=0.11. The model cluster used to obtain this calculation is displayed in (b) (upper part). The lower part of (b) illustrates the position of the model cluster within the island structure on the surface [107].

Parameter	Value	Uncertainty
1st IL dist.	1.72 Å	± 0.04 Å
2nd IL dist.	0.68 Å	± 0.04 Å
3rd IL dist.	0	± 0.08 Å
1st layer row dist.	3.6 Å	± 0.3 Å
Top-layer displacement	0 Å	± 0.3 Å
Cluster radius	>30 Å	-

Table 5.4: Interlayer (IL) distances, top-layer displacement, and cluster radius and their respective uncertainties.

To summarize the low-energy investigations, it can be stated that both the final patterns for the thin and thick layers, respectively, are in very good accordance with the experimental results. For different initial surface covers the resulting XPD patterns could be simulated using the same basic structure. For a higher amount of hafnium on the surface the formation of three-dimensional islands was indicated by the simulations. Their length extends to at least 30 Å. The simulation of longer clusters was not possible due to computational limitations.

5.5.3 Lattice Alignment

One question not answered yet is the alignment of the main crystal axes of the $HfSi_2$ structure with the silicon substrate. The connection between the lattice orientations can also be derived from the XPD results: The experimental patterns of the hafnium signal in Fig. 5.29(a) were always accompanied by a silicon pattern, recorded at the same time. Thus the patterns have a fixed orientation with respect to silicon pattern shown. By simulations for the silicon bulk and the $HfSi_2$ structure it is possible to determine the alignment of the crystal axes of the hafnium silicide islands and the substrate with respect to each other. Therefore, the model structure of silicon was aligned in such a way that the alignment of the resulting (calculated) patterns reproduces the alignment of the experimental ones. As a result, the model structures have to be rotated around the surface normal by 45° with respect to each other, so that the lattice vectors in the surface plane are aligned parallel to the [011] and $[0\bar{1}1]$ axes of each other, respectively. This is also supported by AFM and STM studies [6, 7, 73]. However, a direct determination by AFM/STM is difficult, since only the surface layer with a possible surface reconstruction is probed by these techniques. This finding is furthermore supported by the high energy results presented in Chs. 5.2.1 and 5.3. Here, the alignment of the lattices can be performed in a comparable fashion.

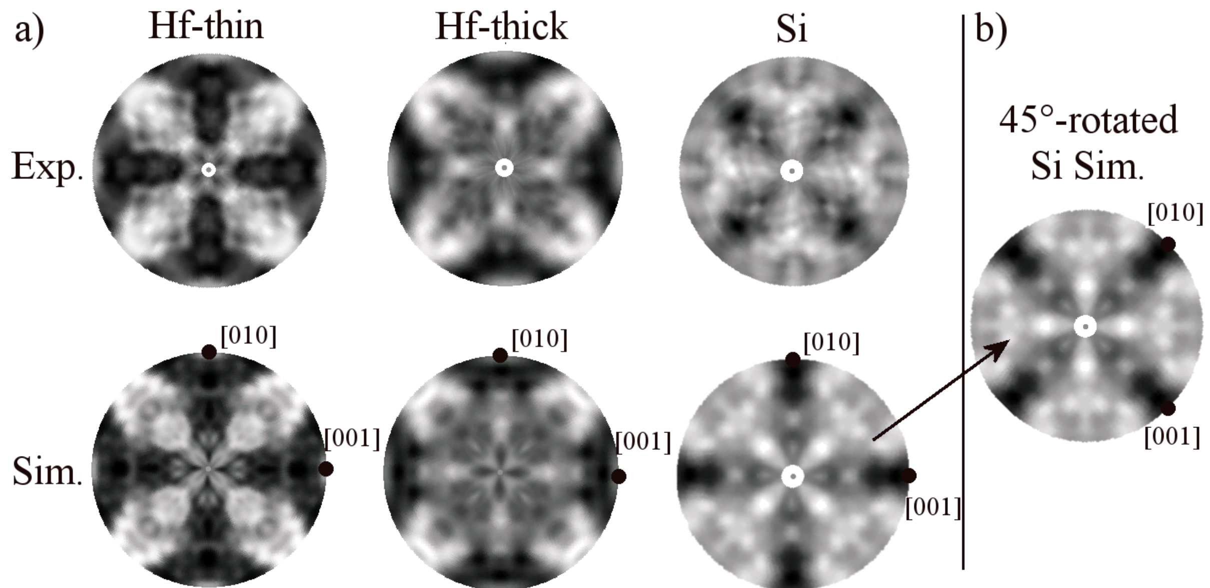

Figure 5.29: Determination of the lattice alignment between the island and the silicon substrate, by comparing the simulated patterns (see text).

5.6 Real Space Imaging of Annealed Hf Films on Si(100)

To unambiguously identify the surface morphology of the investigated structures complementary real space investigations were performed. For a more general overview over the surface, scanning electron microscope (SEM) pictures were recorded at the ISAS [110] in Dortmund. Two hafnium coated samples were prepared. One (sample A) was annealed at 600°C for 10 minutes, after evaporating a nanometer thick coverage. The other sample (sample B) was annealed at 800°C after evaporating a comparable amount of hafnium. Both samples were investigated by XPS, using Mg K_{α}-radiation, to verify the presence of hafnium on the surface. The SEM pictures were recorded by measuring secondary electrons generated by an incident electron beam. Their number in this detection mode is evaluated by a solid state scintillation detection device and a consecutive secondary electron multiplier. This kind of arrangement is called an Everhart-Thornley detector. Details concerning SEM detectors and detection modes can be found in various text books, e. g. [111]. The amount of electrons emitted from a site on the surface is, of course, a function of the incident beam's energy and the chemical composition, i. e. the elements present. In addition shadows can be applied by either detecting the electrons under a certain angle with respect to the surface normal, or tilting the electron source.

The results of the investigation are shown in Fig. 5.30. Part (a) displays a $\approx 2 \times 2.5\,\mu\text{m}^2$ fraction of sample A. Elongated structures of rectangular basis can be observed throughout the image. Their length ranges from $100-500$ nm, their width can be estimated to be <50 nm,

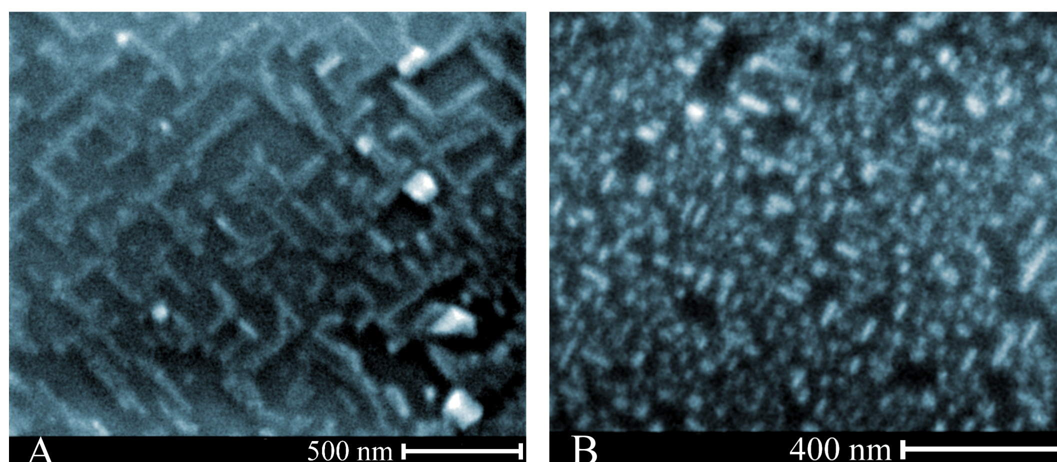

Figure 5.30: Scanning electron microscopy images obtained from Hf/Si(100) systems after annealing at 600°C (a) and 800°C (b).

leading to an aspect ratio of $5 - 20$. As expected from the simulations they are arranged in two perpendicular domains, presumably following the rows of the (2×1)-reconstruction. The orientation of the underlying silicon substrate could not be determined in this measurement. Unexpectedly, the length and width of the islands is much larger than estimated by the simulations. One reason could be that the simulations were conducted after an annealing cycle at 750°C. The XPS intensity ratio between the Si 2p and the Hf 4f signal for sample A was comparable to the ration before annealing, around 1:1. For the high energy investigation it turned out that after annealing at 600°C almost no diffraction could be observed [75].

Indeed it turns out that the surface morphology changes for sample B, annealed at higher temperatures, when structured XPD patterns could also be obtained. The island sites in Fig. 5.30(b), a $1.2 \times 1\,\mu$m image, expose an approximate length of 10-80 nm, a width of far below 20 nm, except for a few of the visible islands. The aspect ratio is around 3-10. The resolving power of this method strongly limits the measurement of the smaller structures appearing. However, the alignment in two preferred surface orientations can again be observed. The change in the morphology compared to sample A goes along with a drastic (and expected) reduction of the XPS yield of the hafnium signal. Here the intensity ratio dropped to around 1:4.

For further investigation of the small structures appearing at higher annealing temperatures, atomic force microscopy was used to record scans from the sample surfaces. Fig. 5.31 displays a $250\times250\,\text{nm}^2$ image of a system annealed at 700°C [107]. Contrary to the REM experiments, the samples were not taken out of the vacuum before the measurements. By using an EBE attached to the STM/AFM chamber [112] the samples were prepared and measured in-situ [113].

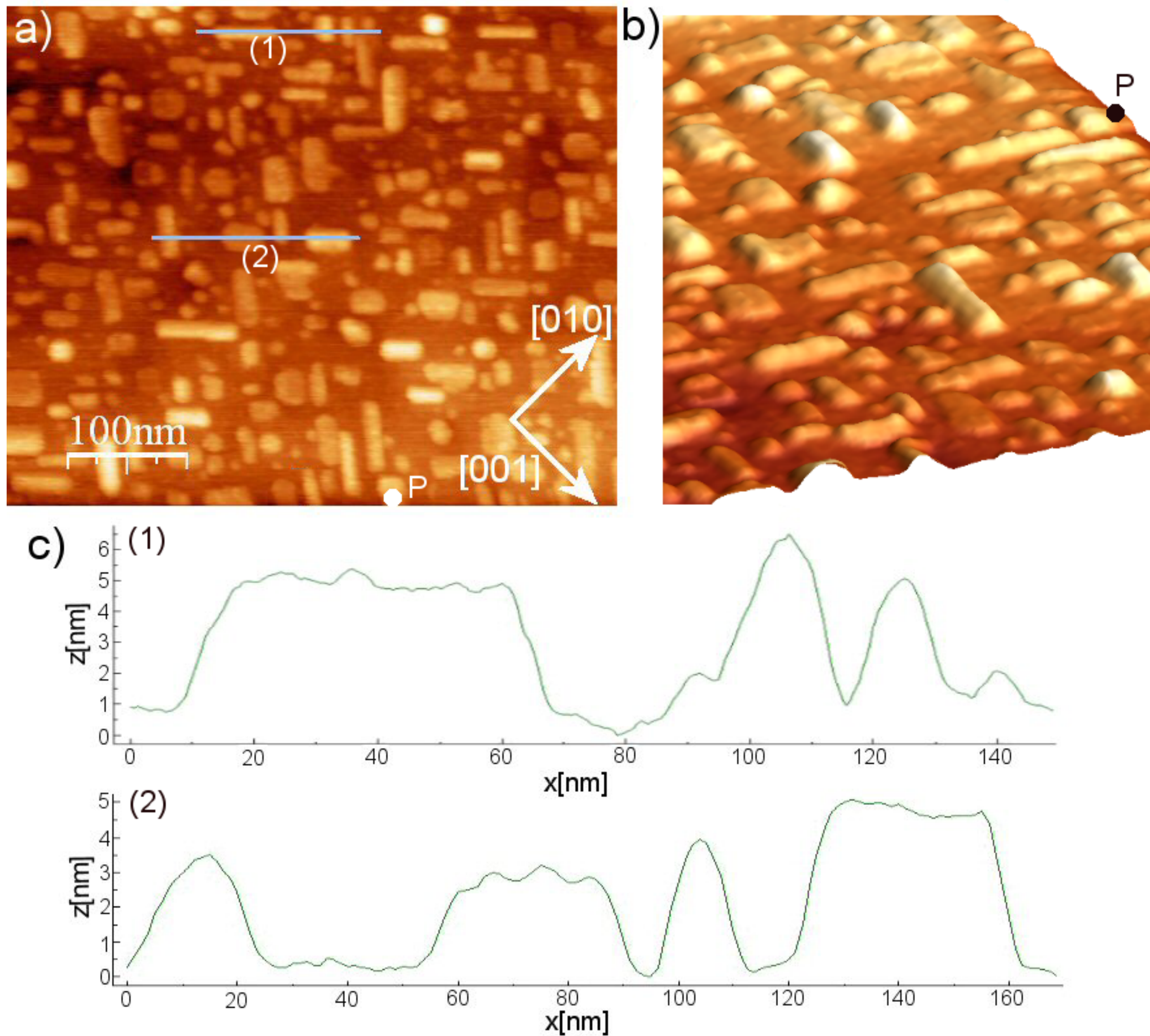

Figure 5.31: $400\times500\,nm^2$ AFM image of a two domain structure of hafnium silicide islands on a Si(100) (a), the substrate orientations are indicated by arrows. Perspective view onto the same surface (b). Line scans from the surface (c), as indicated in (a).

The base pressure of the chamber is 1.0×10^{-10} mbar. By using a LEED system attached to the chamber it was possible to measure the orientation of the silicon substrate. The main surface directions are included in Fig. 5.31. Consistent with the previous investigations, one observes an alignment of the structures along the silicon [011] and $[0\bar{1}1]$ direction, thus collinear to the initial (2×1) surface reconstruction. The islands themselves show the same morphology as observed in the SEM measurements. The aspect ratio equals that observed for sample B from the above described measurement of around $4-10$ nm.

To sum up, it can be stated that the structure observed in the real space investigation equals the structure found in the calculations for the thicker layer concerning its morphology. The observed

structures appear to be longer, as well as broader, compared to the simulated ones. This can be understood by the limited electrons' mean free path in XPS/XPD, limiting the correlation length between emitted and scattered waves within the surface to a few nanometers. Therefore, as illustrated in Fig. 5.28, the model cluster shown relates only to a part, but a representational one, of the islands. The results are comparable to high resolution STM investigations, showing that the system as prepared in this work is comparable to nanowires obtained by other groups [114]. This gives evidence that the structural determinations in Ch. 5.5 are universally valid for this system.

5.7 Stability of EBE Prepared HfO_2/Si(100)

As described in Ch. 3, ultra-thin hafnium dioxide layers are candidates for forming advanced gate dielectric for field effect transistors, along with other transition-metal oxides and rare-earth oxides. They ought to replace SiO_2 as a gate dielectric, due to favorable electronic properties, having in particular a significant higher dielectric constant κ compared to silicon [1, 2]. Presently, their use is thought to be one of the solutions proposed to keep up the miniaturization process in the semiconductor industry, although, their thermal stability is questionable [7, 73, 115]. Tempering the layer-stack at temperatures up to 1000°C is an inevitable part of the active production process of metal-oxide field effect transistors (MOSFETs) and cannot, so far, be omitted. This process leads to partial or full silicidation of hafnium, destroying the system's insulating properties. Ultra-thin layers of HfO_2 and other, so-called, high-κ dielectrics are usually applied to the surface by atomic layer deposition (ALD), or chemical vapor deposition (VCD). This has been shown in a variety of publications in different fields of the surface science community [3, 116–119]. Further on, most of the characterizations are performed by AFM and STM.

Thus, the next step in this work is to prepare the HfO_2/Si(100) system by our preparation methods, i. e. by evaporating Angstrom-thin layers of HfO_2 directly onto the substrate via electron beam evaporation (EBE). Literature involving EBE usually refers to an evaporation of metallic hafnium onto the silicon surface followed by annealing in oxygen ambient [7]. Subsequently, we followed in detail the development of the system after tempering by using photoelectron spectroscopy (XPS) in the soft x-ray regime. Further, a first photoelectron diffraction study was performed. The results will be published in [120].

The experiments were carried out in-situ within the UHV presented in Ch. 4. Si(100) samples, as used before, were cut of an industrial wafer and cleaned in iso-propanol. The native oxide layer was removed by flash annealing to 1000°C inside the vacuum chamber. Afterwards, the

(2×1) surface reconstruction was formed by gradual cooling. The reconstruction was finally checked by low energy electron diffraction (LEED) and XPD patterns that were recorded and referenced to diffraction results obtained in previous silicon investigations. Hafnium oxide was evaporated onto the samples using an electron beam evaporator (cf. Ch. 4) equipped with a special holding mechanism to carry grains of HfO_2. The samples were subsequently annealed at different temperatures for 10 minutes. To omit broadening or shifts of the photoemission signals, a cooling period of half an hour was allowed after each the annealing cycles.

XPS investigations were performed using the undulator beamline 11 at DELTA. To enhance the surface sensitivity of the experiments, photons having an energy of $h\nu$=200 eV were used for excitation. Photoelectron diffraction patterns were recorded using the same excitation energy. Around 7000 spectra were recorded within the XPD investigation. The HfO_2 layer thicknesses were calculated by the damping of the silicon bulk signal due to the HfO_2 overlayer. Assuming a closed layer directly after the evaporation, the XPD data were used in terms of an angle-resolved photoemission spectroscopy study (ARPES) to determine the layer thicknesses. The layer thicknesses ranged from 8 Å to 20 Å.

The most intense photoemission lines at this energy, i. e. the silicon 2p signal and the hafnium 4f signal, were chosen for the investigation. Fig. 5.32 displays the spectra obtained for the relevant elements hafnium and silicon directly after the evaporation. The experimental results are indicated by dotted curves. The Hf 4f signal was found to have a binding energy of around E_{Bin}=(17.7 ± 0.1) eV for the oxidized species. The Si 2p signal's binding energy was E_{Bin}=(99.2 ± 0.05) eV, for the silicon bulk signal. The uncertainty margins correspond to the experimental energy increment. All XPS spectra were normalized by the incident intensity. The background of secondary electrons was removed by subtracting the Shirley-background [91]. Levenberg-Marquardt and Simplex methods,as described in Ch. 2.2, were used as fitting routines.

In the displayed spectra one observes the absence of silicon oxide and $HfSi_2$. This result was initially suspected in one of the earlier investigations [100] and is now evident in the decomposition of the spectra. Silicon dioxide usually equals a 4^+ oxidation of silicon. Its expected energy position [121] is marked in Fig. 5.32(a). Its chemical shift is expected to be 3.6-4.2 eV depending on the layer thickness and also on the preparation method used. The layer thickness influences the shift by changes in the band-offset and screening by the silicon substrate for ultra-thin layers. The preparation method influences density, possible crystallization, and incorporated impurities, all having impact on the relative binding energy with respect to the silicon bulk signal.

Additional components appearing in the Si 2p spectrum besides the Si^0 component are

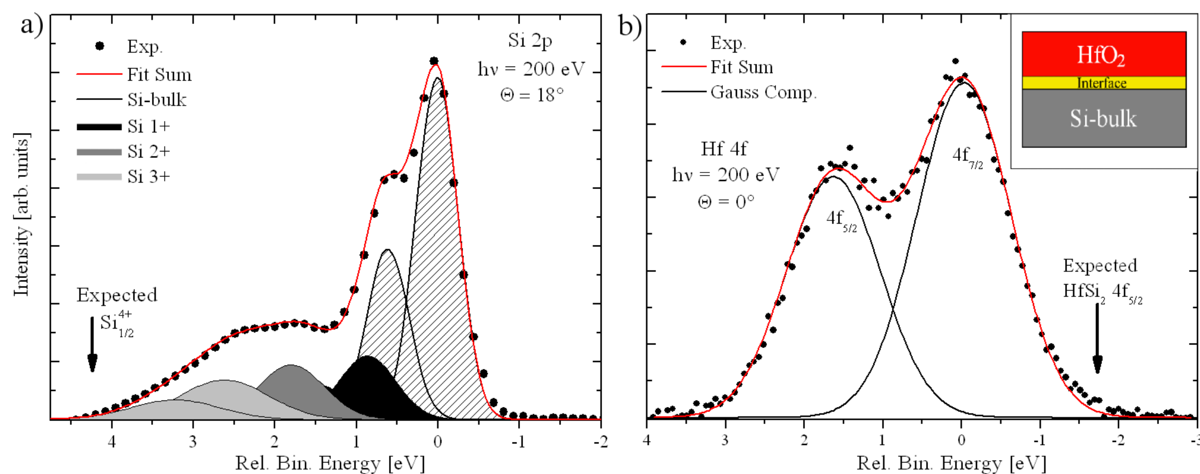

Figure 5.32: XPS spectra of the investigated photoelectron signals. Silicon 2p spectrum (a) and Hf 4f spectrum (b). The experimental data (black dots) can be approximated by a set of Gaussian profiles (see text). The inset of (b) illustrates the system's stack directly after the evaporation of HfO_2

expected to be caused by bonds with either oxygen or hafnium at the interface. This interface between the silicon substrate and the HfO_2 overlayer is illustrated in the inset of Fig. 5.32(b). The position where the $HfSi_2$ photoelectron intensity is expected to appear is marked in Fig. (b), i.e the position for the $4f_{5/2}$-signal is denoted. Relying to preceding investigations the energy position of hafnium silicide is about $14.1 - 14.3$ eV [73, 75], thus it is expected to appear shifted by ΔE=3.3-3.6 eV with respect to the main line. Here, no sub-oxide components are visible between the indicated silicide position and the HfO_2 main peak. A small intensity contribution appears at a relative binding energy of E_{Bin}=-1.5 eV. We allocate it to an increased number of dangling bonds. They could be repeatedly removed by annealing and vanished already at temperatures of 170°C. The Hf 4f intensity appears to be broadened compared to spectra obtained from the 4f signal within $HfSi_2$ layers, indicating the presence of several slightly different HfO_2 modifications, denoting an amorphous layer. Its quasi-continuum of states cannot be resolved by the experiment. The signal's decomposition into a single Gaussian doublet shows the absence of Hf sub-oxides as well as $HfSi_2$. The doublet's intensity ratio was pre-set to 3:4, its energy separation to ΔE=1.7 eV. Good results were obtained for a peak width of $w_{Hf} = 0.60$ eV. Form this finding we infer that HfO_2 bonds to the surface are intermediated by oxygen, leading to sub-oxide features in the silicon spectrum. Hafnium being the second next neighbor to silicon is also reported in the literature [122, 123]. For proving this presumption the Si 2p spectrum was decomposed into different chemical components using a parameter set reported for the interface of the system SiO_2/Si(100) [121, 124, 125] using Gaussian line-shapes. The results are displayed beneath the experimental findings in Fig. 5.32(a). Attention should be drawn to

the number of free variables used. It should be as low as possible to allow unique conclusions regarding the interface chemistry. First, the eight peaks shown are not independent of each other, but forming four doublets, as indicated by same colors. Their shift with respect to each other and the $Si_{5/2}/Si_{3/2}$ intensity ratio were set to ΔE=0.6 eV and 2:1, respectively. This leaves the fit with still 12 free parameters: width, height, and position for each of the doublets. To prove the sole presence or absence of silicon oxide at the interface a further reduction of the free parameters is mandatory. Parameters found for the SiO_2/Si [124] interface were used for this purpose, as mentioned above. This procedure pre-set the energy positions and relative width of all sub-oxide components with respect to the Si^0 component. Further on, the width and the position of the Si-bulk component itself can merely be varied due to the sharp $Si^0_{3/2}$ feature. By applying these constraints one ends up with only four parameters representing the heights of the four doublets used. The experimental findings can be resembled nicely by the presumed components, strongly suggesting an oxygen mediated interface. The values used in the different fitting procedures for silicon are summarized in Tab. 5.5.

Parameter	ΔE to Si-bulk [eV]	Width [eV]
Si^0	0	0.20
Si^β	0.35	$1.45 \cdot w(Si^0)$
Si^{1+}	0.95	$1.24 \cdot w(Si^0)$
Si^{2+}	1.78	$1.58 \cdot w(Si^0)$
Si^{3+}	2.6	$2.0 \cdot w(Si^0)$
Si^{4+}	3.65	$2.2 \cdot w(Si^0)$

Table 5.5: Parameters used for decomposing the Si 2p signal.

A first series of annealing cycles at up to 500°C was conducted to follow possible changes of the surface chemistry in the lower temperature regime. The results are summarized in Fig. 5.33(a)/(b). In Fig. 5.33(a) the hafnium photoelectron signals are displayed. the curve at the bottom repeats the result already discussed for Fig. 5.32(b). For the Hf 4f photoelectron signal only small changes occur. Its position shifts by an amount of ∼0.1 eV. It can be allocated to a reduction of HfO_2 configurations within the layer and the formation of Hf-O-Si bonds. By decomposing the peak, a slight increase of the width becomes apparent after annealing at 500°C. Compared to literature, shifts were observed before, but usually for higher temperatures [7]. The contribution of the sub-oxides in the silicon 2p signal is altered by every step of the series. To illustrate these changes black dots have been placed at the apparent maxima of the sub-oxide features in the different spectra. A closer look at the chemistry after annealing at 500°C will be given below. In Fig. 5.33(c)/(d) a consecutive series of spectra is shown where samples were annealed at temperatures varying from 500-750°C. Neither the Si 2p, nor the Hf 4f signal exhibits noticeable changes in their peak compositions up to temperatures of 700°C. Decomposing the

peaks for the different annealing cycles supports this observation (not shown). Oxygen is completely removed from the surface at a temperature of 750°C. The hafnium signal in Fig. 5.33(c) indicates the formation of $HfSi_2$, as the chemical shift with respect to the previous spectra could be determined to be 3.2 eV. A reduction of the peak area by around 50 % hints to the formation of surface islands that has been observed before [7, 73]. Further, the silicon 2p signal denotes no sub-oxide components and also overview spectra obtained from the surface proved the absence of oxygen.

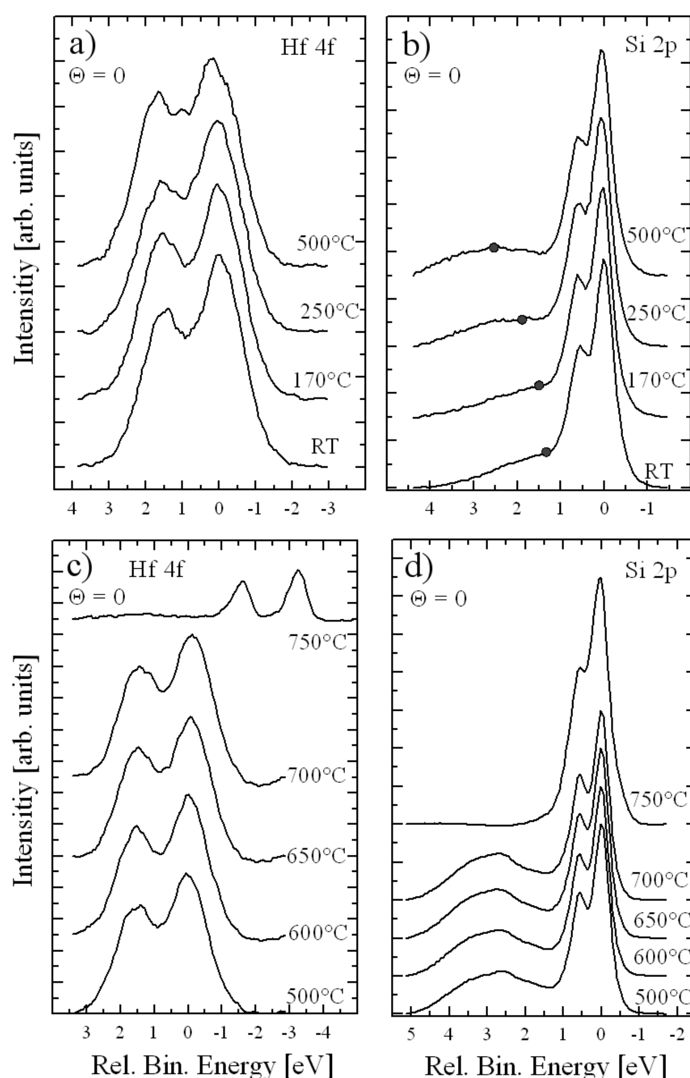

Figure 5.33: Changes of the Si 2p and Hf 4f spectra upon annealing. Annealing series (a) and (b) range from room temperature (RT) to 500°C. Annealing series (c) and (d) range from 500°C to 750°C. Incident light's energy is hν=200 eV for all spectra.

A closer look at the silicon 2p signal after annealing the samples at 500°C is presented in Fig. 5.34. In (a) the same set of silicon oxide parameters as used for Fig. 5.32(a) was applied. At the left end side of the spectrum a new component had to be included. Its position indicates Si^{4+}, i. e. being generated by fully oxidized silicon. Its position and its width were pre-set as before to ensure the component corresponds to SiO_2. While the use of this component allows the sub-oxides-sum to smoothly follow the experimental data, the best fit appears poor in the vicinity of the Si^0 and Si^{1+} component. This makes the use of an additional component necessary that again can be drawn from the SiO_2 model. A sample decomposition for the system $SiO_2/Si(100)$ from a previous work [124, 125] is displayed in the inset of Fig. 5.34(a). For the present investigation the so-called β-component had to be included in the fitting procedure. This component as well as another component called α is presumed to be allocated to silicon atoms within the oxide film not having bonds to oxygen. The match between the decomposition and the experimental data increases drastically in Fig. 5.34(b) by its use. The components' width and its position was pre-set, only its height was varied. The necessity of this component denotes the mobility of silicon at temperature of 500°C, while this kind of diffusion does not take place at room temperature, cf. Fig. 5.32(a). All parameters used in the XPS investigation are summarized in Tab. 5.5. The use of the so-called α-component is not mandatory, in so far as it does not influence the sub-oxide features.

Subsequently to the annealing at 500°C, XPD patterns were recorded from the Si and Hf signals. In a comparable investigation it was possible to obtain distinct patterns from all the

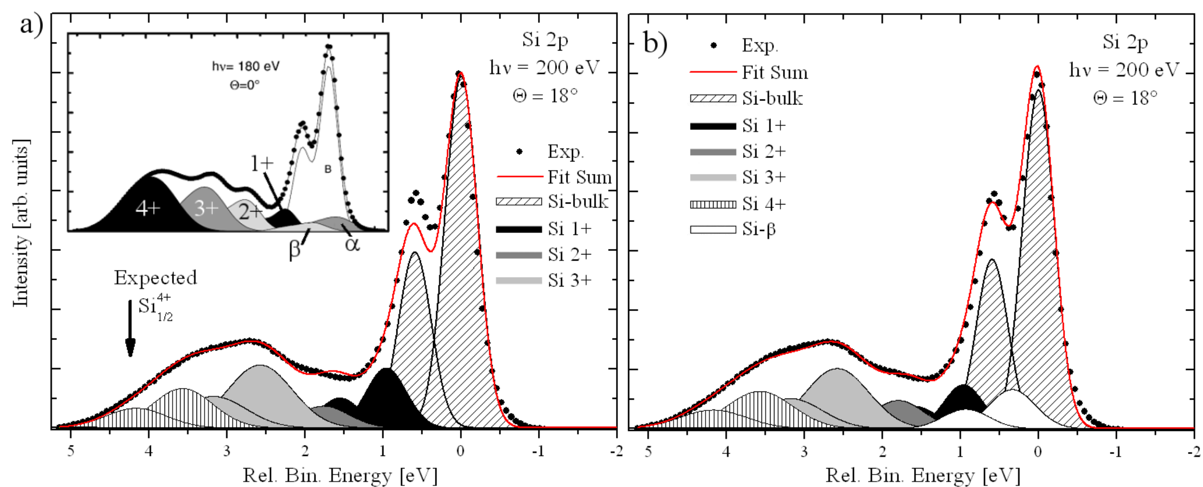

Figure 5.34: High resolution spectra obtained from the Si 2p signal after annealing at 500°C. Without in (a) the so-called β-component indicating silicon diffusion at the interface is left out, it is regarded for in (b). The inset of (a) displays a decomposition found for $SiO_2/Si(100)$ interface [124].

silicon sub-oxides at a SiO_2/Si interface [50]. Some of the results are displayed in Fig. 5.35, along with an illustration of the layer-stack after the formation of the SiO_2 interface. It was possible to record a clear pattern from the Si-bulk component of the system, Fig. 5.35(a). A comparable pattern can be obtained for a clean silicon surface. Anyhow, none of the other components, neither in silicon nor in hafnium, showed a pattern with modulations above the detection limit of about 3 %. This limit is introduced by the statistics of the experimental data and fluctuations of the synchrotron sources' incident beam. An example for such a "missing" pattern is displayed by the Si^{1+} XPD pattern (cf. Fig. 5.35(b)), the one exhibiting presumable the clearest pattern besides the silicon bulk component. No unambiguous modulation can be observed. Along with the lack of any short-range order for the other components, this leads to the conclusion that the interface is much less ordered compared to a purposely prepared SiO_2 layer on Si(100). For these layers the maximum anisotropy of modulations within XPD patterns was measured to be above 20 %, at least for the lower oxidized states, i. e. for the Si^{1+} and Si^{2+} components.

Summarizing it can be stated that the preparation of the system HfO_2/Si(100) by direct evaporation of HfO_2 from an electron beam evaporator on a clean (2×1)-reconstructed Si(100) surface is possible. The evolution of the system upon annealing was followed by x-ray photoelectron spectroscopy and x-ray photoelectron diffraction. It was shown that at the initially SiO_2-free as well as $HfSi_2$-free interface a silicon oxide layer forms upon annealing, starting at already 250°C. The presence of SiO_2 was confirmed by decomposing XPS spectra into its chemical shifted components. Hence, a detailed decomposition of the signals before and after annealing was possible. The XPS spectra indicated additional silicon diffusion into the interfacial layer. Photoelectron diffraction patterns recorded from the Si 2p and Hf 4f signals denote a lack of ordered structures at the interface compared to purposely grown SiO_2 layers on a silicon substrate.

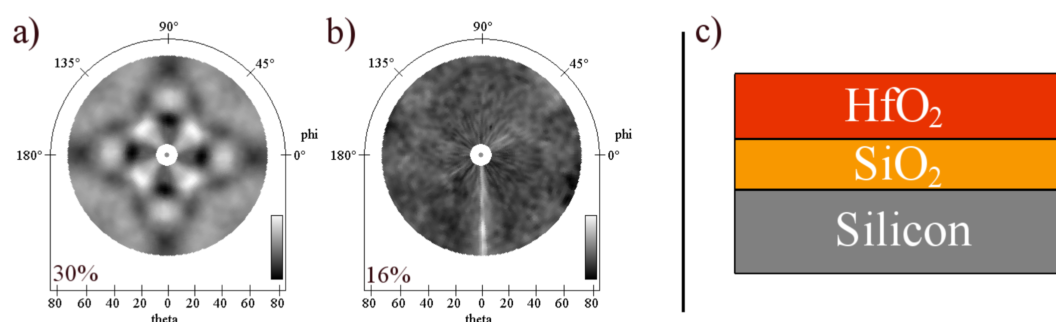

Figure 5.35: Photoelectron diffraction patterns (a)/(b) recorded from the Si 2p photoelectron signal, denoting ordered and unordered silicon species recorded for the silicon-bulk and Si^{1+}-component, respectively. Illustration of the system's layer-stack (c) after annealing at 500°C.

By annealing at temperatures above 700°C the stack is decomposed into $HfSi_2$ islands, while oxygen fully desorbs from the surface.

5.8 Stability of the System $HfO_2/Si_3N_4/Si(100)$

The previous investigations showed that HfO_2 layers prepared by EBE (and other methods) are not stable on the silicon surface upon annealing. Their lack of thermal stability can be understood by diffusion. At temperatures above 250°C additional interstitial oxygen, present in the HfO_2 layer, diffuses through it and initiates the growth of a silicon oxide layer, as shown in the previous chapter. At temperatures above 700°C mobilized silicon atoms diffuse into the HfO_2 slab, leading to the formation of metallic $HfSi_2$. This fully destroys the layer-stack's insulating properties. One idea to prevent diffusion within the layer-stack is to introduce a diffusion barrier at the interface. The implantation of nitrogen in some form can act as such a barrier. Various forms of nitrogen implementation have been reported [126, 127]. Those reports usually rely on N_2 or NH_3 annealing of a HfO_2 on Si, in this study an initial Si_3N_4 buffer layer between silicon and the oxide was prepared. Hence, as a first step ultrathin silicon nitride layers were grown to form an interlayer between silicon and HfO_2 in order to test for a stabilizing effect on the system.

The (100)-oriented silicon samples were cleaned in-situ by flash annealing, as described in the previous chapter. After gradual cooling the (2×1) surface reconstruction was checked for by LEED. In order to create ultrathin Si_3N_4 layers a sputter gun as well as a plasma source were used. With the sputter gun N_2-ions were implanted into the surface with a kinetic energy of 300 eV. The plasma source generates a highly reactive atomic beam of nitrogen atoms (N, and ionized species of N). In this case an atomic beam is evaporated onto the surfaces without additional acceleration. Thus, a rapid as well as smooth growth of the layers is possible.

Different Si_3N_4 film thicknesses could be obtained by varying the time of exposure N and annealing at temperatures of 900°C during the evaporation procedure. To probe for the reliability of these layers two different layer thicknesses, 9 Å and 25 Å, were prepared at the SGM beamline at the LNLS.

Fig. 5.36 displays an overview XPS scan of a sample surface after preparing the $HfO_2/Si_3N_4/Si$ layer-stack and annealing at 600°C for 10 minutes. The excitation energy was tuned to $h\nu =$ 600 eV. Intensities from all four components of the system can be identified in the spectrum. Despite the number of peaks appearing, all features can be unambiguously allocated to the four elements hafnium, oxygen, nitrogen, and silicon. The presumed layer-stack at this stage

is illustrated in the inset of Fig. 5.36. Comparable to the previous investigations the signals of hafnium (4f) and silicon (2p) were investigated in detail to follow the evolution of the system.

To prove the presence of closed layers at the surface, angle-scanned XPS measurements were conducted probing for the change in the intensity ratios between the silicon, nitrogen, and hafnium signals. As a result, no indication of island formation was found. Further on, the acquired data were useful to calculate the layer thicknesses by the inelastic damping of the Si bulk signal due to the Si_3N_4 and HfO_2 overlayers. This procedure is described in detail in [92]. It requires the inelastic mean free path of electrons with a certain energy through the silicon nitride layer. Its value was calculated to be $\lambda = 5.5$ Å, and was provided by the NIST "effective attenuation length database" (EAL) [128].

The evolution of the two prepared layer-stacks upon annealing is presented in the following. The samples were kept at a certain temperature for 10 minutes for all annealing cycles. The annealing always was followed by a cooling period of at least 30 minutes to avoid temperature induced broadening or shifts of the signals. Afterwards, an XPS investigation using an excitation energy of $h\nu = 250$ eV was conducted.

Fig. 5.37 displays a series of highly resolved spectra obtained from the 9 Å sample. Part (a)

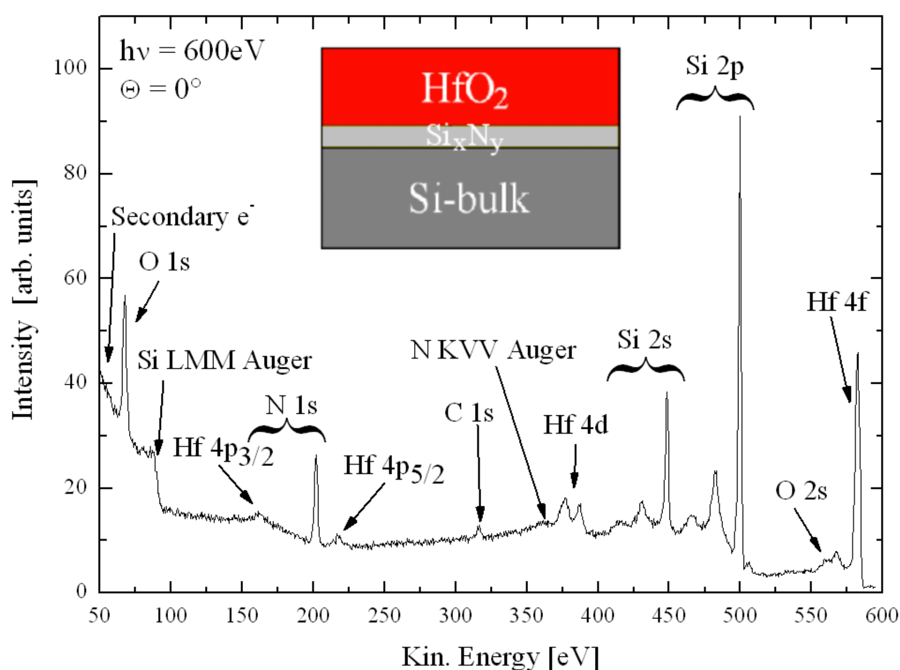

Figure 5.36: Overview spectrum obtained from a sample after growing a Si_3N_4-layer, evaporating HfO_2, and annealing at 600°C for 10 minutes. All intensities are labelled according to [93, 97].

deals with the silicon 2p spectra recorded after annealing at different temperatures. Besides the silicon bulk intensity, set to a relative binding energy of zero, the silicon signal stemming from the silicon nitride layer appears at a binding energy of $E_{relBin} = (+2.8 \pm 0.2)$ eV with respect to the Si-bulk level. According to literature the 2p-level shift of silicon bond in a Si_3N_4 structure is about $3.3 - 3.8$ eV [129, 130] depending on the sample treatment. As the shift happens to be different from the one within SiO_2 ($3.7 - 4.0$ eV, cf. Ch. 5.7) it is possible to distinguish between them in the experiments. Within the detection limit no SiO_2 can be verified. On the other hand the resolution of the experiments turned out to be insufficient for obtaining an unique decomposition of the Si signal into its sub-oxide states, contrary to Ch. 5.7. Therefore, the estimation of chemical shifts in this case bares larger uncertainties.

All signals of Fig. 5.37(a) were normalized with respect to the silicon bulk signal. Changes in the chemical composition are evident upon annealing. Starting at 600°C the intensity ratio between Si-bulk and the silicon nitride component starts to decrease. For lower temperatures no changes were observed, therefore only an exemplary spectrum obtained at 500°C is displayed for the lower annealing temperatures. The decline of the silicon nitride intensity continues for higher temperatures up to 850°C and is also evident for the N 1s signal (not shown). Changes

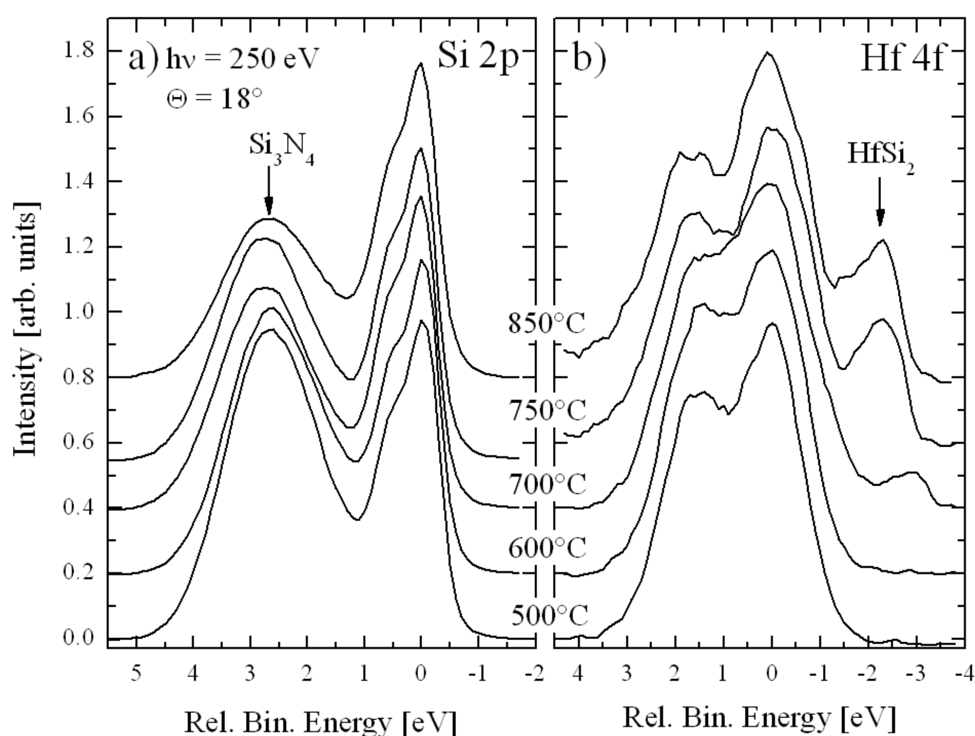

Figure 5.37: Series of XPS spectra recorded from the Si 2p and Hf 4f signals after different annealing cycles. The thickness of the silicon nitride buffer layer is 9 Å. Further details are provided in the text.

can be also observed in the hafnium 4f spectra, displayed in Fig. 5.37(b). At 600°C an additional component can clearly be identified besides the HfO_2 main intensity. Its chemical shift can be estimated to be $\Delta E_{Bin} = (2.3 \pm 0.1)$ eV. The shift can be neither directly allocated to the formation of a silicate compound, nor to the formation of $HfSi_2$. In fact, several different shifts of the hafnium signal are reported depending on the method of preparation and the subsequent sample treatment, see e. g. [126, 131]. The exact chemical composition cannot be anticipated by the data. The shift observed is similar to that of a Hf_xN_y phase. Again, several stoichiometries are possible influencing the chemical shift with respect to HfO_2 (and $HfSi_2$). Details can be found in the publication of Arranz [131] and citations within. These findings suggest the chemical shift of HfN with respect to the pure Hf phase to be between 1 eV and 2 eV. This matches the observations in Fig. 5.37(b), but gives no final prove. Additional, higher resolved measurements are necessary in the future in order to obtain depth profiles for the contribution of the different species.

Another sample was prepared to test for the effects of a thicker Si_3N_4 slab. Therefore a $20-25$ Å layer was grown on silicon. The results of the heating cycles applied to this sample are summarized in Fig. 5.38. The layer-thickness determination is more inaccurate in this case, because the Si bulk signal needed for the calculation is almost fully damped by the HfO_2 film. The spectra in Fig. 5.38(a), recorded under an angle of $\theta = 18°$ with respect to normal emission, expose hardly any signs of the bulk component.

The result of this second investigation shows some differences compared to the first layer prepared. Neither the silicon, nor the hafnium signal, denote changes as they were observed for the thinner layer. Within the sensitivity of the experiments the layer-stack appears to be fully stable up to annealing temperatures of 1000°C. This gives rise to the assumption that for the thinner Si_3N_4-layer bulk silicon plays some role in forming the new component appearing in the Hf 4f spectra.

Silicon nitride inter-layers clearly affect the stability of HfO_2 on silicon, but the exact composition of the new layer-stack could not be uniquely determined. Experiments with higher energy resolution are necessary. For these experiments nitrogen plasma evaporation will be used in order to induce the growth of a Si_3N_4 layer. First experiments using this new method were already conducted. Fig. 5.39 displays XPS spectra taken from a silicon sample before (black line) and after (red line) N-plasma exposure using a SPECS atom beam gun [132]. The clean silicon sample was kept at 500°C during the evaporation, compared to $800-900$°C for the sputter induced nitrogen implantation. The exposure time was set to five minutes, compared to 30 minutes for N_2-sputtering. These first results denote the high efficiency of the procedure and

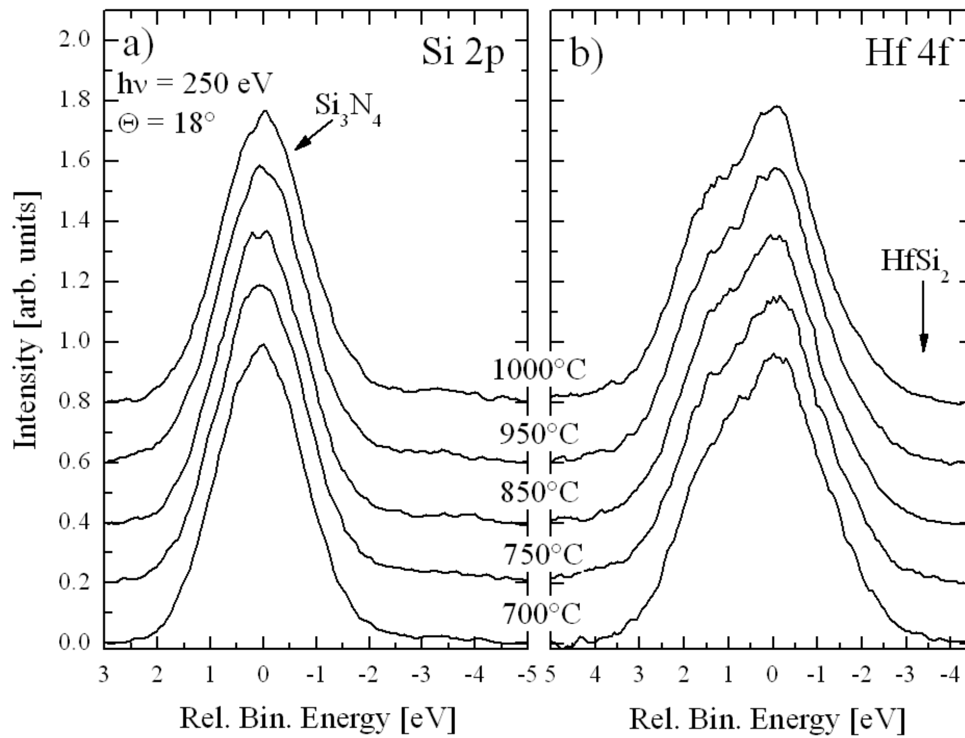

Figure 5.38: Series of XPS spectra recorded from the Si 2p and Hf 4f signals after different annealing cycles. The thickness of the silicon nitride buffer layer is 20-25 Å. Further details are provided in the text.

promise the production of uniform layers. New results on the $HfO_2/Si_3N_4/Si$ layer-stack are expected for the first half of 2008.

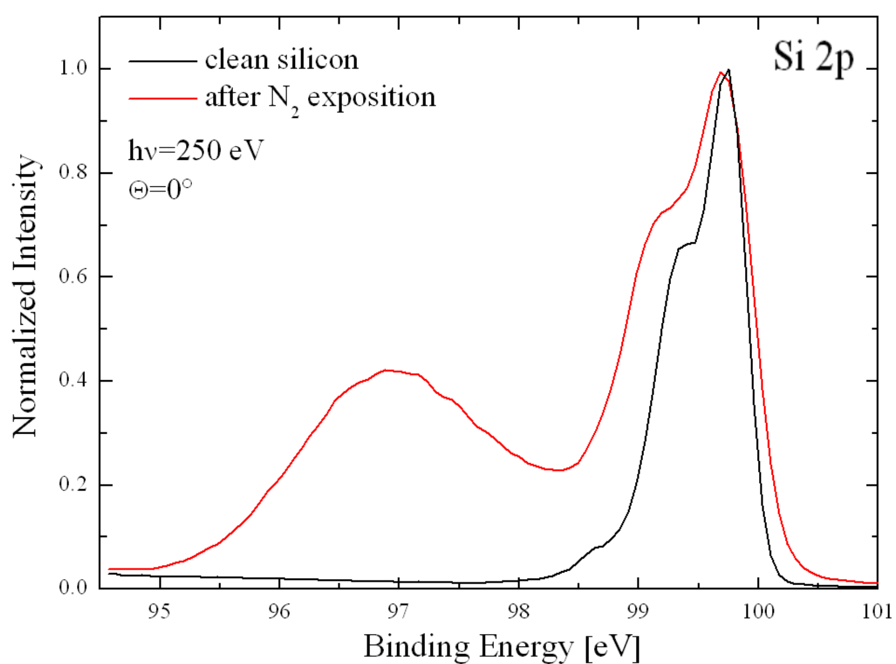

Figure 5.39: First spectrum of a silicon nitride layer prepared by nitrogen plasma evaporation (red line). The Si 2p spectrum of the clean sample is provided for comparison.

6 Conclusions and Outlook

Structure and morphology of the systems $HfSi_2$/Si(100), HfO_2/Si(100), and HfO_2/Si_3N_4/Si(100) were investigated by photoemission techniques and real-space imaging. As shown in Ch. 3 these systems are of significance in the field of high-k dielectrics and metallic nanowires [1,6].

Spectroscopic investigations were performed by using x-ray photoelectron spectroscopy (XPS) and its angle-resolved version (ARPES). Reciprocal space investigations were performed quantitatively by x-ray photoelectron diffraction (XPD) and qualitatively by low-energy electron diffraction (LEED). Real space images of the prepared systems were obtained by using atomic force microscopy (AFM) and scanning electron microscopy (SEM).

Mg K_α-radiation ($h\nu = 1253.6\,\text{eV}$) as well as synchrotron light were available as excitation sources for the XPS and XPD measurements. In the soft x-ray regime synchrotron radiation at excitation energies of $h\nu = 180\,\text{eV}$ and $h\nu = 400\,\text{eV}$ was used for investigating $HfSi_2$. The HfO_2 investigations were performed at $h\nu = 200\,\text{eV}$ and $h\nu = 650\,\text{eV}$. Two different synchrotron light sources were involved in the investigations: The synchrotron light source DELTA at Dortmund (Germany) and the LNLS in Campinas (Brazil). The high-flux undulator beamlines 5 and 11 in Dortmund were used to record XPD patterns, including XPS investigations. The SGM dipole beamline at the LNLS was used e. g. to investigate the system HfO_2/Si_3N_4/Si involving mainly XPS measurements and ARPES.

The experimental procedures to prepare the systems discussed in Chs. 5.3-5.5 were reported in a preceding work [92]. The experimental procedures presented in Chs. 5.6-5.8 were not reported previously.

To draw conclusions from the experimental findings, extensive fitting and simulation procedures needed to be performed. For this purpose, a commercial Levenberg-Marquardt algorithm was used to fit single XPS spectra. Further, a Nelder-Mead simplex algorithm (Java library) was adopted to an existing program structure, developed in this and a preceding work. These algorithms were applied for extensive peak fitting problems, e. g. the decomposition of $7000 - 8000$ XPS spectra within a single XPD pattern. For structure determinations using the XPD results

a genetic algorithm was developed in the course of the work. These kind of probabilistic algorithms, in contrary to deterministic ones (simplex methods etc.), are used in cases where no analytical test functions are available. They are used to work quickly on vast parameter spaces, but usually slow down in the vicinity of the minimum. At this stage grid searches were used to identify its exact position. The so called “R-factor” was used as a quantitative measure to compare experimental XPD patterns to calculated ones. This quantity can be described as a normalized sum of square deviations between the patterns. It returns values from zero to two, while values close to zero correspond to a good match between the patterns.

In order to distinguish diffraction effects stemming from the substrate and those originating from the investigated structures, clean silicon surfaces were investigated by XPS and XPD (cf. Ch. 5.2). As this system is already well known the investigations served also as a check for the reliability of experimental and simulation procedures.

Before performing high resolved synchrotron measurements on the system, the presumed structural model, the C49 structure [49], was tested using a severely higher surface coverage, up to 30 Å, and Mg K_{α}-radiation. Experiments concerning this system as well as preliminary results were reported in a previous investigation, showing the principal applicability of the C49 structure model. This model was proposed for bulk $HfSi_2$ in the 1950s and it was not self-evident that it could also be used for ultrathin layers of this system. For reducing the R-factor, interlayer distances were relaxed and possible surface terminations were tested (Ch. 5.3) using the sophisticated program MSCD [56]. At this point the genetic algorithm was not yet developed. It turned out that the x-ray tube investigation was not very sensible to the topmost layer and unambiguous results regarding reconstructions could not be obtained at this point. On the other hand, comparisons with other base structures that were reported for transition metal silicides clearly showed that only the C49 structures is capable to resemble major diffraction sites of the experimental XPD patterns. Decided progress was made by the introduction of stacking faults. Since they affected more than one layer it was possible to probe for their influence using the x-ray tube data. All statistical mixtures for different stacking faults were tested. By this procedure the R-factor dropped from R=0.5 to R=0.32. This R-value can be considered being quite low, at least for this high kinetic energy investigation, where hundreds of atoms contribute to the model clusters, due to a rather long mean free path within the solid. The final model cluster contains 284 atoms and uses a mixture of one of the presumed stacking faults, called SFA in the course of the work, and the non-faulted structure.

The results show the applicability of the C49 structure, also called zirconium silicide structure. But to obtain distinct information about the first layers surface sensitive experiments must be

performed: An ultrathin Hf layer of around one monolayer thickness was prepared and annealed at 750°C. Synchrotron radiation was tuned to an excitation energy of $h\nu = 180\,\mathrm{eV}$ for enhanced surface sensitivity. The resulting XPS investigation indicated that only one chemical component was present on the surface. Doniach-Sunjic profiles, as they appear for metallic compounds, were necessary to decompose the spectra. The metallicity of the system is expected for bulk material, but was not presumed in prior for ultrathin layers. The XPD results were compared to C49 model clusters, of which the top most layers were used in the simulations. Besides the relaxation of interlayer distances and the cluster radius, also non-structural parameters were included in the so called R-factor analysis. These were the inner atomic potential and the wave expansion, for example. The low kinetic energy causes the 1st layer of the cluster to significantly contribute to the patterns. Significant changes of the simulated patterns could be obtained only by varying the layer terminating the clusters at the surface. A single layer Si-termination was found. The same sensibility applies to surface reconstructions. By probing for different surface reconstructions a missing-row reconstruction led to significantly lower R-factors than for other models, including the non-reconstructed surface. Further progress was made by adding stress to lattice. Due to the lattice mismatch between $HfSi_2$ and silicon of around 5 % the lattice is expected to be distorted at the surface. In fact, a distortion of 4.5 % of the model clusters led to the lowest R-factors. By including all the changes to the model the R-factor dropped from R=0.28 to R=0.105. This value can be considered as extremely low. Since the simulations always assume perfect structures, what is never achieved with real surfaces, R-factors below 0.1 can usually not be obtained according to experience. Thus the obtained R-factor is very close to this “frontier”.

After different initial layer thicknesses were prepared it turned out that the corresponding diffraction patterns changed drastically. Of course, this points to a change in the structure of the system. From this it was decided to perform further investigations with thicker an initial coverage of $1-1.5\,\mathrm{nm}$ hafnium. The resulting diffraction pattern, presented in Ch. 5.5, exposes many differences compared to patterns of the previous investigation. Almost all relaxations had to be performed again. For this investigation a 2-layer Si surface termination had to be chosen, as it showed the best match of R=0.32 compared to the experimental findings. After conducting a comparable relaxation procedure as before, an R-factor of R=0.20 was achieved. During the test for the surface reconstruction the clusters turned out to have low R-values if atomic rows from the edges of the clusters were removed. This finally led to a reshaping of the model, initially having a hemispherical morphology representing a section into the bulk, to an elongated trapezoidal morphology representing a structure on top of the surface. After the reshaping the R-factor decreased from R=0.20 to R=0.14, a drastic drop in this range. Is was already assumed that the structure forms elongated islands at the surface, due to a drastic drop of

the hafnium signal during annealing investigated by angle resolved photoemission spectroscopy. Indication for this can also be found in the literature. Although, it was not expected to observe an influence of the cluster morphology on the simulations. Up to now XPD only has been used to determine interface structures or surface reconstructions, i. e. it was used with fraction of layers on surfaces. No other determination of three-dimensional arbitrary distributed islands, including structure as well as morphology, could be found in the literature. Further relaxations for clusters with a silicon double-row surface termination led to an R-factor of R=0.11, equally as good as for the previous investigation. Attempts to apply the new cluster shape to the thinner-layer results led to no progress for this investigation. The R-factor even increased for those clusters.

A further information held by the XPD patterns is the alignment between the main axes of the islands and the silicon substrate. Results from the literature show that a growth along the [011] and $[0\bar{1}1]$ directions is expected [79]. This could be proved by the XPD results by comparing the alignment of the calculated patterns to the alignment of the experimental one (recorded from the same surface at the same time). The lattice mismatch of 5 % between the lattices, as mentioned before, already corresponds to that growth direction.

As a final prove for the presence of elongated island structures on the investigated surfaces, atomic force microscopy as well as scanning electron microscopy experiments were performed. Those are presented in Ch. 5.6. Both measurements support the findings by XPS and XPD. As assumed, the length of the islands extends to larger scales than the sensibility of XPD. Thus, the XPD pattern corresponds to a small, but representative fraction of the nanowires forming. Even though the aspect ratio of the islands obtained here is lower than already obtained by proper preparation procedures, their length is far above the lateral detection limit of XPD.

The results presented here are comparable with observations for rare-earth metal silicides investigated in the past years. In particular, the silicides of dysprosium, but also those of europium and gadolinium form nanowire structures on a Si(100) substrate of the stoichiometry ASi_2 [82, 114, 133], where A denotes the rare earth element. In the literature, lattice mismatches up to 9 % lead to the formation of nanowires for the rare earth silicides. The investigations on these systems were predominantly performed with scanning probe methods, therefore the results mainly refer to the surface morphology. Eu, Gd, and Dy silicides are possible candidates for an XPD investigation in the next future. The found morphology of the ASi_2 systems is similar to the rectangular/trapezoidal morphology for the $HfSi_2$/Si(100). The measured width of Eu/Dy/Gd silicide structures (by STM) ranges from 1.5 – 13 nm, their height from 0 – 2 nm [77, 82]. The results in this work indicate an island size of at least 1.5 nm and 1 nm for width and height, respectively.

As a next step the development of the system HfO_2/Si(100) was tested. Its thermal instability is reported in the literature [3,7], but the preparation procedures used there turn out to be different compared to the preparations in this work, cf. Ch. 5.7. An electron beam evaporator was prepared to carry grains of HfO_2 that were directly evaporated onto the surface. Using this method a silicon oxide and silicide-free surface could be obtained. Although, step-wise annealing of the system up to 500°C caused the formation of a SiO_2 inter-layer and annealing at temperature above 700°C disintegrated the system. The oxygen is completely removed afterwards. XPD patterns recorded from the system after the 500°C annealing stage showed no ordered structure at the interface between silicon and silicon oxide. After annealing at 750°C XPD patterns, comparable to ones of $HfSi_2$, could be obtained. Concluding it can be stated that the system HfO_2/Si(100) is not thermally stable under the used preparation conditions.

One possible way to stabilize HfO_2 at the surface could be the implantation of nitrogen, or the creation of a thin Si_3N_4 buffer layer between the oxidized hafnium and the silicon surface. In Ch. 5.8 different layer thicknesses of silicon nitride were grown by N_2 sputtering on top of a Si(100) surface before evaporating HfO_2. The experiments were conducted at the LNLS in Campinas. Subsequent annealing cycles clearly indicated a stabilizing effect of such a buffer layer. Nevertheless, no unambiguous clarification of the interfacial layer, forming upon annealing, could be provided for a thinner silicon nitride layer (9 Å). For a thicker layer of around 20-25 Å no visible change occurred in the spectra upon annealing. The system appeared to be stable up to temperatures of 1000°C. The lack of any changes for the thicker layer indicates the role of bulk silicon for the formation of the new interfacial layer observed for the thinner layer. This assumption has to be verified by further experiments.

In order to prepare such experiments with higher energy resolution and growing more homogenous Si_3N_4 layers at DELTA, first tests using a nitrogen-plasma source were conducted. In this preliminary experiments the desired layers could be produced five to ten times faster compared to the previous investigations.

Other perspectives for future investigations are to solve the structure of other nano-structured systems forming islands, clusters, or wires at their surfaces. After the sensibility of XPD to such structures was shown in Ch. 5.5 many systems are in reach for this kind of investigation.

A Properties of Hafnium and Silicon

Silicon

Property	Value
Symbol	Si
Atomic number	14
Atomic weight	28.086 u
Classification	half-metal
Electronic config.	[Ne],$3s^2$,$3p^2$
Melting point	1410°C
Boiling point	2355 °C
Density	2.33 g/cm^3
Lattice type	fcc (diamond)
Lattice constant	5.43 Å
Covalent radius	1.1 Å
Resistivity	10^{-8} Ωm

Table A.1: Physical properties of silicon.

Hafnium

Property	Value
Symbol	Hf
Atomic number	72
Atomic weight	178.49 u
Electronic config.	[Xe],$4f^{14}$,$5d^2$,$6s^2$
Classification	metal
Melting point	2150°C
Boiling point	5400°C
Density	13.31 g/cm^3
Lattice type	hcp
Lattice constant	a=3.196 Å, b=3.196 Å, c=5.051 Å
Covalent radius (emp.)	1.5 Å
Vapor pressure	0.00112 Pa at 2500 K

Table A.2: Physical properties of hafnium.

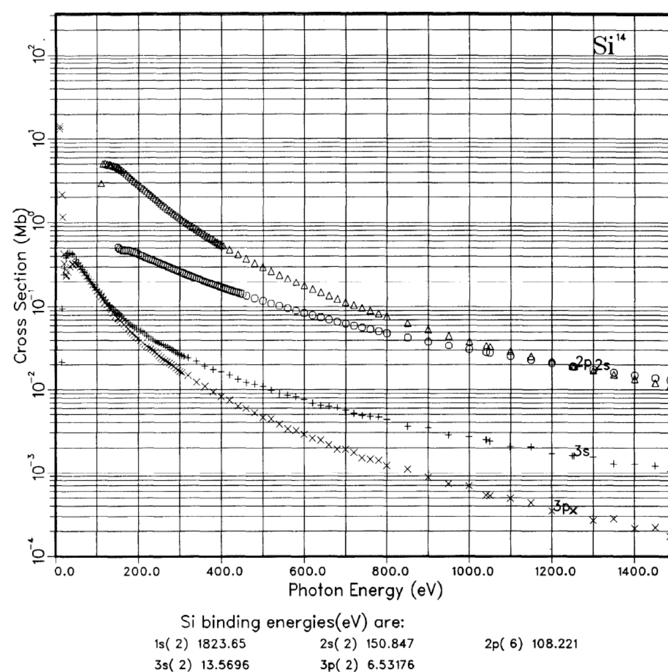

Figure A.1: Sub-shell ionization cross-sections of silicon [13].

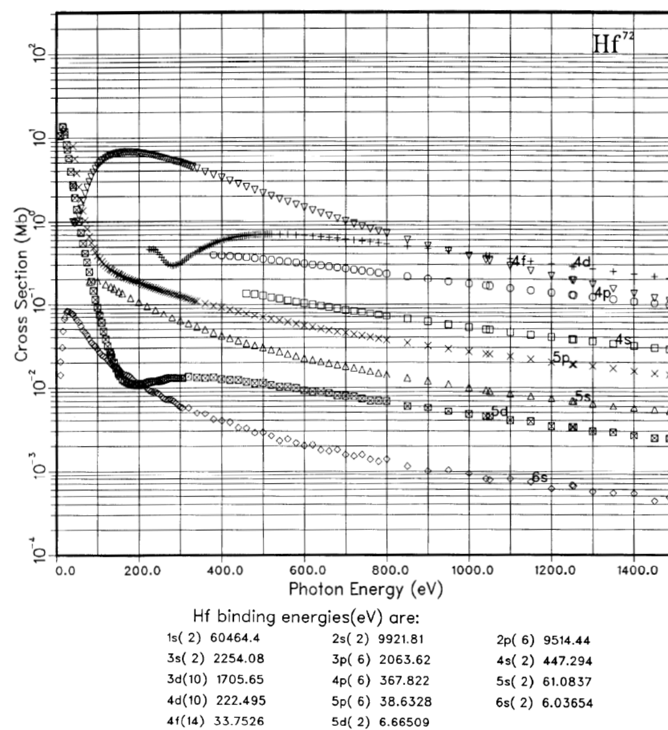

Figure A.2: Sub-shell ionization cross-sections of hafnium [13].

B Sample Input Files

```
        741     10      190     datakind begining-row linenumbers
----------------------------------------------------------------
MSCD Version 1.00 Yufeng Chen and Michel A Van Hove
Lawrence Berkeley National Laboratory (LBNL), Berkeley, CA 94720
basierend auf try 64-6 mit 10% gestreckter zweiter lage
----------------------------------------------------------------

      HfSi C49-4f                       HfSi input file

un      "Christian Fluechter"       user name
sn      HfSi C49-4f             system name
ps01    psIn_HfAbner.txt                input phase shift data file
ps02    psIn_Si.txt             input phase shift data file
rm      rmIn_Hf.txt             input radial matrix data file
pe      HfSiC49-Calc66-20-bigcluster.txt   output photo emission data file

228     10      0.0             scanmode,dispmode,ftolerance

3       20      3       4       linitial, lnum, msorder, raorder
21      0       2       0       layers, finals, fitmath, trymax
18.03   18.03   0.0             kmin, kmax, kstep (per angstrom)
0.0     80.0    2.0             dthetamin, dthetamax, dthetastep (degree)
0.0     360.0   2.0             dphimin, dphimax, dphistep (degree)
55.0    0.0     1               ltheta, lphi, beampol (degree)
0.0     0.0     5               mtheta, mphi, acceptang (degree)
12      14      3.66            radius, depth, lattice(angs)
4       0.0     8.03    234.61  valence, bandgap(eV), density(g/cm3), mweight
178.49  28.1    28.1    28.1    effective weight for kind 1-4 (amu)
0.0     0.0     0.0     0.0     magnetization amplitude for kind 1-4
8.0     430.0   300.0   0.05    vinner(eV), tdebye, tsample(K), pathcut
0.0     0.0     0.0             fit try for vinner, tdebye and lattice

1       2       0       0       layer, kind, emitter, lineatom
0       0       0       0       latoms(xa,xb,ya,yb)
1.0     0.0     unita(len ang) (C49 structure)
1.0     90.0    unitb(len ang) (in unit of lattice)(lage 5 Si)
0.5     0.0     origin(len,ang) (in unit of lattice)
0.0                     interlayer spacing (unit lattice)
0.0     0.0     0.0             fit try for spacing, length and units

2       2       0       0       layer, kind, emitter, lineatom
0       0       0       0       latoms(xa,xb,ya,yb)
1.0     0.0     unita(len ang) (C49 structure)
1.0     90.0    unitb(len ang) (in unit of lattice)(lage 5 Si)
0.5     0.0     origin(len,ang) (in unit of lattice)
0.4590738107657433                      interlayer spacing (unit lattice)
0.0     0.0     0.0             fit try for spacing, length and units

3       2       0       0       layer, kind, emitter, lineatom
0       0       0       0       latoms(xa,xb,ya,yb)
1.0     0.0     unita(len ang) (C49 structure)
1.0     90.0    unitb(len ang) (in unit of lattice)(lage 6 Si)
0.0     0.0     origin(len,ang) (in unit of lattice)
0.5830601                       interlayer spacing (unit lattice)
0.0     0.0     0.0             fit try for spacing, length and units

4       1       1       0       layer, kind, emitter, lineatom
0       0       0       0       latoms(xa,xb,ya,yb)
1.0     0.0     unita(len ang) (C49 structure)
1.0     90.0    unitb(len ang) (in unit of lattice)(lage 7 Hf)
0.7071067       45.0    origin(len,ang) (in unit of lattice)
0.1475409                       interlayer spacing (unit lattice)
0.0     0.0     0.0             fit try for spacing, length and units

           .                     .
           .                     .
           .                     .
```


Figure B.1: Sample input file for the MSCD program [56].

```
c**************MSPHD.INP***************
 &job
 core='4f7/2',
 norman='stdcrm',
 charelx='ex',
 &end
********* HfSi2(100) -Si term ; 2em lmax 8**********
 Computation of potential parameters
11.75  emin ( minimal kin. energy(Ry))
11.75  emax ( maximal kin. energy(Ry))
1.     estep (energy step(Ry))
8      lmax (maximum value of l)
0.0    vinp (inner coulombic potential(Ry) (calculated if 0.0))
0.0    rhoinp (interstitial charge density (atomic u.) (calculated if 0.0))
01.03 cip    (ionisation potential(Ry))
0.0  fermi (fermi edge(Ry)    (calculated if 0.0))
2      teti (initial polar angle(deg))
80     tetf (final polar angle (deg))
40     ntet (number of polar angle calculation)
2.     phii (initial azimuthal angle (deg))
360.   phif (final azimuthal angle (deg))
180    nphi ( number of azimuthal calculations)
0      imov (0/moving sample 1/moving detector 2/both)
125.   tetp ( polar angle of x-ray at detection normal (deg))
0.     phip (azimuthal angle for x-ray incidence plane (deg))
90.    epol (angle between e-field and normal to the incidence  plane (deg))
0      icalcmode (calculation mode (0 full- 1 angular pattern))
*****************cluster surface cell********************************
*******x direction means azimuthal angle equal zero******************
36.49  0.000  ai,aj (components  of unit cell vector  (angstrom))
0.000  36.77  bi,bj (components  of unit cell vector  (angstrom))
10.5           radius (maximum radius of scattering (angstrom))
the x's and y's of the list are given in cell units the z's in angstrom;
w is the emitter contribution; ncalc is the number of symmetry related
emitters; ncalc lines follow the emitter line with related values of phii
and phif.
#atom    x        y        z   zato      w  sym ncalc (I3,3F9.5,2F7.3,A3,I3)
001  -0.5100  0.05000  1.97444 14.0    0.000  N  0
002  -0.4080  0.05000  1.97444 14.0    0.000  N  0
003  -0.3060  0.05000  1.97444 14.0    0.000  N  0
004  -0.2040  0.05000  1.97444 14.0    0.000  N  0
005  -0.1020  0.05000  1.97444 14.0    0.000  N  0
006   0.0000  0.05000  1.97444 14.0    0.000  N  0
007   0.1020  0.05000  1.97444 14.0    0.000  N  0
008   0.2040  0.05000  1.97444 14.0    0.000  N  0
009   0.3060  0.05000  1.97444 14.0    0.000  N  0
010   0.4080  0.05000  1.97444 14.0    0.000  N  0
011   0.5100  0.05000  1.97444 14.0    0.000  N  0
012  -0.5100 -0.05000  1.97444 14.0    0.000  N  0
013  -0.4080 -0.05000  1.97444 14.0    0.000  N  0
014  -0.3060 -0.05000  1.97444 14.0    0.000  N  0
015  -0.2040 -0.05000  1.97444 14.0    0.000  N  0
016  -0.1020 -0.05000  1.97444 14.0    0.000  N  0
017   0.0000 -0.05000  1.97444 14.0    0.000  N  0
018   0.1020 -0.05000  1.97444 14.0    0.000  N  0
019   0.2040 -0.05000  1.97444 14.0    0.000  N  0
020   0.3060 -0.05000  1.97444 14.0    0.000  N  0
021   0.4080 -0.05000  1.97444 14.0    0.000  N  0
           •                             •
           •                             •
           •                             •
           •                             •
           •                             •
           •                             •
```

header

non-structural parameters + lattice constant

structure (given by sinlge atoms)

Figure B.2: Sample input file for the MSPHD program [57].

Bibliography

[1] G. D. WILK, R. M. WALLACE, and J. M. ANTHONY, *J. Appl. Phys.* **89**, 5243 (2001).

[2] C. J. FÖRST, C. R. ASHMAN, K. SCHWARZ, and P. E. BLÖCHL, *Nature* **427**, 53 (2004).

[3] J. ROBERTSON, *Rep. Prog. Phys.* **69**, 327 (2006).

[4] D. A. MULLER, T. SORSCH, S. MOCCIO, F. H. BAUMANN, K. EVANS-LUTTERODT, and G. TIMP, *Nature* **399**, 758 (1999).

[5] W. SHOCKLEY, *Proc. IRE* **40**, 1365 (1952).

[6] J.-H. LEE and M. ICHIKAWA, *J. Vac. Sci. Technol. A* **20**, 1824 (2002).

[7] J.-H. LEE, *J. Korean Phys. Soc.* **44**, 1590 (2004).

[8] H. HERTZ, *Ann. Phys. u. Chem.* **267**, 983 (1887).

[9] A. EINSTEIN, *Ann. Phys.* **14**, 164 (2005), formerly: *Ann. Phys.* **17**, 132 (1905).

[10] K. SIEGBAHN, U. GELIUS, H. SIEGBAHN, and E. OLSON, *Phys. Lett. A* **32**, 221 (1970).

[11] T. KOOPMANS, *Physica* **1**, 104 (1934).

[12] G. KAINDL, T.-C. CHIANG, D. E. EASTMAN, and F. J. HIMPSEL, *Phys. Rev. Lett.* **45**, 1808 (1980).

[13] J. J. YEH and I. LINDAU, *At. Data Nucl. Data Tables* **32**, 1 (1985).

[14] M. P. SEAH and W. A. DENCH, *Surf. Interface Anal.* **1**, 2 (1979).

[15] C. S. FADLEY, *Electron Spectroscopy: Theory, Techniques and Applications*, volume 2, Academic Press, London, 1978.

[16] D. P. WOODRUFF and T. A. DELCHAR, *Modern Techniques of Surface Science*, chapter 3, p. 105ff., Cambridge University Press, Cambridge, 2nd edition, 1994.

[17] J. KIRZ, D. ATTWOOD, and B. HENKE, *X-Ray Data Booklet*, Lawrence Berkeley Laboratory, 1986.

[18] S. DÖRING, Grundlagen zur Charakterisierung der Undulatorbeamline U55 (Bl11) an der Synchrotronstrahlungsquelle DELTA, Diploma thesis, Universität Dortmund, 2007.

[19] M. HENZLER and W. GÖPEL, *Oberflächenphysik des Festkörpers*, Teubner, 1991.

[20] P. AUGER, *J. Physique Radium* **6**, 205 (1925).

[21] R. W. FINK, R. C. JOPSON, H. MARK, and C. D. SWIFT, *Rev. Mod. Phys.* **38**, 513 (1966).

[22] J. OSTERWALDER, T. GREBER, E. WETLI, J. WIDER, and H. J. NEFF, *Prog. Surf. Sci.* **64**, 65 (2000).

[23] G. CZYCHOLL, *Theoretische Festkörperphysik*, Springer Verlag, Heidelberg, Germany, 2nd edition, 2004.

[24] P. A. HATHERLY, J. R. I RIU, M. STANKIEWICZ, F. M. QUINN, and L. J. FRASINSKI, *J. Phys. B: At. Mol. Opt. Phys.* **35**, L77 (2002).

[25] W. PRICE, *Electron Spectroscopy: Theory, Techniques and Applications I*, Academic Press, London, 1977.

[26] S. HÜFNER, *Photoelectron Spectroscopy*, p. 112, Springer, 2nd edition, 1996.

[27] K. SIEGBAHN, *Philos. Trans. R. Soc. London, Ser. A* **268**, 33 (1970).

[28] G. K. WERTHEIM, P. M. T. M. V. ATTEKUM, and S. BASU, *Solid State Commun.* **33**, 1127 (1980).

[29] G. JOHANSSON, J. HEDMAN, A. BERNDTSSON, M. KLASSON, and R. NILSSON, *J. Electron Spectrosc. Relat. Phenom.* **2**, 295 (1973).

[30] F. SCHWABL, *Quantenmechanik I*, chapter 13, p. 227 ff., Springer Verlag, Berlin, 6. edition, 2004.

[31] S. DONIACH and M. SUNJIC, *J. Phys. C* **3**, 285 (1970).

[32] G. D. MAHAN, *Phys. Rev. B* **11**, 4814 (1975).

[33] B. H. ARMSTRONG, *J. Quant. Spectrosc. Radtat. Transfer.* **7**, 61 (1967).

[34] OriginLab Corporation, One Roundhouse Plaza, Northampton, MA 01060, USA, *Origin 7.0 SR0*, 2002.

[35] Acolyte Science, United Kingdom, http://www.casaxps.com/help_manual, *CasaXPS Help Manual*, 2005.

[36] D. ADAMS and J. ANDERSEN, *FitXPS*, Institute of Physics and Astronomy, University of Aarhus, DK-8000 Aarhus C, Denmark.

[37] C. S. FADLEY, *Surf. Sci. Rep.* **19**, 231 (1993).

[38] C. S. FADLEY, *Phys. Scr.* **T17**, 39 (1987).

[39] D. P. WOODRUFF and A. M. BRADSHAW, *Rep. Prog. Phys.* **57**, 1029 (1994).

[40] C. WESTPHAL, *Surf. Sci. Rep.* **50**, 1 (2003).

[41] A. LIEBSCH, *Phys. Rev. Lett.* **32**, 1203 (1974).

[42] S. DREINER, *Untersuchung von Ober- und Grenzflächen mittels niederenergetischer Photoelektronenbeugung*, PhD thesis, Westfälische Wilhelms-Universität Münster, 2002.

[43] C. S. FADLEY, *Synchrotron Radiation Research: Advances in Surface and Interface Science*, volume 1, chapter 9, pp. 421–517, Plenum Press, New York, 1992.

[44] M. C. ASENSIO, *Surf. Rev. Lett.* **4**, 295 (1997).

[45] J. HASE and A. M. BRADSHAW, *Synchrotron Radiation Research: Advances in Surface and Interface Science*, pp. 55–125, Plenum Press, New York, 1992.

[46] J. STÖHR, *X-ray Absorption: Principles, Applications, Techniques of EXAFS, SEXAFS and XANES*, pp. 443–571, Wiley, New York, 1988.

[47] D. J. HANNAMAN and M. A. PASSLER, *Surf. Sci.* **203**, 449 (1988).

[48] D. A. WESNER, F. P. COENEN, and H. P. BONZEL, *Phys. Rev. Lett.* **60**, 1045 (1988).

[49] J. F. SMITH and D. M. BAILEY, *Acta Cryst.* **10**, 341 (1957).

[50] S. DREINER, M. SCHÜRMANN, and C.WESTPHAL, *Phys. Rev. Lett.* **93**, 126101 (2004).

[51] B. COLLIER, *Optical Holography*, Associated Press, New York, 1971.

[52] M. TEGZE and G. FAIGEL, *Nature* **380**, 49 (1996).

[53] S. EISEBITT, J. LÜNING, W. F. SCHLOTTER, M. LÖRGEN, O. HELLWIG, W. EBERHARDT, and J. STÖHR, *Nature* **432**, 885 (2004).

[54] R. W. GERCHBERG and W. O. SAXTON, *Optik* **35**, 237 (1972).

[55] J. WIDER, F. BAUMBERGER, M. SAMBI, R. GOTTER, A. VERDINI, F. BRUNO, D. CVETKO, A. MORGANTE, T. GREBER, and J. OSTERWALDER, *Phys. Rev. Lett.* **86**, 2337 (2001).

[56] Y. CHEN and M. V. HOVE, *MSCD Package*, Lawrence Berkeley National Laboratory, www.sitp.lbl.gov, 1998.

[57] R. GUNNELLA, F. SOLAL, D. SÉBILLEAU, and C. R. NATOLI, *Comp. Phys. Comm.* **132**, 251 (2000).

[58] Y. CHEN, F. J. G. DE ABAJO, A. CHASSÉ, R. X. YNZUNZA, A. P. KADUWELA, M. A. V. HOVE, and C. S. FADLEY, *Phys. Rev. B* **58**, 13121 (1998).

[59] F. SALVAT and R. MAYOL, *Comp. Phys. Comm.* **74**, 358 (1993).

[60] J. REHR and R. C. ALBERS, *Phys. Rev. B* **41**, 8139 (1990).

[61] F. J. G. DE ABAJO, A. CHASSÉ, Y. CHEN, M. A. V. HOVE, and C. S. FADLEY, *(unpublished)* .

[62] L. HEDIN and S. LUNDQVIST, *J. Phys. C: Solid State Phys.* **4**, 2064 (1971).

[63] The Numerical Algorithms Group Limited, *NAG Fortran Library Manual – Mark 17, The Numerical Algorithms Group Limited*, 1995.

[64] W. H. PRESS, S. A. TEUKOLSKY, W. T. VETTERLING, and B. FLANNERY, *Numerical Recipes in C*, chapter 15.5, pp. 681–688, Cambridge University Press, New York, 1992.

[65] J. A. NELDER and R. MEAD, *Computer Journal* **7**, 308 (1965).

[66] M. T. FLANAGAN, *Java Scientific Library*, University College London, Torrington Place, London, UK, 2004.

[67] M. KOTTCKE and K. HEINZ, *Sur. Sci.* **376**, 352 (1997).

[68] A. BRUNETTI, *Comput. Phys. Commun.* **124**, 204 (2000).

[69] Intel Corporation, Santa Clara, California, USA, 2007.

[70] S. TANG, R. M. WALLACE, A. SEABAUGH, and D. KING-SMITH, *Appl. Surf. Sci.* **135**, 137 (1998).

[71] G. TIMP, J. BUDE, K. K. BOURDELLE, J. GARNO, A. GHETTI, H. GOSSMANN, M. GREEN, G. FORSYTH, Y. KIM, and R. KLEIMANN, *Tech. Dig. Int. Electron Devices Meet.* (1999).

[72] G. LUPINA, T. SCHROEDER, J. DABROWSKI, C. WENGER, A.-U. MANE, H.-J. MÜSSIG, P. HOFFMANN, and D. SCHMEISSER, *J. Appl. Phys.* **99**, 114109 (2006).

[73] H. T. JOHNSON-STEIGELMAN, A. V. BRINCK, S. S. PARIHAR, and P. F. LYMAN, *Phys. Rev. B* **69**, 235322 (2004).

[74] N. MIYATA, Y. MORITA, T. HORIKAWA, T. NABATAME, M. ICHIKAWA, and A. TORIUMI, *Phys. Rev. B* **71**, 233302 (2005).

[75] A. DE SIERVO, C. R. FLÜCHTER, D. WEIER, M. SCHÜRMANN, S. DREINER, M. F. CARAZZOLLE, A. PANCOTTI, R. LANDERS, G. G. KLEIMAN, and C. WESTPHAL, *Phys. Rev. B* **74**, 75319 (2006).

[76] J. XIANG, W. LU, Y. HU, Y. WU, H. YAN, and C. M. LIEBER, *Nature* **441**, 489 (2006).

[77] D. R. BOWLER, *J. Phys. Cond. Matter* **16**, R721 (2004).

[78] Y. NAKAYAMA, P. J. PAUZAUSKIE, A. RADENOVIC, R. M. ONORATO, R. J. SAYKALLY, J. LIPHARDT, and P. YANG, *Nature* **447**, 1098 (2007).

[79] J.-H. LEE, *Appl. Surf. Sci.* **239**, 268 (2005).

[80] Y. WU, J. XIANG, C. YANG, W. LU, and C. M. LIEBER, *Nature* **430**, 61 (2004).

[81] J. NOGAMI, B. Z. LIU, M. V. KATKOV, C. OHBUCHI, and N. O. BIRGE, *Phys. Rev. B* **63**, 233305 (2001).

[82] Y. CHEN, D. A. A. OHLBERG, and R. S. WILLIAMS, *J. Appl. Phys.* **91**, 3213 (2002).

[83] Laboratório Nacional de Luz Síncrotron, C.P. 6192, 13084-971 Campinas, SP, Brazil, *LNLS*.

[84] I. LANGMUIR, *J. Am. Chem. Soc.* **38**, 2221 (1916).

[85] VG Microtech, Uckfield, East Sussex, England, *CLAM 4 MCD Analyser System Operating Manual*, 1995.

[86] *Focus GmbH*, 65510 Hünstetten-Görsroth, Germany.

[87] Berufsgenossenschaftliches Institut für Arbeitsschutz - BGIA, www.hvbg.de/e/bia/gestis/stoffdb/index.html, *GESTIS-database on hazardous substances*, 2007.

[88] D. F. AVERY, J. CUTHBERT, N. J. D. PROSSER, and C. SILK, *J. Sci. Instrum.* **43**, 436 (1966).

[89] W. P. REED, Certificate of Analysis, Standard Reference Material 745, Technical report, National Institute of Standards and Technology, Gaithersburg, Maryland, USA, 1990.

[90] U. BERGES, M. KRAUSE, M. SCHÜRMANN, S. DREINER, R. FOLLATH, F. SCHÄFERS, and C. WESTPHAL, *Synchrotron Radiation Instrumentation: Eighth International Conference* , 424 (2004).

[91] D. A. SHIRLEY, *Phys. Rev. B* **5**, 4709 (1972).

[92] C. R. FLÜCHTER, Präparation und Charakterisierung ultradünner Hafniumfilme auf Siliziumsubstraten, Diploma thesis, Universität Dortmund, 2005.

[93] C. D. WAGNER, W. M. RIGGS, L. E. DAVIS, and J. F. MOULDER, *HANDBOOK OF X-RAY PHOTOELECTRON SPECTROSCOPY*, Perkin-Elmer Corporation, 6509 Flying Cloud Drive, Eden Prairie, Minnesota 55344, 1978.

[94] M. A. V. HOVE and S. Y. TONG, *Surface Crystallography by LEED*, Springer Verlag, Berlin, 1979.

[95] C. KITTEL, *Introduction to Solid State Physics (German Translation)*, chapter 1, p. 9 ff., John Wiley & Sons, Inc., 8th edition, 2005.

[96] S. TANUMA, C. POWELL, and D. PENN, *Surf. Sci.* **192**, L849 (1987).

[97] C. D. WAGNER, W. M. RIGGS, L. E. DAVIS, and J. F. MOULDER, *HANDBOOK OF AUGER ELECTRON SPECTROSCOPY*, Perkin-Elmer Corporation, 6509 Flying Cloud Drive, Eden Prairie, Minnesota 55344, 1978.

[98] G. K. WERTHEIM, D. M. RIFFE, J. E. ROWE, and P. H. CITRIN, *Phys. Rev. Lett.* **67**, 120 (1991).

[99] S. DREINER, C. WESTPHAL, M. SCHÜRMANN, and H. ZACHARIAS, *Thin Solid Films* **428**, 123 (2003).

[100] C. R. FLÜCHTER, A. DE SIERVO, D. WEIER, M. SCHÜRMANN, U. BERGES, S. DREINER, M. F. CARAZZOLLE, R. LANDERS, G. G. KLEIMAN, and C. WESTPHAL, *Mater. Sci. Semicond. Process.* **9**, 1049 (2006).

[101] K. SCHUBERT, *Kristallstrukturen zweikomponentiger Phasen*, Springerverlag, Berlin, 1964.

[102] M. IANNUZZI, P. RAITERI, M. CELINO, and L. MIGLIO, *J. Phys.: Condens. Matter* **14**, 9535 (2002).

[103] A. BOURRET, F. M. D'HEURLE, F. K. L. GOUES, and A. CHARAI, *J. Appl. Phys.* **67**, 241 (1990).

[104] C. R. FLÜCHTER, A. DE SIERVO, D. WEIER, M. SCHÜRMANN, U. BERGES, S. DREINER, M. F. CARAZZOLLE, R. LANDERS, G. G. KLEIMAN, and C. WESTPHAL, *J. Electron Spectrosc. Relat. Phenom.* **156**, 92 (2007).

[105] D. WEIER, Präparation und Charakterisierung ultradünner Hafniumoxidfilme auf Siliziumsubstraten, Diploma thesis, Universität Dortmund, 2005.

[106] A. ARRANZ, *Surf. Sci.* **563**, 1 (2004).

[107] C. R. FLÜCHTER, A. DE SIERVO, D. WEIER, M. SCHÜRMANN, A. BEIMBORN, S. DREINER, M. F. CARAZZOLLE, R. LANDERS, G. G. KLEIMAN, and C. WESTPHAL, *Surf. Sci.* **submitted** (2008).

[108] K. HEINZ, L. HAMMER, A. KLEIN, and A. SCHMIDT, *Appl. Surf. Sci.* **237**, 519 (2004).

[109] J. OSTERWALDER, A. TAMAI, W. AUWÄRTER, M. ALLAN, and T. GREBER, *Chimia* **60**, A795 (2006).

[110] *Institute for Analytical Sciences*, Bunsen-Kirchhoff-Str. 11, 44139 Dortmund, www.isas.de.

[111] S. L. FLEGER, J. W. HECKMAN, and K. L. KLOMPARENS, *Scanning and Transmission Electron Microscopy (German Translation)*, Oxford University Press Inc., 1993.

[112] Omicron Vakuumphysik GmbH, Idsteiner Str. 78, 65232 Taunusstein, Germany, *UHV STM/AFM*.

[113] A. BEIMBORN, Untersuchung von Hafnium- und Hafniumoxidfilmen auf Si(001) mittels Rasterkraftmikroskopie, Diploma thesis, Universität Dortmund, 2007.

[114] C. PREINESBERGER, S. K. BECKER, S. VANDRÉ, T. KALKA, and M. DÄHNE, *J. Appl. Phys.* **91**, 1695 (2002).

[115] T. J. HUBBARD and D. G. SCHLOM, *J. Mater. Res.* **11**, 2757 (1996).

[116] L. XINYE, S. RAMANATHAN, A. LONGDERGAN, A. SRIVASTAVA, E. LEE, T. E. SEIDEL, J. T. BARTON, P. DAWEN, and R. G. GORDON, *J. Electrochem. Soc.* **152**, G213 (2005).

[117] Y. WIDJAJA and C. B. MUSGRAVE, *J. Chem. Phys.* **117**, 1931 (2002).

[118] C. KYU-JEONG, S. WOONG-CHUL, and Y. SOON-GIL, *J. Electrochem. Soc.* **149**, F18 (2002).

[119] L. SUNGJOO and K. DIM-LEE, *Jpn. J. Appl. Phys., Part 1* **43**, 427 (2004).

[120] C. R. FLÜCHTER, D. WEIER, M. SCHÜRMANN, S. DÖRING, U. BERGES, and C. WESTPHAL, *Surf. Sci.* **accepted** (May 2008).

[121] F. J. HIMPSEL, F. R. MCFEELY, A. TALEB-IBRAHIMI, J. A. YARMOFF, and G. HOLLINGER, *Phys. Rev. B* **38**, 6084 (1988).

[122] Y. UEHARA, K. KAWASE, J. TSUCHIMOTO, and T. SHIBANO, *J. Electron Spectrosc. Relat. Phenom.* **148**, 74 (2005).

[123] R. PUTHENKOVILAKAM and J. P. CHANG, *J. Appl. Phys.* **96**, 2701 (2004).

[124] S. DREINER, M. SCHÜRMANN, and C. WESTPHAL, *J. Electron Spectrosc. Relat. Phenom.* **137-140**, 79 (2004).

[125] J. H. OH, H. W. YEOM, Y. HAGIMOTO, K. ONO, M. OSHIMA, N. HIRASHITA, M. NYWA, A. TORIUMI, and A. KAKIZAKI, *Phys. Rev. B* **63**, 205310 (2001).

[126] M. R. VISOKAY, J. J. CHAMBERS, A. L. P. ROTONDARO, A. SHANWARE, and L. COLOMBO, *Appl. Phys. Lett.* **80**, 3183 (2002).

[127] S. JEON, C. J. CHOI, T. Y. SEONG, and H. HWANGA, *Appl. Phys. Lett.* **79**, 245 (2001).

[128] C. POWELL and A. JABLONSKI, *NIST Electron Effective-Attenuation-Length Database*, National Institute of Standards and Technology, Gaithersburg, Maryland, USA, 2001.

[129] K. J. KIM, T. H. KANG, K. IHM, C. JEON, C. C. HWANG, and B. KIM, *Surf. Sci.* **600**, 3496 (2006).

[130] C. H. F. PEDEN, J. W. ROGERS(JR.), N. D. SHINN, K. B. KIDD, and K. L. TSANG, *Phys. Rev. B* **47**, 15622 (1993).

[131] A. ARRANZ, *Surf. Sci.* **563**, 1 (2004).

[132] Oxford Scientific, Culham Innovation Centre, Oxon, UK, *OSPrey Plasma Source Operating Manual*, 2008.

[133] B. Z. LIU and J. NOGAMI, *J. Appl. Phys.* **93**, 593 (2003).

Publications

A. de Siervo, C.R. Flüchter, D. Weier, M. Schürmann, S. Dreiner, M.F. Carazzolle, A. Pancotti, R. Landers, G.G. Kleiman, and C. Westphal, *The hafnium silicide formation on Si(100) upon annealing*, Phys. Rev. B **74** (2006) 75319

C.R. Flüchter, A. de Siervo, D. Weier, M. Schürmann, U. Berges, S. Dreiner, M.F. Carazzolle, R. Landers, G.G. Kleiman, and C. Westphal, *Structure analysis of the system Hafnium/Silicon(100) by means of X-ray photoelectron spectroscopy and X-ray photoelectron diffraction (XPD)*, Mater. Sci. Semicond. Process. **9** (2006) 1049

D. Weier, C. Flüchter, A. de Siervo, M. Schürmann, S. Dreiner, U. Berges, M.F. Carazzolle, A. Pancotti, R. Landers, G.G. Kleiman, and C. Westphal, *Photoelectron spectroscopy (XPS) and photoelectron diffraction (XPD) studies on the system hafnium silicide and hafnium oxide on Si(100)*, Mater. Sci. Semicond. Process. **9** (2006) 1055

C.R. Flüchter, A. de Siervo, D. Weier, M. Schürmann, U. Berges, S. Dreiner, M.F. Carazzolle, R. Landers, G.G. Kleiman, and C. Westphal, *Photoelectron diffraction study and structure determination of ultrathin hafnium silicide layers on silicon(100) using Mg* K_α *radiation and synchrotron light*, J. Electron Spectrosc. Relat. Phenom. **156** (2007) 92

M.F. Carazzolle, M. Schürmann, C.R. Fluechter, D. Weier, U. Berges, A. de Siervo, R. Landers, G.G. Kleiman, and C. Westphal, *Structural and electronic analysis of Hf on Si(111) surface studied by XPS, LEED and XPD*, J. Electron Spectrosc. Relat. Phenom. **156** (2007) 393

C.R. Flüchter, D. Weier, M. Schürmann, U. Berges, S. Döring, and C. Westphal, *Evolution of chemical states within the* HfO_2*/Si(100) interface upon annealing, prepared by direct electron beam evaporation*, Surf Sci. (2008) **accepted for publication**

C.R. Flüchter, A. de Siervo, D. Weier, M. Schürmann, A. Beimborn, S. Dreiner, M.F. Carazzolle, R. Landers, G.G. Kleiman, and C. Westphal, *Structure determination of three-dimensional hafnium silicide nano structures on Si(100) by means of x-ray photoelectron diffraction*, Surf. Sci. (2008) **submitted**

F. Schönbohm, C.R. Flüchter, D. Weier, U. Berges, S Döring and C. Westphal, *Thermal behavior of ultrathin ZrO_2 films and structure determination of $ZrSi_2$ islands on Si(100)*, Phys. Rev. B (2008) **submitted**

M.F. Carazzolle, C.R. Flüchter, A. de Siervo, D. Weier, R. Landers, G.G. Kleiman, and C. Westphal, *Stability of HfO_2 on Si(100) mediated by Si_3N_4 buffer layers*, J. Appl. Phys. (2008) **in preparation**

Acknowledgements

At first I would like to thank my supervisor Prof. Dr. Carsten Westphal for providing me the opportunity to work in his group, for supporting me with all his expertise, and supplying me with all the fancy equipment needed in the lab. I also thank Prof. Dr. Thomas Weis for taking the time to act as a second referee for my thesis.

Further on, thanks go to the E1-group members without whom this work would not have been possible and who always patiently wasted their time in my favor. In particular I want to thank Stefan Dreiner and Mark Schürmann who introduced me to all the methods and the equipment, and who assisted me with my diploma thesis and my first publications. Thanks to all the guys in my and the neighboring office (Daniel Weier, Axel Beimborn, Frank Schönbohm, Tobias Lühr, Patrick Mehring) for innumerable fruitful discussions and for always creating a relaxing working atmosphere. I thank Eva Henschel for being my good conscience throughout all the years and encouraging me in difficult times. Thanks go to Sven Döring and Ulf Berges for illuminating my samples during the last three years, albeit of exploding beamlines. Of course, without the staff of DELTA and the LNLS there would have been no synchrotron light at the first place.

Agradeçimentos cordiais aos Brasilieros, sobretudo a Abner de Siervo, para a sua grande ajuda durante o meu trabalho dentro e fora do Brasil. Agradeço a Marcello Carazzolle, Alexandre Pancotti, Richard Landers e George Kleiman para o seu trabalho, com o que eles ajudaram-me muito. Aprendi muitas coisas deles, não somente ligado com física.

I thank Alex von Bohlen and the institute for analytical sciences (ISAS) for all the help with the scanning electron microscope images.

Finally, I am much obliged to my friends and my family for their immeasurable endurance they brought up, and for reminding me of my out-of-university life in the periods I spent more time talking to UHV-chambers than talking to them.